INSTITUT POLYTECHNIQUE DE PARIS

NNT : 2023IPPAXXXX

Thèse de doctorat

Turbulent approaches to image analysis and statistical fractography

Thèse de doctorat de l'Institut Polytechnique de Paris
préparée à l'Ecole polytechnique

École doctorale n°626 École doctorale de l'Institut Polytechnique de Paris (EDIPP)
Spécialité de doctorat : Physique

Thèse présentée et soutenue à Palaiseau, le 27 novembre 2023, par

SAMY LAKHAL

Composition du Jury :

Emmanuel Bacry CNRS & Université Paris Dauphine	Président
Frédéric Dufaux CentraleSupelec	Rapporteur
Jean Schmittbuhl CNRS & Université de Strasbourg	Rapporteur
Camille Couprie FacebookAI	Examinatrice
Michael Benzaquen CNRS & Ecole polytechnique	Directeur de thèse
Laurent Ponson CNRS & Sorbonne Université	Co-directeur
Alexandre Darmon Art in Research	Co-encadrant
Henri Maître Telecom Paris	Invité

TURBULENT APPROACHES TO IMAGE ANALYSIS AND STATISTICAL FRACTOGRAPHY

SAMY LAKHAL

27th of November, 2023

Samy Lakhal: *Turbulent approaches to image analysis and statistical fractography*, 27th of November, 2023

FOREWORD

In 2019, my quest for a research internship led me to meet Michael Benzaquen, who at that time had freshly founded the EconophysiX lab together with Jean-Philippe Bouchaud. My initial goal was to explore a subject interfacing finance and statistical physics. We decided that I would work on quantitative aesthetics.

In 2020, I recontacted Michael, with whom I had a great research experience. This time, I was decided to explore a finance-related project. It was compromised that I would work on poetry generation.

It occurred to me that adaptability was a useful quality, but that I may also benefit from being more persuasive. Eager to develop this skill – among the many others that would be of use in my future career – I started a PhD in late 2020 under the supervision of Michael Benzaquen, Laurent Ponson and Alexandre Darmon.

During my PhD I had the chance to work on exciting topics, the most important aspects of which were published in international peer reviewed journals, see [1–4]. I had the opportunity to give tutorials on sociophysics, optimization and machine learning at ENSAE and supervise three interns in the group. I attended two summer schools at Como and Brunico in Italy, and shared my works at the StatPhys28 conference in Tokyo. I was also invited for 6 weeks in the Quantitative Life Science group of the Abdus Salam International Center of Theoretical Physics by Matteo Marsili. This Italian interlude gave me the inspiration to write a short communication paper on Quantitative Aesthetics for Polytechnique Insights [5].

Finally, the PhD was the opportunity to engage in lab-life activities, such as the organization of several team dinners and gatherings, as well as two Lab retreats with my friend and colleague Cecilia Aubrun. The co-supervision also allowed me to meet people of various backgrounds at the EconophysiX Lab, LadHyX and Institut Jean Le Rond D'Alembert.

I must say, these three years have been the most interesting and fulfilling of my life. Yet, I have no doubts that the best is yet to come.

ACKNOWLEDGMENTS

I want to thank all members of the jury for participating in the evaluation of my doctoral thesis. In particular I am grateful to Emmanuel Bacry and Camille Couprie for accepting to be examiners; Frédéric Dufaux and Jean Schmittbuhl for reviewing the manuscript; and Henri Maître for accepting my invitation.

Doctoral students are first of all students, and the quality of their supervision will often make the quality of their experience. I want to thank my supervisors Michael Benzaquen, Alexandre Darmon and Laurent Ponson for their strong involvement in the supervision of my thesis. In particular I want to express my gratitude to Michael and Alexandre for their time, trust and support.

I express my gratitude to Jean-Philippe Bouchaud, Iacopo Mastromatteo and Matteo Marsili for their involvement in several projects, and important discussions. I am grateful to Matteo Marsili for inviting me at the Quantitative Life Science section of the Abdus Salam International Center of Theoretical Physics in Trieste, Italy.

These three years were the opportunity to meet many people from EconophysiX, LadHyX and ∂'Alembert. I would like to mention Sarah, Mahshid, Yutao and Lucas from d'Alembert; Iman and Pratsmesh from LadHyX; and Jérôme, Cécilia, Salma and Pierre from EconophysiX. In particular, I want to thank Cécilia and Jérôme for their kindness and support.

A research lab is first of all a structure that must be managed administratively and socially. I want to thank all these people who establish an environment conducive to research and discussion: Delphine and Michael from EconophysiX; Sandrine, Toaï, Blaise, Emmanuel and Lutz from LadHyX; and Simona, Catherine and Pierre-Yves from ∂'Alembert. I want to warmly thank Simona for her systematic involvement in the well-being of every intern, PhD student and postdoctoral researcher.

The doctoral thesis is the finishing line of a long and studious path. I am grateful for the involvement of every teacher and principal I met during those years. In particular, I want to thank Christian Charrier, Frédéric Lesne, Karim Bouchekoura, Alain Gille, Mme Proux, Thibault Kerhervé, Christine Weill, Vincent Cros, Mathilde Colin de Verdière, Sévérine Mensch, Antoine Landart, Dominique Mouhanna and Nicolas Sator.

Sometimes, the road of studies is rough. Fortunately, having great friends softens that path. I express my gratitude to my roommates Antoine and Valentin; to Lorenzo, Paul.R, Bénédicte and Romain from

high school; Badih, Rémi, Jean, Youssef, Maëlys, Baptiste and Pierre-Thomas from Lycée Pasteur; and Erwan, Merwan, Anthony, Gauthier, Vincent, Christelle, Elsa and David from École Normale Supérieure Paris-Saclay.

I want to thank Patricia, with whom I have shared three wonderful years, and who expressed constant support.

Finally, I would like to express my gratitude to my family, and in particular to my mother, father and brother. Their love and support made all of this possible.

ABSTRACT

One may argue that the role of the physicist is to describe the universe from rules and laws. However, while the behaviour of simple physical settings can be derived from first principles, this step becomes increasingly difficult when systems gain in complexity. A second approach consists in characterizing the response of systems to harmonic or stochastic forcing. This method is all the more interesting in high dimension, as it allows one to efficiently explore the configuration space, and highlight specific regimes. Maybe the most classic example would be of fluid turbulence, the analysis of which reveals universal scaling properties, unexpected from the local Navier-Stokes equations. I make strong use of these intuitions by introducing statistical and fluctuations-based tools in the study of two seemingly different subjects: image processing and statistical fractography.

In the first part of this thesis, I tackle three distinct problems in image analysis and processing, by establishing fluctuation-based metrics with straightforward interpretability. First, I revisit the long-standing question of the relation between visual appreciation and image statistics. Our analysis suggests that there might exist some universal quantitative criteria that correlates to aesthetic judgement. Then, I use an agnostic information-theoretic observable to investigate the statistical properties of natural images. Overall, the approach appears as a satisfying candidate for image analysis and processing procedures, while providing a good level of physical interpretability. Finally, I address the specific problem of image color quantization by deriving stochastic mapping algorithms from maximum entropy principles. I use our previously defined measures to calibrate these tools, ultimately revealing satisfying visuals.

The second part of this thesis revolves around the study of fracture surfaces resulting from the complete failure of a material. These surfaces display universal statistical properties reminiscent of fluid turbulence, namely scale invariance, non-Gaussian statistics and multiaffinity. First, I define a minimal class of random fields reproducing these properties. The comparison with fracture surfaces highlights slight differences, mainly related to the presence of cliffs on the surface reminiscent of turbulent dissipation fields filaments. Then, the study of four fracture surfaces from different rocks materials allows us to link the correlation length ξ defining the multifractal regime, with the size of the Fracture Process Zone ℓ_c, in which dissipative coalescence mechanisms occur. Some stochastic models of crack propagation are ultimately derived, and show the emergence of multifractal scaling from ad-hoc assumptions, based on experimental observations.

RÉSUMÉ

D'aucun diraient que le rôle du physicien est de décrire l'univers par des règles et des lois. En réalité, bien que le comportement des systèmes simples puisse être déduit de premiers principes, cette tâche devient difficile lorsque ces systèmes gagnent en complexité. Une seconde approche consiste alors à caractériser la réponse des systèmes soumis à des sollicitations harmoniques ou stochastiques. Cette méthode est d'autant plus intéressante en haute dimension, puisqu'elle permet (i) l'exploration efficace des différentes configurations du système, et (ii) la mise en évidence de certains régimes spécifiques. Un exemple classique serait celui de la turbulence fluide, dont l'étude révèle la présence d'un régime fractal/invariant d'échelle universel, inattendu par les équations de Navier-Stokes. Nous faisons un usage important de ces intuitions en introduisant des outils statistiques dans l'étude de sujets en apparence différents : le traitement d'images et la fractographie statistique.

Dans la première partie de cette thèse, j'aborde trois problèmes distincts du traitement de l'image. Tout d'abord, je revisite la question du lien entre l'appréciation visuelle et les propriétés statistiques des images. L'analyse suggère qu'il existe des critères quantitatifs universels, fortement corrélés au jugement esthétique. Ensuite, j'aborde le cas des images naturelles, dont l'analyse repose sur des observables mesurant l'information contenue dans les images à toutes les échelles : la *Multiscale relevance* (MSR). Notre analyse montre que cette mesure permet des applications directes en analyse et traitement d'images, tout en garantissant une bonne interprétabilité physique. Enfin, j'étudie le problème spécifique de la quantification des couleurs, en établissant des algorithmes à partir de principes de maximisation de l'entropie. Les mesures établies précédemment permettent la calibration de ces outils, et conduisent à des visuels satisfaisants.

Dans la deuxième partie du manuscrit, j'étudie les surfaces de fracture obtenues par la rupture complète d'un matériau. Ces surfaces présentent des propriétés statistiques rappelant la turbulence des fluides par leur invariance d'échelle, et leurs fluctuations non-Gaussiennes. Tout d'abord, je définis une classe de champs aléatoires reproduisant ces propriétés. Leur comparaison avec une surface de rupture permet de souligner les similarités, ainsi que les différences principalement liées à la topologie des évènements turbulents. Enfin, l'analyse de quatre surfaces de roches permet de mettre en évidence le lien entre la longueur de corrélation du régime multifractal, et la taille de la *Fracture Process Zone* où les phénomènes de coalescence de l'endommagement se produisent. Des modèles stochastiques de propagation de fissure sont développés, et montrent l'émergence de la

multifractalité à partir d'hypothèses simples, basées sur des observations expérimentales.

MY PUBLICATIONS

1. S. Lakhal, A. Darmon, J.-P. Bouchaud, and M. Benzaquen, "Beauty and structural complexity," Physical Review Research **2**, 022058 (2020)[Editor's Suggestion][Rapid Communication]

2. S. Lakhal, A. Darmon, and M. Benzaquen, "A new spin on color quantization," Journal of Statistical Mechanics: Theory and Experiment **2023**, 033401 (2023)[Editor's Highlights]

3. S. Lakhal, A. Darmon, I. Mastromatteo, M. Marsili, and M. Benzaquen, "Multiscale relevance of natural images," Scientific Reports **13**, 14879 (2023)

4. S. Lakhal and M. Benzaquen, "Can beauty be quantified?" Trans. by T. Zoé, Polytechnique Insights (2021)

5. S. Lakhal, L. Ponson, M. Benzaquen, and J.-P. Bouchaud, "Wrapping and unwrapping multifractal fields," In preparation (2023)

CONTENTS

INTRODUCTION

In this thesis, I explore two seemingly different topics: image processing and statistical fractography. Despite their apparent differences, we will see that the investigation tools are similar, as they inherit from the physical description of complex systems. Indeed, one may argue that the role of the physicist is to establish the rules and universal behaviors of its environment through experiments, simulation and models.

The role of this introduction is to discuss the quantitative and semantic links between the two topics of this thesis. First, I introduce the concept of complexity, from a classic and scientific. Then, I show how embracing this concept paves the way for a statistical description of systems with numerous degrees of freedom through fluctuation analysis and forcing, for modeling and experimental purposes. Finally, the third and fourth parts of the introduction will review my work in image processing and fractography respectively, under the paradigm introduced earlier.

Note that I will produce systematic comparisons with the statistical description of turbulent flows. This framework encapsulates the main fluctuation based tools employed in the following research work.

1 COMPLEXITY: DEFINITIONS AND CONCEPTS.

Life is really simple, but we insist on making it complicated.

— Confucius

What does it mean to be "complex"? This term is used to characterize a myriad of objects, systems and concepts. We use it so much that its sense and definition seem diluted. We will first review some common definitions that will bring us to discuss the concept of complexity used in science.

1.1 COMPLEXITY IN THE LANGUAGE

The adjective *complex* – or *complexe* in French – originates from the latin *complexus*, which means *plaited*, that is used for example to describe a braided fabric. The idea of individual constituents forming an organized whole starts to appear here. The Cambridge Dictionary provides the following definition:

> Complex (adj): *involving a lot of different but related parts.*
>
> Cambridge Dictionary

The etymology and definition seem thus compatible at first glance. However, *complexus* is also the past tense of *complectere*, meaning to embrace, to comprise, to assess intelligibly. The same dictionary provides a second definition:

> Complex (adj): *difficult to understand or find an answer to because of having many different parts.*
>
> Cambridge Dictionary

This raises a contradiction, that we also observe in the common language: *complex* can be used either in an ameliorative context or in a pejorative one. An object can either be complex when it displays informations but also when it hides it, in which case one may prefer the term *complicated* in agreement with the following definition:

> Complicated (adj):*involving a lot of different parts, in a way that is difficult to understand*
>
> Cambridge dictionary

Interestingly, the etymology of the word *complicated* is different. Indeed, it derives from the latin *complicat*, meaning *folded altogether*. This emphasizes the lesser intelligibility of complicated objects, whose hierarchy is hidden from the observer. This differs from a complex object whose parts can be assessed, studied and possibly understood.

Of course, systems and objects can switch from one category to the other depending on the observer. A piece of jazz and a lecture of advanced physics are complex, but could appear as complicated to the non-initiated one. This status can also change through time, as to the keen observer, initially complicated objects can slowly reveal their complex features.

1.2 COMPLEXITY IN SCIENCE

The idea of complexity is also largely used in the scientific literature.

Complex systems – This expression is widespread in physics [6], sociology [7, 8] or biology [9], to name a few disciplines. The physicist Alain Barrat proposed the following definition:

Complex systems are composed of a large number of constitutive elements, interacting without central coordination, without plans from an invisible architect, and leading to the spontaneous emergence of non-trivial structures [10]

For such systems, simple interaction rules produce non-trivial effects. A famous example is the Ising model [11], initially introduced to understand the ferro-paramagnetic transition observed in magnets. The model consists in a network of micro-magnets (spins) interacting in pairs, through a global energy function (the Ising Hamiltonian). These interactions can be local (e.g. nearest neighbours) and yet lead to patterns of infinite size for specific values of the control parameters (e.g. temperature, external field). The model can be directly related to quadratic minimization problems on discrete state space, a technique also encountered in biology [12], sociology [13], finance [14], and as we will see in Chap. 3, in image processing. Another example is borrowed to fluid mechanics, which provides a *quintessential complex system* [15]: while Navier-Stokes equations characterize the local dynamics, highly non trivial configurations of fluids in motion can appear at a global scale can appear. We will see later these turbulent flows share many common features with the systems that we will explore during this thesis.

We may wonder what a "complicated system" is? This term could apply to a complex system whose interaction rules are unknown yet. This could also relate to its etymological origin: a complicated system is opaque, unpredictable or chaotic. A complicated system in that sense does not have to contain many parts, as some systems become non-integrable with only a few elements, as for example the n-body problem for $n \geq 3$.

Complexity measures – The term appears in the literature to describe quantifiable measures, which can be related to the definitions and etymologies introduced earlier.

Some complexity measures characterize disorder and could be said to be *entropic*. For example in algorithmic theory, the Kolmogorov complexity measure [16–19] is the minimal length of instructions needed to reproduce a given object. To reproduce a list of independent random numbers, one would need to store each one of them: the complexity is maximal. Possessing an underlying regularity yields lower complexity: for example, the terms of an arithmetic sequence can be summed up from the initial state and the difference of successive terms.

However, what is perceived as "complex","rich" or "informative" rarely corresponds to the most disordered objects. This is why some other complexity measures focus on intelligible features, related to *a priori* criteria: distribution of information across scales [3, 20, 21], robustness to denoising [1, 22], emergence of peculiar structures [22] or redundancy in the data [23]. These features can also mimic subjective perceptions, for example in visual assessment: ability to distinguish features [24], sensitivity to local variations of colors and contrasts [25], among many other examples. These descriptors have shown excellent results in visual quality assessment tasks, but this relationship with more formal complexity measures remains elusive.

In Chapter. 1, this gap is bridged by comparing of entropy-based measures with large-scale surveys experiments on visual preference. We will show in Chapter. 2 that this approach leads to more quantitative tools of image analysis, with direct applications in image processing that will be presented in Chapter. 3. Regarding the study of the morphology of fracture surfaces, we will show that the complexity of fracture patterns can be mastered using synthetic images reproducing their main scaling properties in Ch. 4, and ultimately harnessed to explore the elementary physical mechanisms governing the failure resistance of materials in Ch. 5.

2

TRADING COMPLEXITY, EMBRACING RANDOMNESS

As we have seen earlier, complexity can manifest in various ways. The reason is simple: reality is complex and every object possibly interacts with one another, tangled by the fundamental laws of the universe. A low level of complexity is already sufficient to produce erratic or irregular behaviours, for which specific tools must then be developed.

In this second part of the introduction, we will see first that modelling this complexity from random contributions can provide rich insights on the system investigated. Then, reciprocally, injecting such fluctuations may reveal some specific properties of the system. In the following, we provide a brief review of the methods of random modeling used in this research work.

2.1 DESCRIBING FLUCTUATIONS

For the majority of systems, the knowledge of the interactions allows the physicist to make consistent approximations, and reveal universal behaviors through seemingly different systems.

However, we know since Bachelier [26] that some systems drive or get driven by fluctuations. An example is a grain of pollen in a fluid: its erratic displacement is due to convective and diffusive effect of its surrounding medium. More precisely, its trajectory results from the continuous bombarding of fluid particles, which can not be directly derived from first principles. Yet, this does not mean that the behaviour of the grain of pollen cannot be rationalized: if we can not derive an exact expression for these fluctuations, we may then model them as random contributions.

From local fluctuations to Brownian motion – Let us start with a seminal example: the Brownian motion. We consider a particle in a fluctuating environment, for example the grain of pollen described earlier, a colloid in a suspension, or small particles ($\sim 1\mu$m) under the effect of thermal agitation. The idea of Brown in 1827 [27] and later quantified by Einstein in 1905 [28], was to model such fluctuations by introducing a random force term $\boldsymbol{F}(t)$. Writing Newton's second law for the particle velocity then yields

$$m\frac{d\boldsymbol{v}}{dt} = -\gamma\boldsymbol{v} + \boldsymbol{F}(t), \tag{2.1}$$

with m the mass and γ a viscous friction coefficient. We know from the central limit theorem (CLT) that these fluctuations – if reasonable – average to a Gaussian white noise. We consider the *overdamped* regime, where the acceleration term is negligible, and get

$$\boldsymbol{r}(t) = \boldsymbol{r}(0) + \int_0^t \frac{1}{\gamma}\boldsymbol{F}(t)dt. \tag{2.2}$$

The trajectory becomes stochastic and displays a seemingly erratic behaviour, as is show in Fig. 2.1(a). Further assuming $\boldsymbol{F}(t)$ uncorrelated in time and $\langle \boldsymbol{F}^2(t)\rangle = \sigma^2$ with $\langle . \rangle$ the time or ensemble average yields the following scaling behaviour:

$$\langle \|\Delta\boldsymbol{r}\|^2\rangle = \langle \|\boldsymbol{r}(t+\Delta t) - \boldsymbol{r}(t)\|^2\rangle = \frac{\sigma^2}{\gamma^2}t. \tag{2.3}$$

This result indicates that, during a time Δt, a particle explores a surrounding region of average size $\Delta r \propto \sqrt{\Delta t}$ around its starting point. The particle is said to be *diffusing*, and its displacement is parameterized by the diffusion coefficient $D = \Delta r^2/\Delta t$, also found in the diffusion equation. We see in Fig. 2.1(b) that the particle trajectory reveals a hidden form of regularity, that would universally manifest

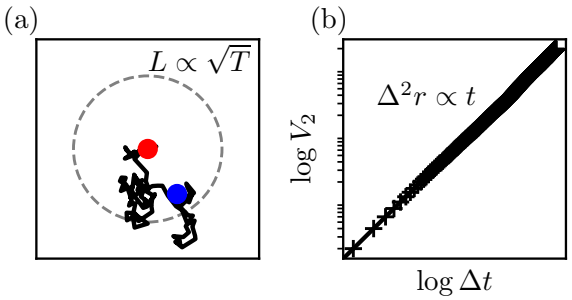

Figure 2.1: Brownian trajectory in 2D. (a) Trajectory (decimated for lisiblity). Red and blue dots are initial and final positions.(b) Variogram of the trajectory.

for similar conditions.

Anomalous scaling – Reasonable fluctuations – meaning white noise with finite variance – lead to diffusive scaling. What happens if these conditions are discarded? For example, replacing Gaussian jump with discrete power-law distributed ones $\rho(r) \propto 1/r^{\alpha+1}$ (for e.g. Pareto or Levy stable [29]) defines so-called *Levy-flights*, introduced by Mandelbrot in 1982 [30]. A direct calculation recovers the following scaling of trajectories:

$$\langle \|\Delta \boldsymbol{r}\|^q \rangle = \langle \|\boldsymbol{r}(t+\Delta t) - \boldsymbol{r}(t)\|^q \rangle \propto \Delta t^{q/\alpha} \quad \text{if } q < \alpha, \tag{2.4}$$

where $\alpha \leq 2$, $\alpha = 2$ corresponding to Gaussian noise. This deviation from diffusive scaling is said to be *anomalous*. Here for $H = 1/\alpha > 1/2$ it is said to be *superdiffusive*, the case $H < 1/2$ being called *subdiffusive*. In Fig. 2.2, we display the trajectories of several flights for different H parameters. We see that high values of H introduce high-jumps events, creating an apparent persistency of the trajectory, as is recovered by the scaling analysis of (b).

On a more general note, anomalous scaling emerges when the Central Limit Theorem breaks down. The sum of random variables (X_i) does no longer scale as $\sqrt{N}$ in the $N \to +\infty$ limit. This situation can be encountered when (i) systems display non-Gaussian properties for their jumps (e.g Lévy flights) or waiting times (e.g subdiffusive CTRW) or (ii) when realizations possess long-range correlations, ultimately changing the effective scaling of the sum. In physical systems, these behaviours result from memory effects [31], disorder [32] or from intermittent fluctuations. These contributions can be described by adequate stochastic models that capture experimental observations.

Scaling through time and space – Identically to particle motion, many systems can display fluctuation and scaling properties, through time

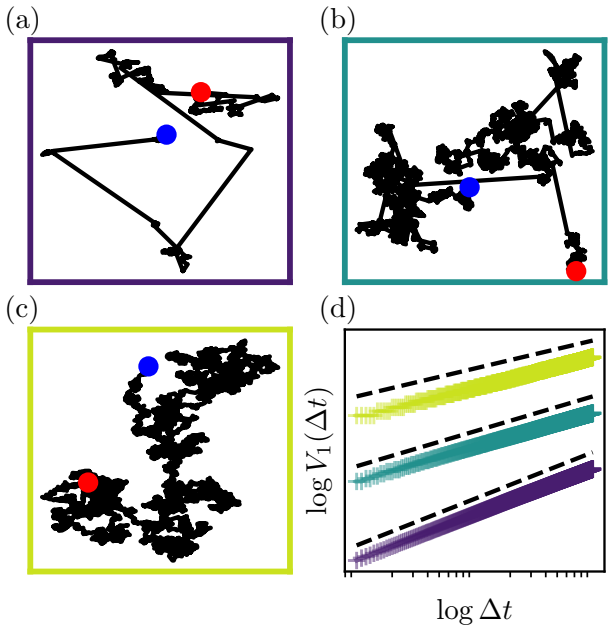

Figure 2.2: Anomalous diffusion of Levy-flights. (a), (b) and (c), particle trajectories sampled from Levy-stable distributed jumps with $H = 0.83, 0.75, 0.5$ respectively. (d) Scaling of trajectories, calculated from the first order variogram $V_1(\Delta t) = \langle |\boldsymbol{r}(t+\Delta t) - \boldsymbol{r}(t)| \rangle$. Black lines indicate theoretical scalings $V_1(\Delta t) \propto \Delta t^H$.

or space. Maybe the most classic example would originate from the works of A.Kolmogorov (1941) [33] who observed universal scaling in turbulent flows, and which was later found to hold for various fluids and systems [34, 35]. More specifically, Kolmogorov highlighted the anomalous scaling of the third order moment of velocity increments $\langle \Delta v_{\parallel}^3 \rangle \propto \Delta r$ ($\neq \Delta r^{3/2}$), whose behaviour can only be derived from Navier-Stokes equations after strong simplifying assumptions (incompressible fluid with local isotropy) [36]. This allowed for the quantitative description of the *energy cascade* [35, 37, 38] where kinetic energy is continuously redistributed from large to small structures, as qualitatively observed by Lewis Fry Richardson in 1922 [39]. Let us note that this behaviour can even emerge from human-made representations such as paintings: a statistical analysis Van Gogh's *Starry Night* (see Fig. 2.3) recovers the universal scaling of turbulent flows [40, 41].

However, this example is only one amongst the many scale-invariant systems. Indeed, many systems under external constraint [37, 42–50]) or specific control parameters [11, 51, 52] can display power-law observables. Similarly to the case of random particles, such scaling properties provide precious insights on the physics at play, e.g. interscale energy transfers, emergent dissipative scales, range of interactions, etc. In Chapter. 5, we will see that the scaling properties of the fracture surfaces can be used as a guideline to decipher their complex geome-

Figure 2.3: Van Gogh's *Starry Night* (1889), MoMa's online Collection. The sky displays eddy-like structures, reminiscent of fluid turbulence.

try, and study the mechanisms controlling material resistance.

2.2 FORCING FLUCTUATIONS

When systems do not initially display such fluctuations, one can introduce them through so-called *forcing*. Let us a consider a given system, described by a field $\phi(\boldsymbol{r}, t)$, function of space and time. It can be the Eulerian velocity $\boldsymbol{v}(\boldsymbol{r}, t)$ in a volume of fluid, the local pressure $P(\boldsymbol{r}, t)$ in a musical instrument, or the color of pixels $h(i, j, t)$ in a video. A straightforward way to characterize the system is to apply an external force and observe its influence on ϕ.

Forcing of linear systems – For linear systems, a harmonic forcing leads to a frequency-dependent response that can be reported in a response diagram (e.g. the Bode diagram for electrical or mechanical systems). The linearity of the system allows one to use any external force $\boldsymbol{F}(\boldsymbol{r}, t)$, and describe the response from Fourier analysis. This translates analytically to

$$A[\boldsymbol{\phi}](\boldsymbol{r}, t) = \boldsymbol{F}(\boldsymbol{r}, t) \tag{2.5}$$

where A is a linear operator describing the space-time evolution of the system. It can include local operators (e.g. derivations, integrations) and non-local ones (e.g. fractional operators [53] or long-range kernels [48, 54]). Applying the Fourier transform $(\mathcal{F})$ on Eq. (2.5) yields

$$\boldsymbol{\phi}(\boldsymbol{k}, \omega) = \tilde{A}^{-1}(\boldsymbol{k}, \omega)\tilde{\boldsymbol{F}}(\boldsymbol{k}, \omega), \tag{2.6}$$

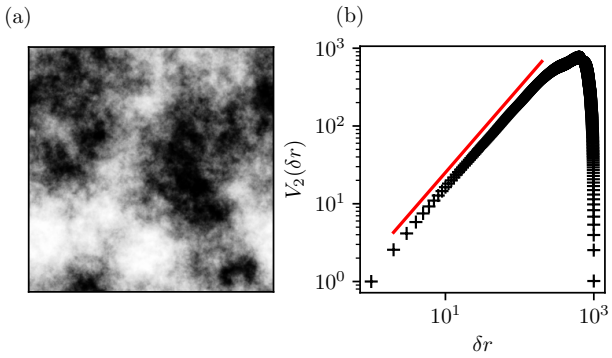

Figure 2.4: Fractional Gaussian field, $H = 0.6$. (a) Quantile representation of the random field $\phi(\boldsymbol{r})$ (b) Variogram $V_2(\delta r) = \langle |\phi(\boldsymbol{r} + \delta \boldsymbol{r}) - \phi(\boldsymbol{r})| \rangle$. Theoretical slope $V_2 \propto \delta r^{2H}$ in red.

showing that the modes of forcing and response are trivially linked to one another.

Stochastic forcing – Forcing does not restrict to harmonic contributions, and can further generalize to stochastic one. For example, taking $\boldsymbol{F}$ as a Gaussian white noise, leads to Gaussian statistics for $\boldsymbol{\phi}$. Its correlation is directly related to the evolution operator:

$$C(\delta \boldsymbol{r}, \delta t) = \langle \boldsymbol{\phi}(\boldsymbol{r}, t) \boldsymbol{\phi}(\boldsymbol{r} + \delta \boldsymbol{r}, t + \delta t) \rangle = \mathcal{F}^{-1} \left[\tilde{A}^{-1} \right] (\delta \boldsymbol{r}, \delta t).$$

Reciprocally, one can sample Gaussian fields of prescribed autocorrelation by applying the convenient filtering to white noise [55]. We have made an extensive use of such method in Chap. 1, 2 and 4, where we generated 2D fields from power-law filters of the form $G(\boldsymbol{k}) \propto 1/k^{\alpha}$. We see in Fig. 2.4 that the resulting fields are fully abstract and yet display statistical regularity, making them specifically relevant for image assessment and processing experiments.

Forcing of non-linear systems – A non-linear system exhibits non-linear responses to external forcing . Equation. (2.6) does no longer apply, and one may observe non-trivial inter-scale responses from the system.

In some specific situations, systems respond by displaying scale invariant properties, e.g. in 3D fluid turbulence, a simple harmonic forcing at *injection scale* induces Kolmogorov scaling up to the viscous dissipation scale. The scaling of non-linear systems can be estimated from scaling arguments [56], perturbative developments [42, 46] or other Renormalization Group (RG) approaches [57, 58]. However in the majority of cases, the scalings are only recovered through numerical simulations [59–63] and experimental setups [64–66]. We will further observe in Chap. 4 that the scale invariance of non-linear systems can

lead to non-Gaussian and intermittent statistics.

Forcing of energy-based models – We have seen that any systems following motion equations could be constrained to external forcing. We now consider the case of systems simply described by the energy functional $E[\phi]$ of their configuration $\phi(\boldsymbol{u})$, with $\boldsymbol{u}$ a relevant index variable. This approach is very useful for multi-agent systems whose global energy can account for interaction effects. For example in the Ising model, the Hamiltonian $\mathcal{H}[(\sigma_i)]$ describes the nearest neighbour interactions of the spins micro-configuration (σ_i). Note that at this point, we do not prescribe any dynamics to the system, and this energy should not be related to a mechanical energy that would recover motion equations. We simply assume that the system evolves towards the global minimizer

$$\phi^* = \arg\min_{\phi} E[\phi]. \tag{2.7}$$

In reality, we know from optimization that the ability of the system to reach such minima will highly depend on the dynamics and on the energy landscape topology. We further add that assuming a completely isolated system, without self-induced fluctuations, wouldn't be realistic. One of the greatest contributions of statistical mechanics is to introduce a way to relax such minimization constraint and account for fluctuations which can model physical effects (colliding particles, thermal noise, etc.), or more complicated processes (agent indecision in opinion models [67]). This can be done by switching from a deterministic viewpoint to a probabilistic one, under maximal entropy assumption. The method consists in finding the most agnostic/entropic distribution, conditionally to specific constraints. If energy minimization is the only constraint, one recovers the famous Boltzmann-Gibbs distribution [68–70]:

$$P_T[\phi] = \frac{1}{Z(T)} e^{-E[\phi]/T}, \tag{2.8}$$

where $Z(T)$ is a normalization term. The temperature parameter T tunes the width of the distribution, from $P_{T=0}[\phi] = \delta(\phi - \phi^*)$, up to the uniform distribution $P_{T\to+\infty}[\phi] = (\#\{\phi\})^{-1}$. We note that Boltzmann-like distributions are widely used, in Monte-Carlo methods [71], *softmax* classifiers [72–74] or generative models [75, 76] and can even be applied to optimization problems in image processing, as will be seen in Chap. 3.

In conclusion, many systems can be characterized from the study of their inherent or induced fluctuations. In the first case, these contributions spontaneously manifest from noisy environment, self-organization or microscopic thermal fluctuations. For the second case, an operator decides to force specific modes of the system, harmonically

or randomly, in time or space. The influence of these fluctuations can be assessed trivially for linear systems, but the task is more difficult for non-linear or energy based models. For these situations, scaling behaviours may arise unexpectedly and provide essential insights on the physics at play.

Let us quickly summarize the first two parts of this introduction. We have seen that complexity refers to a specific scientific concept. Complex systems describe multi-agent frameworks, whose interactions make analytical derivations difficult. On the other hand, complexity measures describe the disorder of a given configuration, or its ability to display features of interest. To study complex systems or complex configurations, defining observables and characterizing their fluctuations can drastically lower the dimension of the problem and help one recover strong insights on the mechanisms at play. Even better, injecting such fluctuations in theoretical or experimental setups constitutes a fruitful tool of investigation. We will see in the rest of this introduction, how these concepts are employed for the processing of images, and the deciphering of fracture surfaces.

3 A PHYSICIST APPROACH TO IMAGE PROCESSING

L'art c'est moi, la science c'est nous.

— Claude Bernard

The first part of the thesis is dedicated to image processing, that is the algorithmic approach to digital photography. The consistent progresses in image processing result from several factors: increase of computational power, increase of optics and display quality [77], developments of new signal processing and learning frameworks [78–80], availability of high-quality data [81–83], or better knowledge of the biological visual process [84, 85]. These have led to the emergence of tools used in our everyday lives: image filtering, denoising [86], retrieval [87, 88], labelling [89, 90], among many others. These last years have been further marked by the training of efficient architectures with large databases, which notably allows for natural language to image generation [91]. See Fig. 3.1 for example.

The goal of our research is to take a slight step back from the tumult of these recent advances, and address three essential questions: What is the link between image statistics and visual appreciation? What is the specificity of classic interpretable images, namely natural images? Can

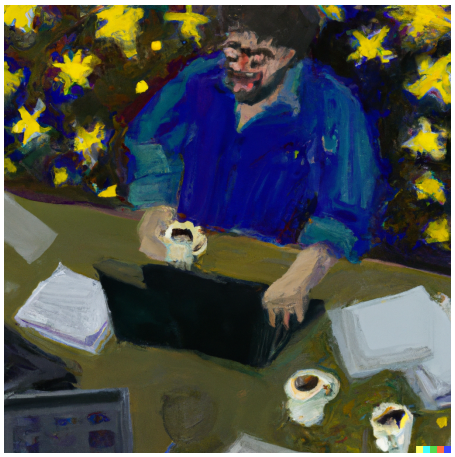

Figure 3.1: *Painting in Van Gogh's starry night style of an enthusiastic PhD student on his computer, with several coffee cups on his desk*, obtained from OpenAI's Dall-E 2 [91].

we answer these questions from novel statistical tools, to solve concrete image processing problems? The viewpoints introduced earlier will allow us to answer these questions in three distinct chapters, for which we now introduce the context.

3.1 AESTHETICS AND COMPLEXITY

Aesthetically pleasing objects display a subtle equilibrium of simplicity and complexity, triviality and originality, respect of rules and their transgressions. As scientists, we naturally ask ourselves whether it is possible to quantify such properties and define universal criteria for aesthetic appreciation [5].

In the context of images, the research of quantitative criteria for the description of aesthetic assessment is simply called *quantitative aesthetics*. A recent and extensive review was produced in [92], showing the diversity of scientific contributions: building of tractable measures [25, 93–99], design of visual assessment experiments [100–105], construction of databases [83, 106–108], prediction of aesthetic quality [109–111], aesthetic informed image enhancement [110, 112–115] and generation [116]. These works have changed the paradigm of image and optic enhancement procedures, which are now aesthetic informed.

In Chapter. 1 –which is largely based on the published work [1]– we revisit the long-standing question of the relation between image appreciation and its statistical properties. We generate two different sets of random images well distributed along three measures of *entropy-based* complexity (spectral, fractal and algorithmic). These first complexities measure the visual disorder of the system. We then run a large-scale survey in which people are asked to sort the images by preference, which reveals maximum appreciation at intermediate entropic complexity. We show that the algorithmic *structural* com-

plexity of the coarse-grained images, expected to capture structural complexity, while abstracting from high frequency noise, is a good predictor of preferences. This second measure assesses intelligible and meaningful contributions of the image. Our analysis suggests that there might exist some universal quantitative criteria for aesthetic judgment, structural complexity being one of them.

3.2 INFORMATION THEORY AND NATURAL IMAGES

The Chapter. 1 introduced a complexity measure relying on the irrelevance of small scale features [1, 22], an *a priori* conditions that may not be relevant in the context of interpretable images such as natural ones. These images have long been studied in the literature for their visual [117, 118], spectral [119–121] and statistical [122–126] properties.

In Chapter. 2 –which reproduces the contents of [3]– we define agnostic observables from a formalism that was recently introduced for the description of high-dimensional data, and reviewed in [23]. The method consists in observing the influence of compression procedures (grid size, number of bits, number of histogram bars, etc.) over simple entropy metrics. The approach has shown interesting theoretical developments [127, 128] and promising applications in finance [127], biology [20], machine learning [129, 130] and statistical physics [23, 131].

In the context of images, we use the Multiscale Relevance (MSR), which assesses the overall robustness of images to compression at all scales. We first characterize the MSR of synthetic random textures and extend the analysis to natural images. We find striking similarities with log-correlated ($H = 0$) random textures. We ultimately apply the MSR in a classic processing context, here the calibration of a denoising algorithm. Overall, the MSR approach appears to be a good candidate for advanced image analysis while providing a satisfying level of interpretability.

3.3 COLOR MAPPING AND MAXIMAL ENTROPY

In Chapter. 2 an information theoretic formalism is used to characterize specific properties of artificial textures and natural images. We wonder if such measures can be applied in a famous image processing problem: color quantization.

Color quantization is a long known problem of image processing, with more than forty years of history [132]. It consists in reducing the color palette of an image, in two main steps. First the *color palette design* groups authorized colors from the statistical analysis of the original image. The methods usually employ thresholding [133, 134] or clustering [135–138] procedures relying on the original histogram. The second step is *color mapping*, which attributes each pixel to the

palette. This can be done from a simple nearest neighbour procedure but stochastic methods can smooth out thresholding artifacts [139–142].

In Chapter. 3 – the results of which have been presented in [2]– we apply a maximal entropy viewpoint to the color mapping step. We find that adding thermal noise to the system improves visual impressions. To quantify this observation, we introduce a coarse-grained quantization error, which computes the distance between convoluted images. The optimal temperature which minimizes this loss is a good proxy for complexity at different scales. Noting that the convoluted error is a key observable, we directly minimize it using a Monte-Carlo algorithm to generate a new series of quantized images. Adopting the Resolution/Relevance based approach introduced in Chapter. 2, we are able to determine an optimal convolution parameter leading to the best visuals. Finally, we test the robustness of our method against changes in image type, color palette and convolution kernel.

4

STATISTICAL ANALYSIS OF FRACTURE SURFACES.

In the second part of this thesis, we study the morphology of fracture surfaces, which are the surfaces created during the failure of materials, and whose topographic maps $h(\boldsymbol{r})$ can be measured by profilometry. In Fig. 4.1 we display three examples for three different materials, taken from [143].

All surfaces display repeating patterns, organized in steep cliffs clearly visible on the gradient map. The size of these cliffs depends on the material. Yet their scaling properties that we will detail in the following, are robust and observed in a wide range of materials.

Scale invariance – Fracture surfaces display scale invariance [144, 145], which corresponds to an invariance of statistics through affine transformations of the space variable. A classic way to assess such property is by computing the variogram, or *roughness function*, from the following expression:

$$V_2(\Delta r) = \langle \Delta^2 h \rangle = \langle |h(\boldsymbol{r} + \Delta \boldsymbol{r}) - h(\boldsymbol{r})|^2 \rangle \propto \Delta r^{2H}. \tag{4.1}$$

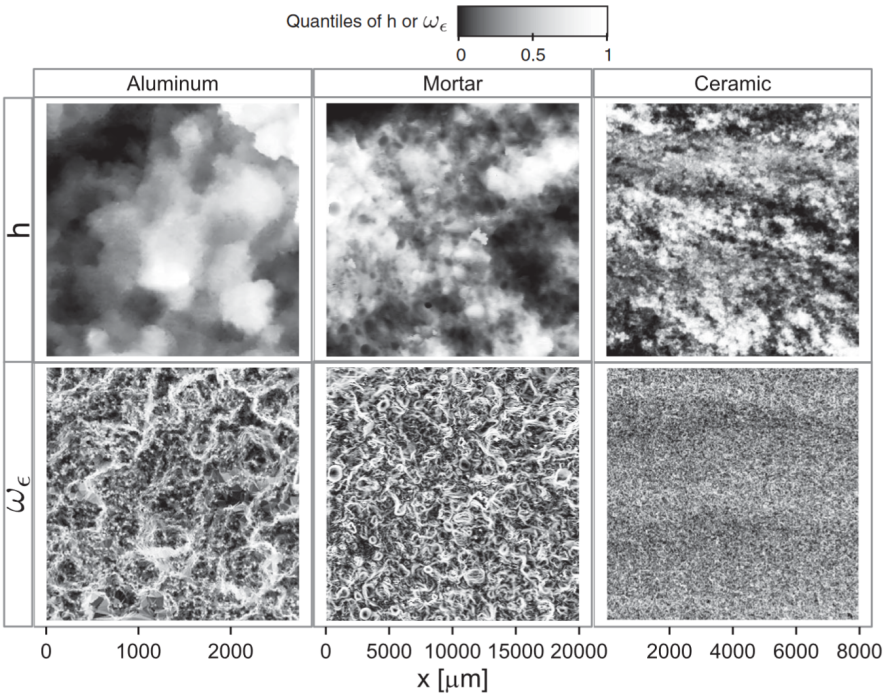

Figure 4.1: Fracture surface morphology of three seemingly different materials from [143]. (Top) Height fields $h(\boldsymbol{r})$ of the fracture surface. (Bottom) Gradient fields. In both cases, the quantiles of the distribution are represented by a gray hue, the largest values being represented by the lightest hue.

This observable measures the amplitude of out-of-plane deviations $\Delta^2 h$, as a function of the in-plane distance Δr. A system is scale invariant when $V_2(\Delta r) \propto \Delta r^{2H}$, where H is the roughness or *Hurst* exponent, a property observed for many materials [144, 145]. We also note that failure resulting from the propagation of a crack can induce anisotropic scaling [44], also reported in [42, 46, 56, 146].

Scaling transition – The scaling exponent H does not vary much with the material, but can change with the observation scale. In particular, one observes a transition at material-dependent length ξ between two scaling different regimes.

At large-scale $\Delta r \gg \xi$, the scaling roughness exponent H is lower than 0.5, typically in the range $0.35 - 0.45$, corresponding to an antipersistent behaviour. In this regime, the crack front is modelled as a continuous line, whose interactions are governed by a long-range elasticity that can be exactly derived from fracture mechanics, a theoretical framework that describes failure as a propagation of a crack line [147–149]. These so-called models of elastic lines in random media provide a fairly precise description of experimental fracture surfaces in this regime.

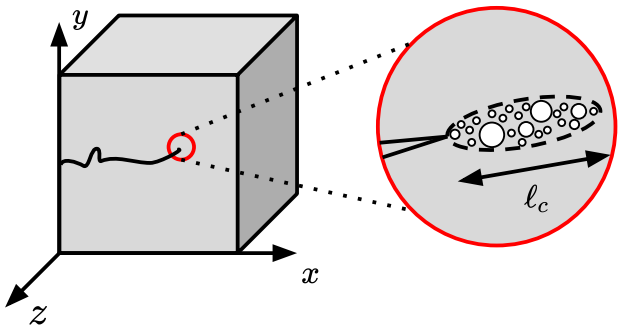

Figure 4.3: The microscopic view of failure. At large scale, failure results from the seemingly continuous propagation of a crack. Yet, zooming at the crack vicinity, one observes that cracks grow by coalescing cavities in a so-called *fracture process zone* of size ℓ_c.

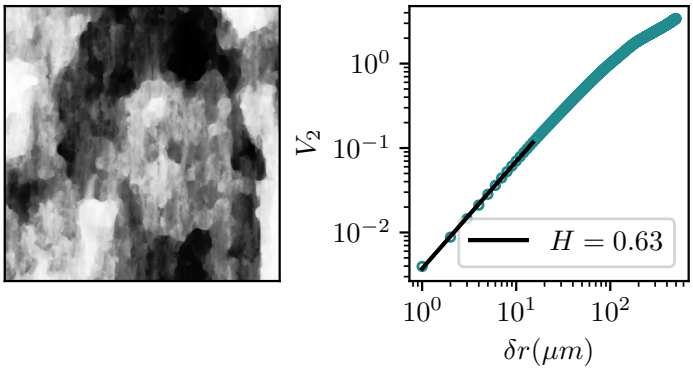

Figure 4.2: Fracture surface of a metallic alloy, measured by optical profilometry. (Left) Quantile representation of the height field $h(x, y)$ in 256 grayscale levels. The resolution is 1000x1000 with 1pixel $= 1\mu m$. (Right) Variogram function for ($q = 2$) calculated along the propagation direction .

For $\Delta r < \xi$, fractures surfaces display persistent scaling ($H > 1/2$), as shown in Fig. 4.2. This observation is not consistent with the predictions drawn from fracture mechanics. It was then proposed that at this scale, the failure progresses in the material through the sampling of damage cavities, as illustrated in Fig. 4.3. These cavities are expected to initially nucleate from defects present in the material microstructure, and then grow until they finally coalesce to form new surfaces in the fracture plane.

While fracture mechanics models [46, 56, 146, 150] have been employed to explain the scaling features of frazcture surfaces at scale $\Delta > \xi$, discrete coalescence models, based for example on the concept of gradient percolation [151], have been proposed at smaller scale $\Delta r < \xi$.

Intermittency – A puzzling feature of fracture surfaces is the presence of intermittent non-Gaussian statistics at small scale $\Delta r < \xi$ [143, 145, 152]. This behaviour manifests from the distribution of height

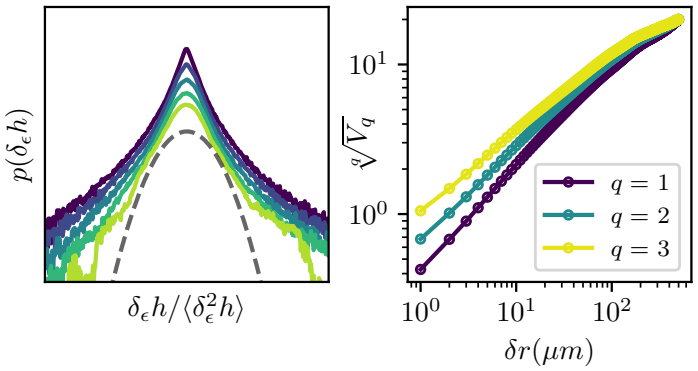

Figure 4.4: Characterization of intermittent behaviours. (Left) Empirical p.d.f of jumps increments $\Delta_\epsilon h$ for $\epsilon \in 1, 2, 4, 8, 16$ pixels (Top to Bottom).(Right) Rescaled variograms $\sqrt[q]{V_q}(\Delta \boldsymbol{r})$, showing $\zeta_q \neq qH$

increments $\rho_\epsilon(\Delta h) = \mathbb{P}[h(\boldsymbol{r}+\boldsymbol{\epsilon}) - h(\boldsymbol{r})]$, as shown in Fig.4.4. This intermittency ultimately smooths out to Gaussian statistics, as the observation scale ϵ increases beyond ξ. Intermittency also manifest in the multifractal scaling of fracture surfaces which can be investigated from the scaling of the generalized variograms:

$$V_q(\Delta \boldsymbol{r}) = \langle |\Delta_{\Delta r} h|^q \rangle = K_q \Delta r^{\zeta_q}, \tag{4.2}$$

where ζ_q is the so-called scaling exponent spectrum. In the monofractal case, one gets $\zeta_q = qH$, and the rescaled variograms $\sqrt[q]{V_q}$ collapse to one another. This is not the case for fracture surfaces, as shown in Fig. 4.4. This behaviour, first reported in [145] was further characterized in [143].

Big whorls, little whorls – Interestingly, the properties reported above are reminiscent of fluid turbulence: (i) Velocity increments display a quasi-universal scale invariance regime ($\zeta_3 = 1$) [33, 35]. (ii) This regime is surrounded by two other ones: smooth at small dissipative scales ($H \approx 1$), and system size dependent at large scales. (iii) Velocity increments display the same fat-to-thin tail transition, as the observation scale increases [153]. (iv). The scaling exponent spectrum deviates from $\zeta_q = qH$ [154]. However, we can observe a striking difference regarding the dynamical organization of the self-similar structures. In 1922, Richardson observed that turbulent eddies [39] seemed to split from one another, forming smaller and smaller structures. This so-called *direct cascade* can manifest in various fashions, as Jonathan Swift beautifully illustrated in his *On Poetry: a Rhapsody* (1733):

> *So, nat'ralists observe, a flea*
> *Hath smaller fleas that on him prey;*
> *And these have smaller yet to bite 'em,*
> *And so proceed ad infinitum.*

...

Thus every poet, in his kind,
Is bit by him that comes behind:
Who, though too little to be seen,
Can teaze, and gall, and give the spleen.

This construction inspired Richardson [39] in the following:

Big whorls have little whorls,
Which feed on their velocity,
And little whorls have lesser whorls,
And so on to viscosity.

It was found years later by Kolmogorov that the cascade was more quantitatively related to a kinetic energy transfer, hence making of Richardson's works the premises of 100 years of turbulence theory [37, 155].

For fracture problems, damage cavities emerge at a microscopic scale and the then increases through the coalescence with other cavities, ultimately leading to failure through a complex process of void coalescence. The cascade in fracture would then stream in an inverse direction, and we may instead propose:

As damage voids form in the mass,
They coalesce into small cracks,
And these small cracks merge in large ones,
Persistently building their path.

In the second part of the thesis, we will tackle the characterization of fracture surfaces by raising the following questions. Can we build a minimal model of random fields that reproduce the scaling properties of fracture surfaces? How do these artificial surfaces compare with experimental ones ? How far can we learn about the damage mechanisms at the origin of fracture surface morphology, and can we get insights on this microscopic dissipation mechanism that ultimately controls the failure resistance of materials ?

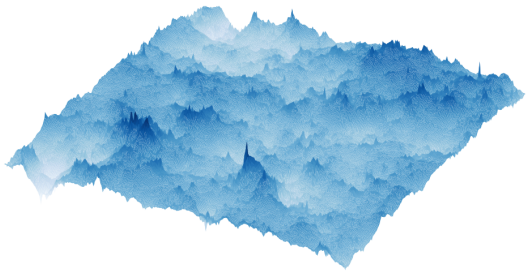

Figure 4.5: Synthetic multifractal field. The non-Gaussian statistics appear under the form of pikes, cliffs and other singularities. However, we will see in Chapter. 4 that some features of these artificial fracture surfaces differ from experimental ones.

In Chapter. 4, a powerful yet simple method for the generation of multifractal fields is introduced, and allows for direct comparisons with experimental fields. In Chapter. 5, a more exhaustive investigation of experimental rock fracture surfaces reveals the peculiar properties of their steepest structures, and their relation with the mechanical *Fracture Process Zone* length ℓ_c which controls the cohesive properties materials.

The result of both chapters should be included in forthcoming publications, Ref. [4] being one of them.

Part I

STATISTICAL PHYSICS APPROACH TO IMAGE ANALYSIS AND PROCESSING

1

A FIRST EXPERIMENT ON QUANTITATIVE AESTHETICS

When in doubt, optimize for interestingness.

— Paul Graham [156]

This chapter is largely based on [1], written in collaboration with Alexandre Darmon, Jean-Philippe Bouchaud and Michael Benzaquen, and the results of which are based on my doctoral and pre-doctoral works. Some minor changes and additions were implemented, for overall consistency.

1.1 INTRODUCTION

What makes a beautiful image? Is there such a thing as universal beauty? These puzzling yet fascinating questions have been tackled many times in the past within several disciplines, including philosophy, psychology, arts or mathematics [101, 157–168]. According to Kant, *Is beautiful that which pleases universally without a concept* [169]. The idea of an intelligible beauty appeared in ancient Greece, where Nature was believed to be a *cosmos* constituting a principle of order and harmony. The proportions between the constitutive elements of each being are rightfully defined, whether it is a work of art, a living organism or a city [170]. Following the Greeks, the Baroque and Renaissance artists also believed in a universal beauty, and it is striking that their arts partially rely on a mathematisation of the artistic representation (symmetry [165], proper geometric proportions as given by the *golden number* [157], etc.). In other terms, the belief that there must be scientific grounds to the conception of what is artistic or beautiful has been out there for quite some time. Yet, the very idea of a universal beauty is a longstanding debate which has known many ruptures through the history of art [158] and still opposes a number a great modern thinkers.

Physicists' interest in the subject is more recent. Stephens *et al.* [126] showed that natural images were critical in the thermodynamic sense and proposed a theory for the *Thermodynamics of Natural Images*. While, as pointed out above, many would consider *quantitative aesthetics* to be an oxymoron, and indeed it would be rather nonsensical to aim at building a fully consistent theory of pictorial art, we, as physicists, believe there is some room for a quantitative analysis. For example one could easily argue that an aesthetically appealing image often results from a subtle balance between regularities and surprises. Indeed, it

seems rather plausible to think that while one might find dull an image that is too regular (no surprises), one may also feel lost in front of an image with no recognisable shapes or structures to hang on to (too much surprise). As argued in [47], *Total chaos is disquieting. Too much regularity is boring. Aesthetics is perhaps the territory in-between*. Provided one agrees with such statements, these ideas clearly suggest that one could design an entropy-like function to quantify this subtle and complex equilibrium.

To address this question we run a large-scale survey in which people are asked to sort by preference two different sets of random images well distributed along three measures of entropic complexity: Fourier Magnitude's slope, fractal dimension and compression rate.

The chapter is organised as follows. We first introduce simple complexity metrics in Sec. 1.2 that motivate straightforward image generation methods. We then present and analyse the results of the survey in Sec. 1.3. Finally in Section. 1.4, we argue that algorithmic complexity of the coarse-grained images is a rather good proxy for image appreciation. We conclude in Section. 1.5.

1.2 SIMPLE COMPLEXITY MEASURES FOR IMAGES

There exist many possible measures of image complexity, relying on e.g. their mathematical properties [171, 172], their physical properties [126, 173, 174], or even their cognitive impact [100, 118, 175]. Here we choose to work with three simple measures that can be easily computed unequivocally for any digital 2D image. The first one is the *magnitude slope* α defined as the logarithmic slope of the radially averaged Fourier magnitude $\mathcal{S}(k) = \langle \hat{u}(k,\theta) \rangle_\theta$, where $\hat{u}(k,\theta)$ denotes the Fourier Transform of the image grayscale intensity $u(r,\phi)$, and $\mathcal{S}(k) \sim |k|^\alpha$. The second is the *fractal dimension* d_f computed using the Minkowski-Bouligand box-counting method [176]. After transforming the image to B&W using an intensity threshold ensuring two equally-populated levels [126], the fractal dimension follows $N(\epsilon) \sim \epsilon^{-d_f}$ where $N(\epsilon)$ is the number of boxes of size ϵ containing both black and white features. The third is the *compression rate* or *algorithmic complexity* τ computed as the ratio between the size of the PNG image and its uncompressed maximum size equal to $N_x \times N_y$ bytes (1 byte = 8 bits per pixels).

1.3 THE EXPERIMENT

1.3.1 *Generating abstract images*

In order to remove possible cognitive and cultural biases, we choose to design our experiment with abstract images randomly generated using two of the complexity measures presented above. The first set

of images (Fig. 1.1a) is generated by *reverse-engineering* the Fourier Magnitude property: setting $\hat{u}(k,\theta) = k^{\alpha} e^{i2\pi\eta(k)}$, where η is drawn from a uniform distribution on $[0,1]$ with $\langle \eta(\boldsymbol{k})\eta(\boldsymbol{k}')\rangle \propto \delta_{\boldsymbol{k}\boldsymbol{k}'}$[1], and taking the inverse Fourier Transform of $\hat{u}$ allows to produce a series of random grayscale images $|u(r,\phi)|$ with controlled Magnitude slope [100, 102, 177]. Table 1.1 gathers the computed complexity measures

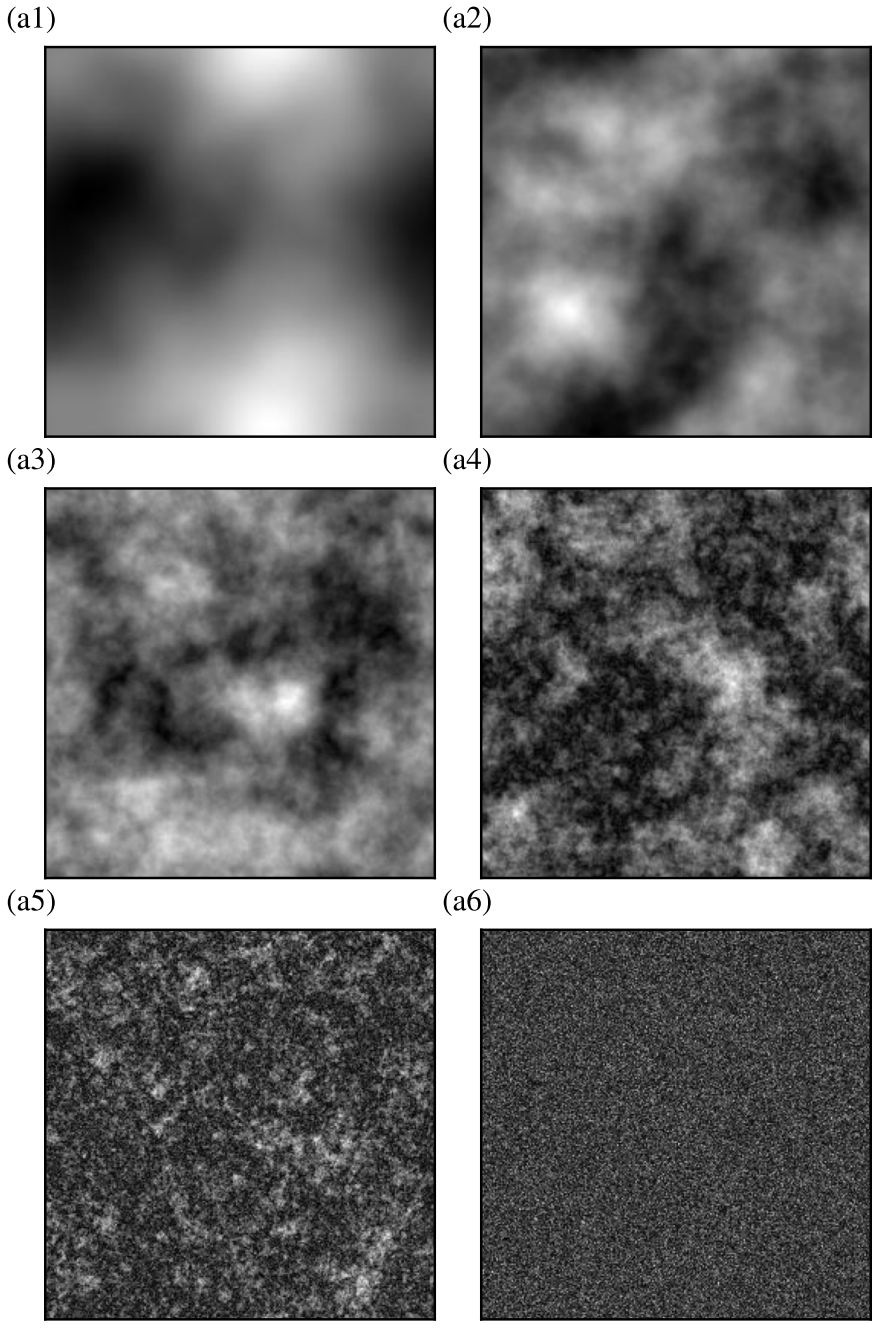

α, d_f and τ of the 256×256 images displayed in Fig. 1.1a. As one can see both d_f and τ are increasing functions of α, comforting our choice

1 We shall see in Ch. 2 that such fields belong to a class of well known random Gaussian fields.

of complexity measures and indicating that there is a clear correlation between the spectral, fractal and algorithmic properties.

The use of a second set of images was motivated by the remarks of some survey participants. When asked why they had preferred certain images, they responded their picks reminded them of cloudy skies or galactic landscapes. With the aim of producing more abstract images, we used an alternative method, now based on reverse-engineering

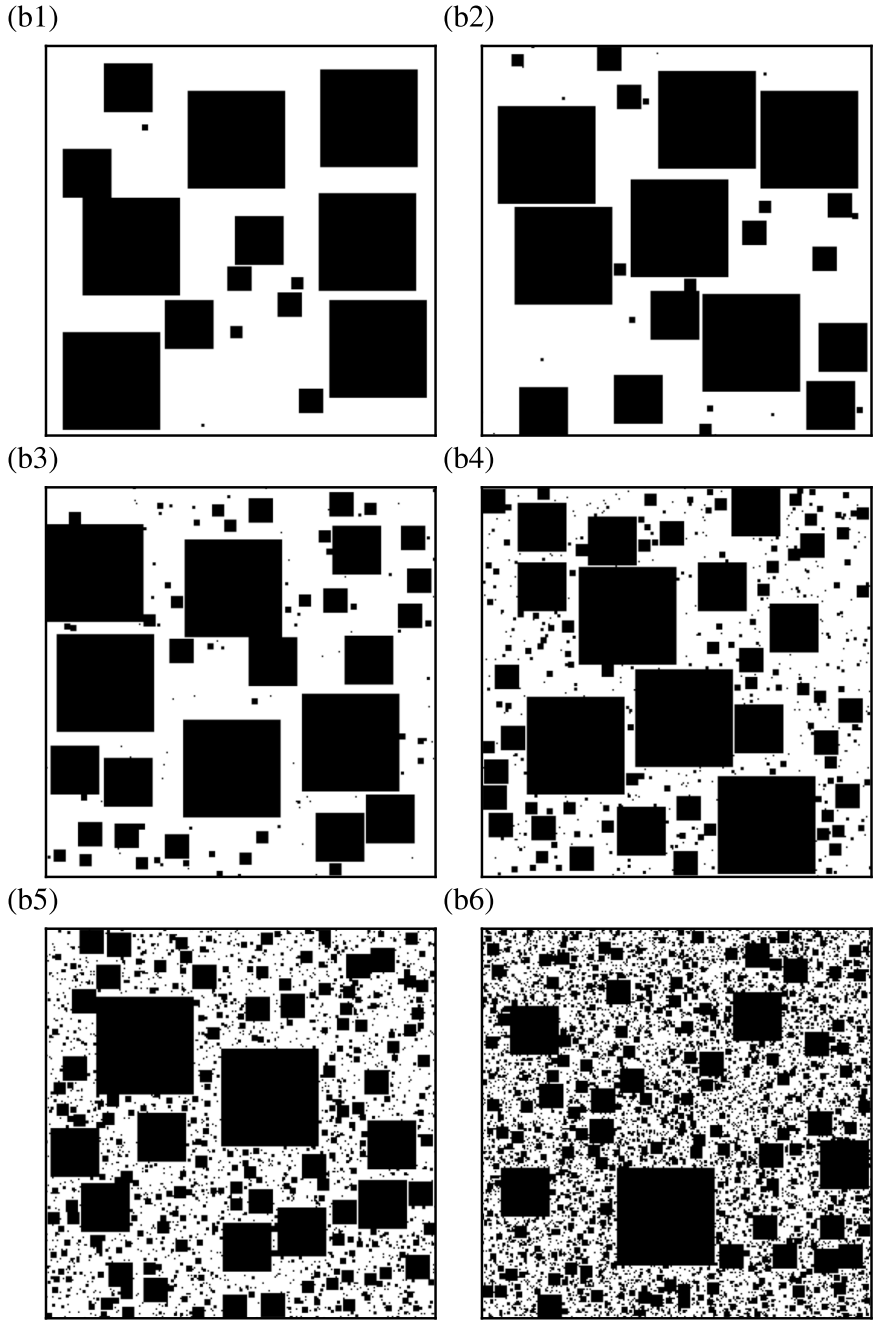

Figure 1.1: (a) Fourier Magnitude-generated images, and (b) Box-counting-generated images, both series with increasing complexity from left to right. These images were used for our large-scale survey.

the Minkowski-Bouligand box-counting method (Fig. 1.1b). Black squares of size $\epsilon = 2^k$, $k \in [1, k_{\max}]$, drawn from the distribution $N_x(\epsilon) = A\epsilon^{-x}$ are randomly added to a white canvas of size 256×256 with the condition that they do not overlap. The upper boundary $k_{\max}$ is chosen such that the biggest squares occupy at most 1/16th of the total surface, $k_{\max} \leq \log_2(256) - 2 = 6$. We also enforce that the total fraction of black pixels does not exceed 1/2 [2]. Here again the complexity measures appear to be increasing functions of one another (see Tab. 1.1).

Table 1.1: Complexity properties of the images presented in Fig. 1.1.

	a1	a2	a3	a4	a5	a6
α	-3.96	-2.47	-1.95	-1.42	-0.76	0
d_f	1.22	1.33	1.58	1.87	1.99	2.0
τ	0.186	0.325	0.472	0.711	0.902	0.956
	b1	b2	b3	b4	b5	b6
α	-2.14	-1.78	-1.56	-1.32	-1.04	-0.77
d_f	1.42	1.51	1.62	1.75	1.88	1.95
τ	0.012	0.014	0.022	0.044	0.095	0.16

1.3.2 *Survey design and deployment*

In 2013, Spehar and Taylor [177] conducted a survey on twenty-six academics, using black and white computer generated images with increasing fractal dimension. They found a reversed U-shaped relation between image appreciation and fractal dimension, with an aesthetic optimum for $d_f \approx 1.5$, allowing to argue that we indeed tend to prefer images with intermediate complexity, see also [100, 102]. Curious of their results, we conducted a larger scale experiment intended for a larger panel (about a thousand participants with different backgrounds), using the images presented in Fig. 1.1. Our question at this stage is similar: is there a link between the statistical properties of our generated images and the tendency of people to appreciate them?

Survey methods design constitutes a strand of research on its own [178]. For optimal results the selection task must be simple and display the minimum amount of information to the interviewee. While the common five-star ratings only take a time proportional to the number of images to score, these have been shown to be weighted by extreme grades, the utility given to intermediate grades being far from linear [179]. Five-star ratings image-by-image can also be rather disorienting due to the lack of reference. Another option is image

2 Note that while our method is motivated by fractal considerations, x does not match the measured fractal dimensions displayed in Tab. 1.1, due to both finite size effects and the non-overlapping boxes constraint.

classification, where the interviewee is presented with the whole set of images and is then asked to sort them by preference. While also time-efficient, presenting all the images at once might strongly induce people into intuitively recognising other features, such as complexity, and ending by sorting them by something else than preference. Finally, the *Battle survey* consists in presenting the interviewee with two images, asking her/him to choose the one she/he prefers, and repeating the operation until all possible combinations of two images have been addressed [160, 180]. While less time-efficient (with $N(N-1)/2 = O(N^2)$ battles, for $N = 6$ images one needs 15 rounds to complete the survey), this method beats the other shortcomings mentioned above, and people usually feel more comfortable with such a binary task, intellectually less challenging. We thus choose the latter method.

We conducted two slightly different surveys. The panel for the first survey consisted of colleagues from CFM and Ecole Polytechnique as well as students and relatives, adding up to ≈ 350 people, who were asked to participate without any financial incentive. While probably slightly biased population-wise, these are the results as we are most confident with, since we believe people in such a panel completed their tasks selflessly and honestly. To run this survey we used the Zooniverse platform [181] which provides a rather intuitive interface. The 15 two-image sets for each series were generated using a python algorithm that concatenated the images in a random order and attributed them a different name so that the interviewee couldn't find hidden information. Upon completion of the survey, to establish a global ranking of the images we attributed them a score according to the following rule: if image i wins (resp. looses) a battle, its score S_i increases (resp. decreases) by $1/N_i$ where N_i denotes the number of battles in which i was involved [3]. To obtain a score $S_i \in [0, 1]$ we then transform it as $S_i \to (S_i + 1)/2$.

1.3.3 *Results*

The results are plotted as a solid black line in Fig. 1.2. Remarkably, the preferred images appear to be a4 a5, and b4 b5 respectively, both corresponding to α close to 1. To note, interestingly $\alpha \approx 1$ is often associated to the spectral properties of natural images [121, 126] and visual arts [171]. Discussions with voters revealed that they found their favorite images to be the most *harmonious* and *well balanced*.

In order to increase the size and diversity of the panel, we ran an other experiment on the Mechanical Turk platform [183], in which participants are paid a small amount of money to participate (we reached ≈ 600 panelists). However, there was a significant risk that

3 Note that N_i was not exactly equal to N since a small number of participants stopped before completing the 15 battles.

people would answer randomly as they do not, by definition, participate selflessly and in good will as in our first experiment. We thus formulated the question differently in order to encourage non-random participation: much like in Keynes' famous beauty contest [68], people were asked to pick the image which they thought would be preferred by the majority and told they would not get paid if their overall choices fell too far off the average (needless to say, we did process all of the

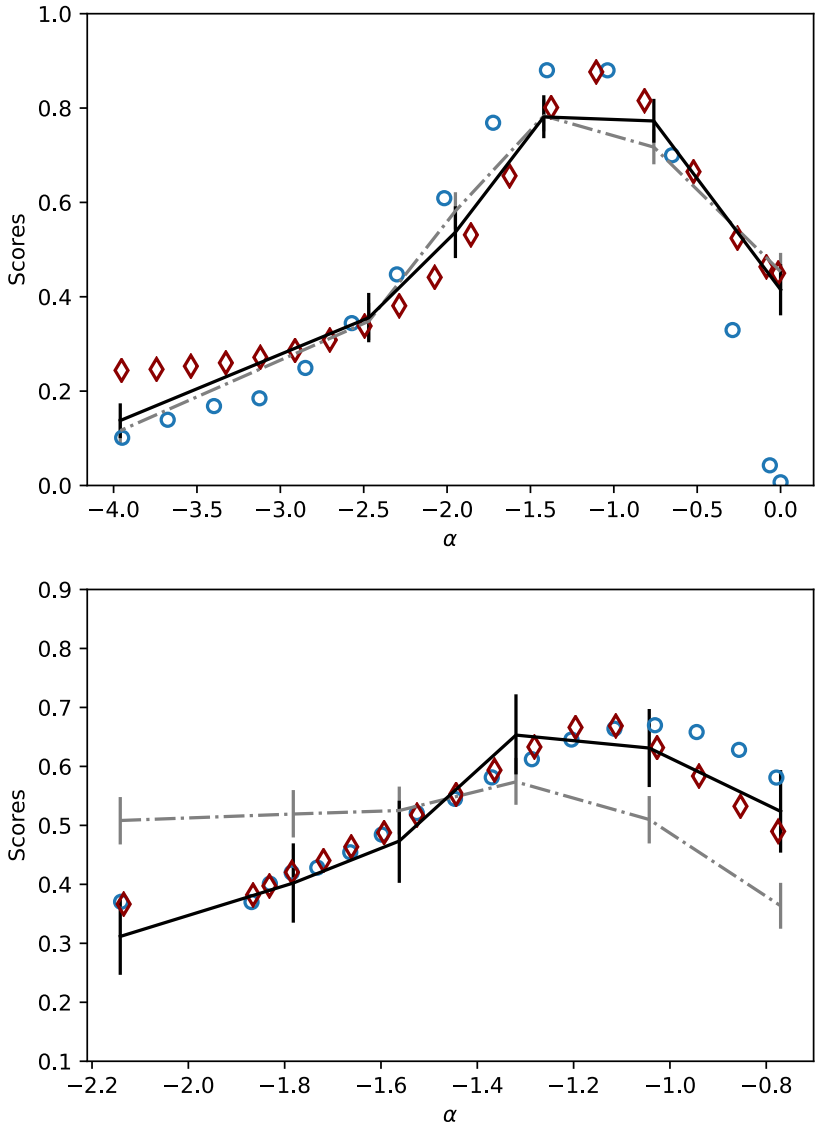

Figure 1.2: Results of the two different surveys (Zooniverse: solid black line, Mechanical Turk : dash-dotted gray line). The red diamonds markers indicate the structural complexity τ_{cg} defined below. We have rescaled and shifted vertically τ_{cg} to show that the maximum scores also correspond to maximum structural complexity. The blue circles reflect the complexity measure proposed in [25]. Top: image series of Fig. 1.1(a). Bottom: image series of Fig. 1.1(b). Error bars reflect the 95% confidence interval using the bootstrap method [182].

data, regardless of its distance to the average). Results are presented in Fig. 1.2 (dash-dotted gray line). While probably introducing other biases, the results displayed good agreement with that of the initial selfless survey. Also note that while all results are fully consistent for the first set of images (Fig. 1.1(a)), the second experiment leads to a less pronounced maximum for the image series of Fig. 1.1(b), with scores on average closer to $S = 1/2$ than they were for the very first experiment.

1.4 STRUCTURAL COMPLEXITY

1.4.1 *A metric for harmony and equilibrium*

Very much like entropy is used to measure the disorder in a physical system, we would now like to see whether there might exist a statistical proxy to estimate an image's *harmony* and *equilibrium*, as described by our survey participants. Given the complexity measures described above, images with low complexity display very simple shapes (a1 b1), and images with very high complexity display a large amount of white noise (a6 b6). Our survey revealed that maximum appreciation is obtained for intermediate complexity suggesting the following question: could it be that an aesthetically appealing image results from a subtle balance between complexity and regularity? And if so, can we find an associated statistical measure? The work of Desolneux *et al.* [172] clearly resonates with such questions. Guided by the idea that there is no perceptual structure in white noise, the authors attempted to characterise forms and structures and in particular defined unusual features or *Gestalts* as *sets of points whose (...) spatial arrangement could not occur in noise*. Their ideas can be easily illustrated with the coffee and cream dynamics [22].

1.4.2 *Computing structural complexity*

Consider the experiment in which plain cream is left to slowly mix with plain coffee. While the initial and final states of such a system display very regular homogeneous structures, the transitional regime displays interesting and *complex* mixing patterns as the cream/coffee interface slowly disappears. So far we have used the term *complexity* rather imprecisely and it is now time to distinguish more rigorously two sorts of complexity. The first is *entropic complexity* measuring the amount of information in the image, which in the coffee experiment can only be an increasing function of time according to the second law of thermodynamics; the second is *structural complexity* accounting for the amount of features outside of the noise, which here is a non-monotonous function of time displaying a maximum at intermediate stages where the non-trivial mixing patterns are most

significant. Entropic complexity is well described by α, d_f or more commonly τ. Structural complexity, in a sense, measures *noiseless* entropic complexity or *interestingness*.

Guided by the work of Aaronson *et al.* [22] we computed structural complexity as a *noiseless* entropy. More precisely we apply a coarse-graining procedure of given radius r_{cg} on the B&W images and then compute their algorithmic complexity τ_{cg} which we call structural complexity in the following [4]. The colour of a given block is determined by its black to white pixel ratio $\eta \in [0,1]$: white if $\eta \leq \delta$, gray if $\delta < \eta \leq 1-\delta$, and black for $\eta > 1-\delta$ where $\delta \in]0,1/2[$ is a given threshold. Figure 1.3 illustrates the procedure on images a1, a4 and a6; after turning them into B&W (second column), the coarse-graining procedure is applied (third column). As one can see, image a1 is barely changed (just a thin gray line at the domain boundaries) and we thus expect $\tau_{cg} \approx \tau$, image a4 is slightly denoised while letting its structures invariant $\tau_{cg} \lesssim \tau$, image a6 however is strongly denoised as the coarse-graining procedure has left it almost plain gray suggesting $\tau_{cg} \ll \tau$. The structural complexity computed for both sets of image is plotted on Fig. 1.2 as dark red diamonds. As expected, $\tau_{cg}(\alpha)$, or equivalently $\tau_{cg}(d_f)$ and $\tau_{cg}(\tau)$, are non-monotonous functions displaying a maximum for intermediate values of α, d_f and τ. Note that the y-axis in Fig. 1.2 is arbitrary (structural complexities and scores don't have the same dimensions) and thus only the shape of the curves should be compared, which we facilitate by superimposing them (vertical linear transformation $\tau_{cg} \to a\tau_{cg} + b$). Furthermore, the scale parameter r_{cg} and the threshold η can be used as fitting parameters; in particular r_{cg} acts as the cutoff of a low-pass filter which erases high frequency spatial features, increasing it tends to lowers the right most red markers and shift the maximum to the left. Up to a multiplicative factor, best fits are obtained for $(r_{cg}, \eta) = (7, 0.23)$ for the first set and $(13, 0.12)$ for the second. The agreement between theory and experiments is quite convincing. Not only do the maxima coincide, but also the overall shape of the curves is similar. Note that such good agreement is not r_{cg}- and δ-sensitive provided the latter are kept within a reasonable range. This quantitatively supports the idea that structural complexity is a good proxy for average image preference. Also note that the alternative interesting measure of structural complexity proposed in [25] (see blue circles on Fig. 1.2), though more *ad hoc* than ours, appears to also correlate well with our survey data.

4 Spehar *et al.* [102] showed that the preference curve was hardly affected by the gray scale to B&W transformation. For the sake of simplicity we thus choose to apply the coarse-graining procedure to B&W images.

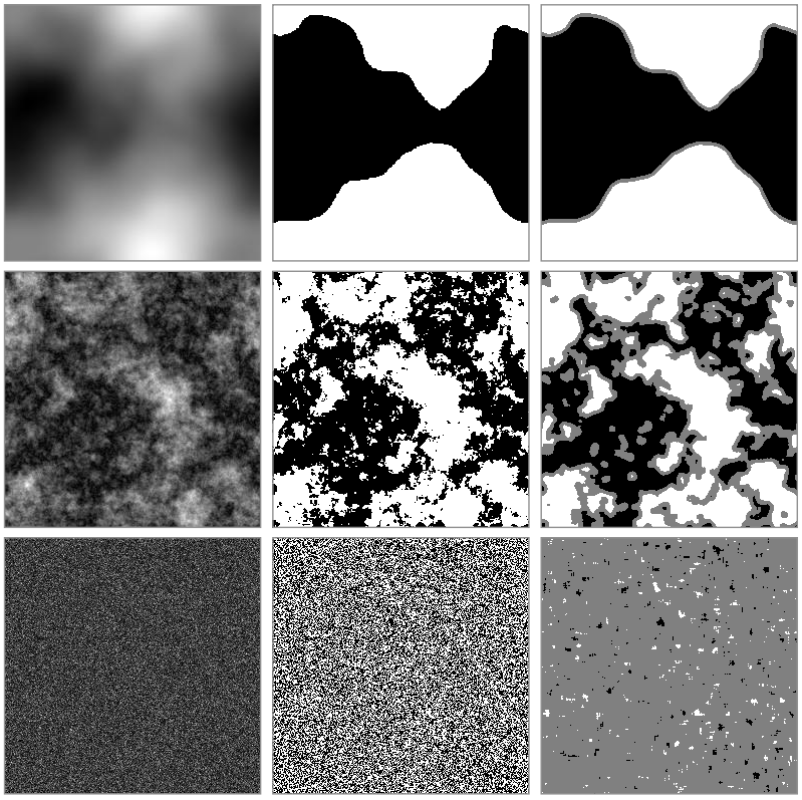

Figure 1.3: Illustration of the coarse-graining procedure on images a1, a4 and a6, with $r_{cg} = 7$ and $\delta = 0.23$.

1.5 CONCLUSION

Let us summarise what we have achieved. Using two random-image-generation algorithms, we produced two different sets of abstract images spanning a broad range of entropic complexity, measured by three different quantities. We then designed and ran a large-scale experiment for image classification and found that preference peaks about complexity criteria matching that of natural images, perhaps indicating that people's preferences are influenced by their natural environment. Finally, our main contribution is to show that a "noiseless" entropy (that captures interesting structural features only) accounts well for the experimental results on image appreciation. It is interesting to speculate that, when confronted with images, the human brain may actually conduct the same kind of geometrical coarse-graining, trying to extract forms and structures while erasing uninteresting noise, or as put by the *Gestalt theory* [184]: filter meaningful perceptions from chaotic stimuli. As a result, the excess of noise and lack of forms may lead to unconscious rejection of structureless images. In the next chapter, we continue our investigation on multi-scale entropy contributions to analyse natural images. We will introduce a recent formalism designed to evaluate the information content of high-dimensional samples.

1.6 TAKE-HOME MESSAGE

An intuitive viewpoint:

> *Total chaos is disquieting. Too much regularity is boring. Aesthetics is perhaps the territory in-between.*

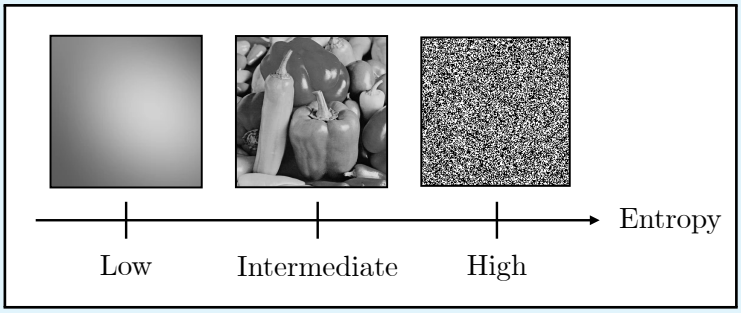

We test that assertion by building a large scale survey experiment on visual appreciation of abstract images.

We find that image appreciation correlates really well with a noiseless entropy measure: Structural Complexity.

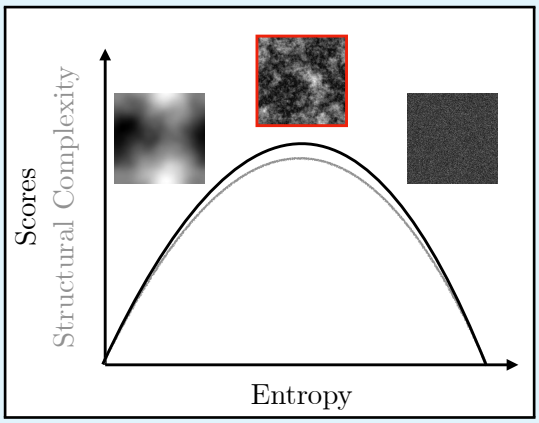

Interestingly enough, the spectrum of most appreciated visuals strongly resembles that of natural images.

2 MULTISCALE RELEVANCE FOR IMAGE ANALYSIS

La perfection n'est pas de ce monde et certainement pas dans mon métier. En tout cas, tous les jours on se remet en question, on essaie de s'améliorer, demain on sera meilleur qu'hier.

— Alain Ducasse

This chapter is a reorganization of the published paper [3], written in collaboration with Alexandre Darmon, Iacopo Mastromatteo, Matteo Marsili and Michael Benzaquen, and the results of which are based on my doctoral works. Some minor rearrangements and supplemental informations were added, to ensure consistency with Chapter. 3.

2.1 INTRODUCTION

Recent advances in image processing have benefited from the emergence of powerful learning frameworks combining efficient architectures [185–187] with large high-quality databases [188, 189]. In particular, neural networks, layering simple linear and non-linear operators such as convolution matrices or activation functions, have proven to be very efficient to classify or generate high dimensional data. They are now able to capture similarities between images with unprecedented success. However, while their performance increases with the depth of the architecture, it is generally at the cost of physical interpretation. Understanding the learning dynamics and the statistical features of the resulting images remains a challenge for the community [190, 191].

Before the advent of machine learning algorithms, tasks such as compression [192, 193], denoising [86] or edge detection were (and in some cases still are) performed using signal processing methods. Among the classical approaches, the first kind is based on specific measures, such as the widely used Peak Signal-to-Noise Ratio (PSNR) [194], that are built upon common signal processing metrics (Euclidian distance, power spectrum, etc.). The second family uses vision based experiments to construct semi-empirical measures of similarities, such as the Structural Similarity Index (SSI) [195]. In both cases the approach is fully deterministic, which means that stochastic properties like roughness, stationarity, or local correlations are ignored.

In the context of statistical physics, the problem of high dimensional data inference has recently been addressed using a novel, fully agnostic, approach. Developed to measure specific properties of finite size samples [23], the approach consists in assessing the influence of a prescribed compression procedure over simple entropy measures.

Applications in biological inference [20], finance [127], language models [23] or optimal machine learning [129, 130] have already shown exciting results. In this paper, we adapt the latter formalism to image analysis and image processing, focusing specifically on the case of natural images. Natural scenes or landscapes have long been studied as they display distinguishable statistical features such as scale invariance [120, 124, 125], non-Gaussianity [123], or patch criticality [126].

The outline of the chapter is as follows. In Section 2.2, we introduce the Resolution/Relevance formalism using an illustrative example, and adapt it to the purpose of image analysis. In Section 2.3, we analyse a class of parameterizable images, that is random $1/f^{\alpha}$ Gaussian fields, and introduce the Multiscale Relevance (MSR). In Section 2.4, we extend the analysis to natural images and their gradient magnitudes. We discuss meaningful statistical similarities with the synthetic Gaussian fields. In Section 2.5, we show how the MSR approach can be used in the context of a classic image processing task.

2.2 THE RESOLUTION/RELEVANCE FRAMEWORK

Here we present the information-theoretic framework that was recently introduced by Marsili *et al.* [23] for the agnostic analysis of high-dimensional data samples and their behaviour under compression procedures. Relevant metrics are derived from simple statistics of the compressed samples.

2.2.1 *Tradeoff precision/interpretability*

Let us consider the problem of binning, namely clustering samples of a random variable X into groups characterized by a similar value of X. If the sampled data points $\mathcal{S} = \{x_1, \ldots, x_N\}$ all take different states (e.g. when the distribution of X is continuous) the empirical distribution is a Dirac comb. In order to gain insight into the sampled variable, one can visualize the data by using histograms with well chosen bins/boxes. Indeed, this procedure enforces the emergence of structure by reducing data resolution through compression, allowing for more interpretability. One can then make assumptions on the underlying process and find the optimal parameters to best describe the data.

We illustrate this intuition by sampling $N = 100$ realizations of a Gaussian variable $X \sim \mathcal{N}(0, 1)$ in Fig. 2.1. The data are binned into n identical boxes, for three different values of $n = 5$, 23 and 400. We also define the bin width ℓ as a compression parameter transforming the original sample $\mathcal{S}$ into a compressed sample $\mathcal{S}^{\ell}$. The compression step consists in replacing each data point by its corresponding histogram bar index. Figure 2.1(a1) (large ℓ) displays a situation of *oversampling*. With only five bins a considerable amount of data resolution is lost.

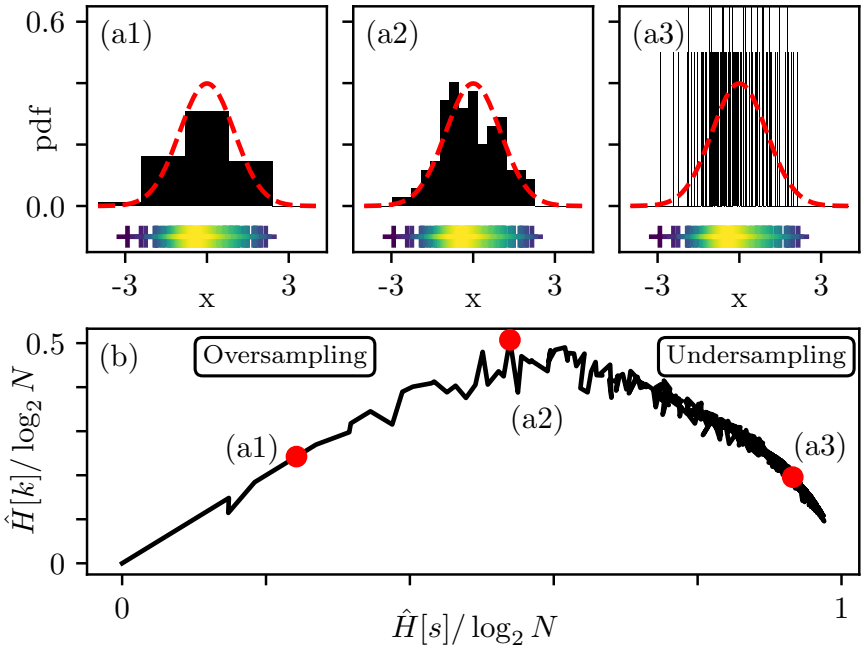

Figure 2.1: Relevance analysis of a Gaussian distribution sample ($N = 100$). (a) Influence of the number of bins n on the normalized histogram (black bars), for (a1) $n = 5$, (a2) $n = 23$ and (a3) $n = 400$. The red curve corresponds to the underlying distribution. The bottom markers (+) represent the initial sample data points with color indicating local data density. (b) Resolution/Relevance curve.

On the contrary, Fig. 2.1(a3) (small ℓ) corresponds to an *undersampling* regime, with very narrow bins (mostly containing only one data point) and a resulting distribution close to a Dirac comb. Figure 2.1(a2) (intermediate ℓ) appears as a reasonable compromise in which the histogram is visually close to the generator density, indicating we might be close to the optimal level of data compression. From the latter observation, one is tempted to go for a Gaussian model, with suitable estimators for the mean and variance. However such decision solely relies on a specific compression level, and thus does not make full use of the sample at play.

The formalism that we introduce in the next section provides a principled framework to connect the choice of the compression level with an optimality criterion that is agnostic to the nature of the generative model from which the data is sampled.

2.2.2 *Resolution and relevance*

Previous work from Marsili *et al.* [127] addressed the issue of the *overampling/undersampling* transition by introducing observables that allow one to monitor changes in a reduced sample $\mathcal{S}^\ell = \{s_1^\ell, \ldots, s_N^\ell\}$ obtained by compressing $\mathcal{S}$ with a parameter ℓ. First, let us consider

k_s^ℓ the number of data points of identical state s and m_k^ℓ the number of states appearing k times in $\mathcal{S}^\ell$. It follows that $\sum_s k_s^\ell = \sum_k k m_k^\ell = N$. For example, in the compressed sample displayed in Fig. 2.1(a1), values taken by k_s^ℓ are $\{2, 26, 49, 23, 0\}$, and since each bar in the histogram has a different height, one has $m_2 = m_{26} = m_{49} = m_{23} = m_0 = 1$ and $m_k = 0$ otherwise.

One can then define the *Resolution* $\hat{H}^\ell[s]$ and *Relevance* $\hat{H}^\ell[k]$ as:

$$\begin{cases} \hat{H}^\ell[s] &= -\sum_s \frac{k_s^\ell}{N} \log_2 \frac{k_s^\ell}{N}, \\ \hat{H}^\ell[k] &= -\sum_k \frac{k m_k^\ell}{N} \log_2 \frac{k m_k^\ell}{N}. \end{cases} \tag{2.1}$$

The *Resolution* is the entropy of the empirical distribution $\{p_s^\ell = k_s^\ell / N\}_s$ and describes the average amount of bits needed to code a state probability in $\mathcal{S}^\ell$. The compression clusters data points together hence reducing the average coding cost. The *Resolution* is maximal for raw data and monotonically decreases with ℓ, until it reaches the minimally entropic fully compressed sample. The *Relevance* is the entropy of the distribution $\{q_k^\ell = k m_k^\ell / N\}_k$, that is the probability that a data point sampled from $\mathcal{S}^\ell$ appears k times in the sample. This is a compressed version of p_s^ℓ, where identical frequency states are clustered, dropping their label s in the process. Knowing q_k^ℓ is then sufficient to build a histogram without labels, and is equivalent to assuming indistinguishability of states sampled the same number of times. Sorting them in decreasing frequency values would yield the famous Zipf plot. In the end, the *Relevance* encodes the height of each bar and is maximal when $\{k m_k^\ell / N\}_k$ is uniformly distributed, leading to $m_k \propto k^{-1}$. We reported in Tab. 2.1 the typical sampling situations and their corresponding value in Resolution/Relevance.

Coming back to the Gaussian sampling example, Fig. 2.1(b) displays $\hat{H}^\ell[k]$ as function of $\hat{H}^\ell[s]$, obtained by varying ℓ. Corresponding values for $n = 5$ (a1), $n = 23$ (a2) and $n = 400$ (a3) are highlighted. Note that (a2) maximizes Relevance while (a1) and (a3) respectively correspond to oversampling and undersampling. Let us emphasize at this point, that, despite the visual impression in this specific example, the sample (a2) does not necessarily minimize the distance between

Table 2.1: Typical sampling situations.

Situation	Sampled States	$\{m_k\}_k$	$H[s]$	$H[k]$
Full Oversampling	Identical	$m_N = 1$ $m_k = 0$	0	0
Full Undersampling	Distinct	$m_1 = N$ $m_k = 0$	$\log N$	0
Intermediate sampling	Intermediate	$m_k \propto k^{-1}$	H_0	$\max H[k]$

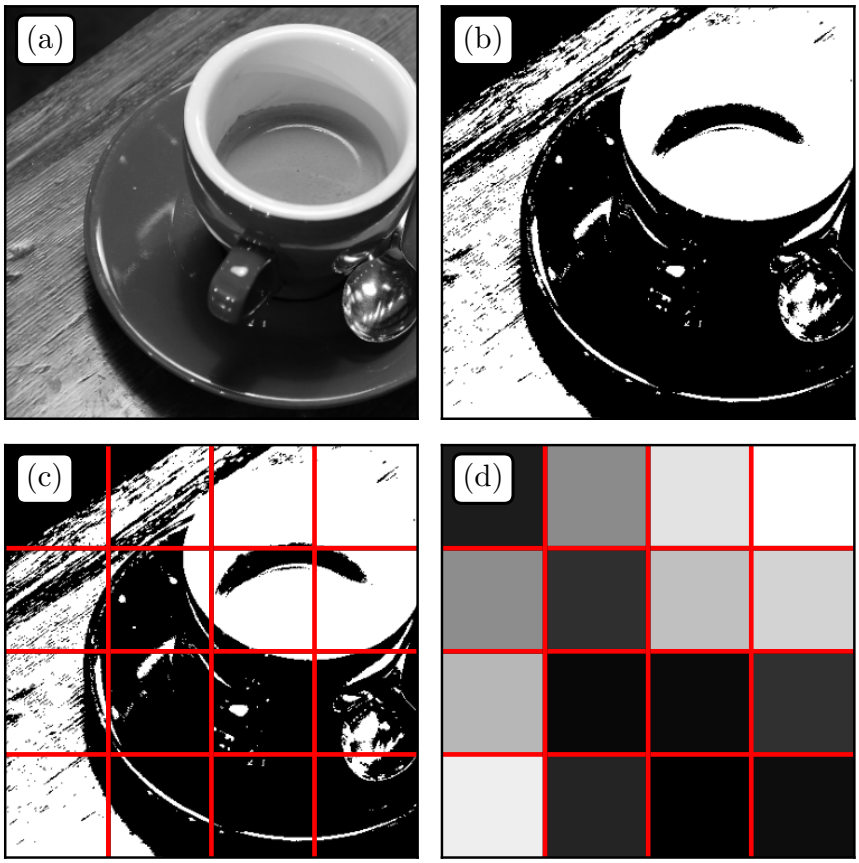

Figure 2.2: Illustration of the segmentation/compression procedure on a classic benchmark image. (a) Original Image. (b) Thresholded image at a given quantile value a. (c) Thresholded image with reduced grid. (d) Reduced sample where each grid cell is replaced by the average pixel color.

the underlying and empirical distributions. Interestingly, the Resolution/Relevance properties are only dependent on the raw sample $\mathcal{S}$ and the compression parameter ℓ, making the overall approach agnostic to the generating process. What is most interesting is thus the way in which the sample evolves with compression, while transitioning from undersampling to oversampling. As a result, one must choose a compression procedure that allows to crossover between these two regimes.

2.2.3 *Application to images*

Images are usually described as fields $h(\boldsymbol{r})$ where $\boldsymbol{r} \in \{1, \dots, N_X\} \times \{1, \dots, N_Y\}$. This is equivalent to a sample made of $\mathcal{S} = \{(\boldsymbol{r}, h(\boldsymbol{r})\}$ of size $N = N_X N_Y$, describing the position and color of each pixel. Naturally, $\mathcal{S}$ lies in the full undersampling regime as each data point is unique.

To compress grayscale images, we therefore propose a simple procedure consisting in two steps: (i) segmentation, and (ii) spatial compression, as illustrated in Fig. 2.2. Segmentation means grayscale levels are transformed into black and white pixels using a threshold level a (fraction of black pixels), leading to the binary image $h_a(\boldsymbol{r})$ (Fig. 2.2(b)). This lowers the amount of possible color states in the sample, a necessary condition to reach the full oversampling regime. Note that one can reconstruct the original image by averaging over all segmentations. This step is generalisable for colors, for example by using a triplet $(a_{\mathrm{R}}, a_{\mathrm{G}}, a_{\mathrm{B}})$ in the RGB space. The second step consists in the compression of pixel positions (Fig. 2.2(c)). One replaces each coordinate $\boldsymbol{r}$ by the index $\boldsymbol{r}^\ell$ of its position on a grid of stepsize ℓ. One ends up with a compressed sample:

$$\mathcal{S}_a^\ell = \{(\boldsymbol{r}^\ell, h_a(\boldsymbol{r}))\}. \tag{2.2}$$

Each pixel value is then replaced by its average in the reduced grid (Fig. 2.2(d)). Finally, $k^\ell_{(\boldsymbol{r}_\ell,0)}$ and $k^\ell_{(\boldsymbol{r}_\ell,255)}$ would be defined as the number of black and white pixels in cell $\boldsymbol{r}^\ell$, and m_k^ℓ as the number of cells with k black or white pixels at scale ℓ. Using Eqs (2.1), one can compute the values of $\hat{H}^\ell[s]$ and $\hat{H}^\ell[k]$ that will be used in the sequel.

One can make a direct analogy between this compression procedure and image processing architectures such as Convolution Neural Networks (CNN) [185]. First, their constitutive layers usually combine a spatial compression procedure, that is a first linear convolution, with a trainable or prescribed layer. Then, a segmentation step is performed using a nonlinear transformation on pixel values called *activation function*. In a similar fashion, our procedure consists in a one layer network, taking $\mathcal{S}$ as input and giving $\mathcal{S}_a^\ell$. Interestingly, we do not need to specify a particular convolution matrix as an input to the algorithm, but only a size parameter, by that making our approach more agnostic. Ultimately, note that any compression procedure allowing the undersampling/oversampling transition could have been selected. For example, one could use Discrete Fourier or Wavelet coefficients, classically used in JPEG compression algorithms [192, 193]. Another approach would consist in using intermediate representations of trained or untrained networks with binary activation functions (perceptron-like) and tunable layer size, as in the Resolution/Relevance trade-offs of deep neural architectures [130].

2.3 RELEVANCE OF $1/f^\alpha$ TEXTURES

In this section we illustrate the use of the metrics ($\hat{H}^\ell[s]$, $\hat{H}^\ell[k]$) on a simple yet widely encountered class of processes: two-dimensional $1/f^\alpha$ random Gaussian fields. We first recall the properties of such fields and then study the influence of α on Resolution and Relevance.

2.3.1 *On $1/f^\alpha$ Gaussian fields*

$1/f^\alpha$ Gaussian fields consist in the linear filtering of an initially uncorrelated 2D white noise (see Appendix. A.1). The latter presents a flat Fourier spectrum that is then multiplied by $1/f^\alpha$, therefore leading to a power spectrum scaling as $1/f^{2\alpha}$. This leads to the forcing of spatial correlations in the direct space. Such power law filter introduces scaling properties that are usually described by the roughness *Hurst* exponent $\mathrm{H} := \alpha - d/2$ where d is the field dimension (here $d = 2$). Depending on the sign of H, one can recover two types of processes. When $\mathrm{H} < 0$ the random field is stationary, that is with fixed mean and correlations $C(\delta r) \propto \delta r^{2\mathrm{H}}$ at lag distance δr. The specific case $\mathrm{H} = -d/2$ corresponds to an unmodified spectrum (white noise). When $\mathrm{H} > 0$, the process is no longer stationary but possesses stationary increments with scaling $\langle [h(\boldsymbol{r} + \delta\boldsymbol{r}) - h(\boldsymbol{r})]^2 \rangle \propto \delta r^{2\mathrm{H}}$. We generate three samples of distinct roughness values $\mathrm{H} \in \{-1/2, 0, 1/2\}$, shown in Fig. 2.3(a), (b) and (c) respectively. The Hurst exponent influences the visual aspect of roughness, with images getting smoother as H increases. Figure 2.3(d) shows the azimuthally averaged power spectrum $S(f) = \langle |\tilde{h}(f, \theta)|^2 \rangle_\theta$ allowing to check that the generating method is robust as the expected scaling behavior and exponents are recovered.

2.3.2 *Multiscale relevance of random textures*

We now perform the segmentation described above on the fields presented in Fig. 2.3. The resulting textures for threshold value $a = 0.5$ are displayed in Fig. 2.4(a)-(c) and the corresponding Resolution/Relevance curves $(\hat{H}^\ell[s], \hat{H}^\ell[k])_{\ell \in \{1,\dots,N\}}$ are plotted in Fig. 2.4(d).

One can see that while the patterns remain quasi-identical for $\mathrm{H} = -0.5$ (Fig. 2.4(a)) and $\mathrm{H} = 0$ (Fig. 2.4(b)), this is not the case for $\mathrm{H} = 0.5$ (Fig. 2.4(c)) where large areas of uniform tint are created by the segmentation procedure. This is due to the presence of stronger spatial correlations, inducing more persistence of patterns and less fluctuations around the average. Further, one can see that the $\mathrm{H} = 0$ texture displays interesting visual features at all scales, as reported in visual quality assessment experiments [1], while they appear limited to small scales for $\mathrm{H} = -0.5$. It is not straightforward to connect these observations with the Relevance curves in Fig. 2.4(d), as the relative Relevance varies with Resolution. It thus seems more natural to consider the Relevance across all levels of compression.

To do so, we introduce a measure that quantifies the overall robustness of a sample to compression called *Multiscale Relevance* (MSR) and defined as:

$$\mathrm{MSR} := \int \hat{H}^\ell[k] d\hat{H}^\ell[s], \tag{2.3}$$

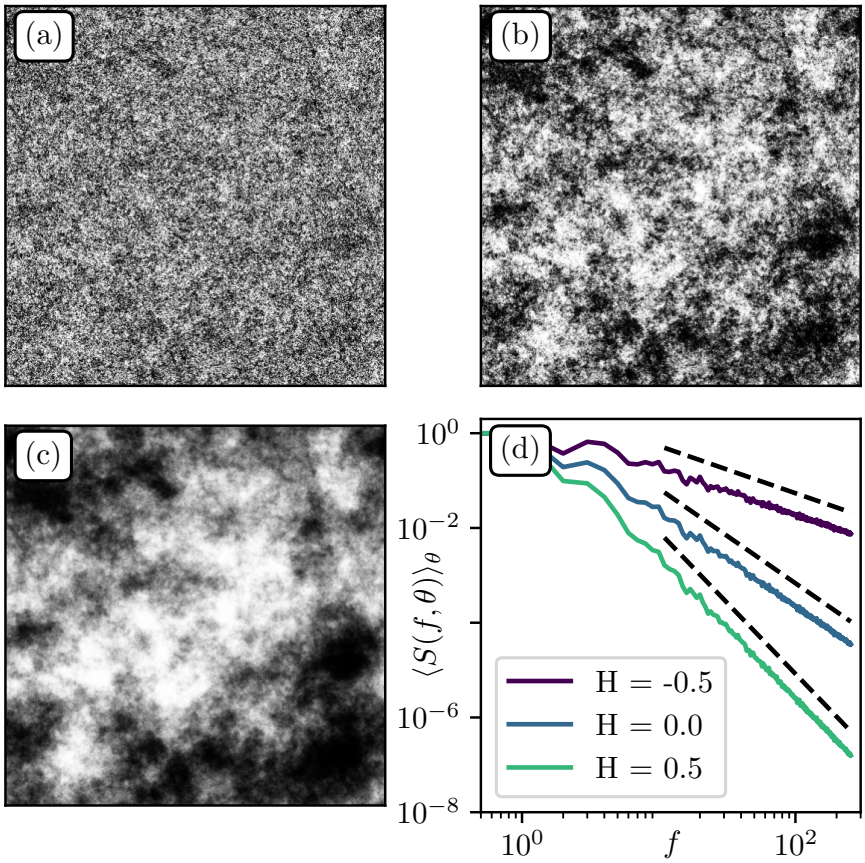

Figure 2.3: $1/f^\alpha$ textures generated from the same white Gaussian noise seed. (a), (b), (c) Representations of $1/f^\alpha$ random fields with respective roughness $\mathrm{H} = -0.5, 0, 0.5$ and spatial resolution 512×512. (d) Azimuthally averaged power spectrum $\langle S(f,\theta)\rangle_\theta$. Black dashed lines indicate the theoretical power spectrum decay $1/f^{2\alpha}$ with $\alpha = 1 + \mathrm{H}$.

which is non other than the area under the Resolution/Relevance curve. This measure was introduced in [20] as an order parameter characterizing neuronal activity time series, and was successful at distinguishing useful information from ambient noise, as expected from a complexity measure [22]. Note that while several measures of complexity based on multi-scale entropy contributions have already been introduced in the literature [21, 196], the MSR differs in that the contribution of each scale is naturally weighted by the Resolution. Other measures generally give identical weights to each compression level. For the images in Fig. 2.4, one obtains $\mathrm{MSR}(\mathrm{H} = 0.5) < \mathrm{MSR}(\mathrm{H} = -0.5) < \mathrm{MSR}(\mathrm{H} = 0)$. This is consistent with our previous visual impression that the texture in Fig. 2.3(b) seems to contain more information at different scales.

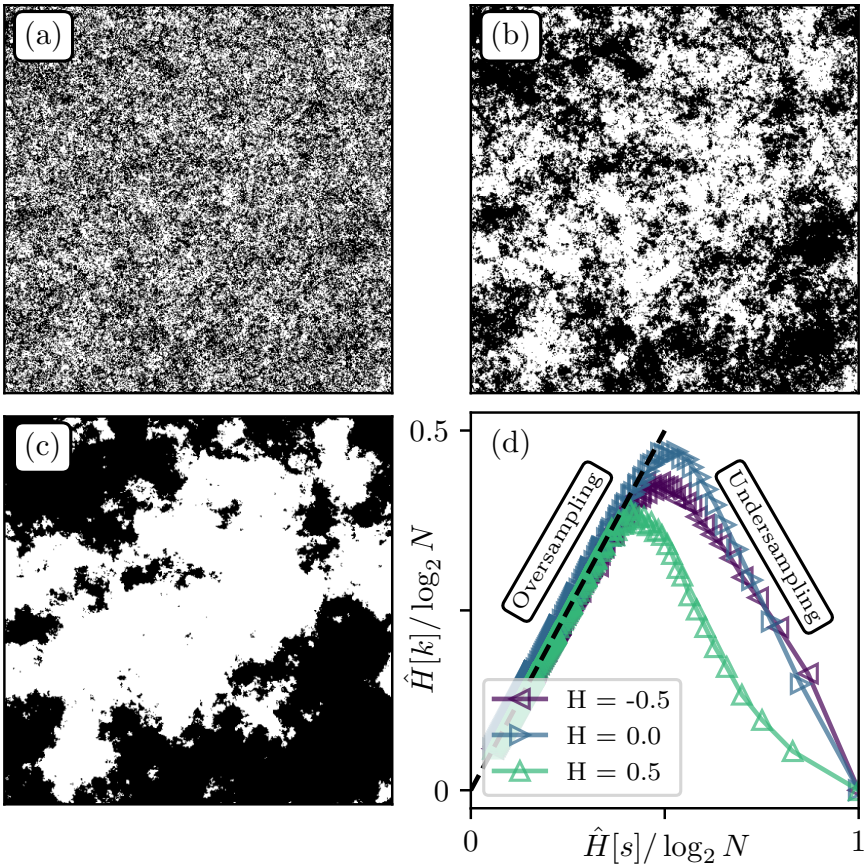

Figure 2.4: (a), (b), (c) Segmented versions of the textures of Fig. 2.3, with $H = -0.5, 0, 0.5$ respectively, and threshold value $a = 0.5$. (d) Resolution/Relevance curves normalized by the maximum entropy $\log_2 N$.

2.3.3 *Most relevant segmentation(s)*

One naturally expects the segmentation threshold a to influence the Relevance. Indeed, at given $H < 0$, most relevant representations do not seem to correspond to $a = 0.5$. This is confirmed in Fig. 2.5(a) where the Relevance curve for $H = -0.8$ is higher for $a = 0.66$ than $a = 0.5$. Figure 2.5(b) displays the MSR as function of a for three values of H. For $H = -0.8$ (dashed curve) one observes two symmetric maxima at $a_c = 0.5 \pm .13$, consistent with Fig. 2.5(a). Interestingly, breaking the symmetry in the distribution of pixels by choosing a "background canvas" leads to more interesting samples in terms of Resolution/Relevance. As one can see in Fig. 2.5(c), there is a bifurcation at $H \approx 0$ below which two maxima of MSR coexist. The obtained values of a_c for $H < -1/2$ fall close to the classic percolation threshold $a^* = 0.59$ on the 2D square lattice [197]. Indeed, our segmented images are equivalent to samples of the correlated percolation site problem. In particular, Prakash *et al.* [24] observed, as we do here, that when

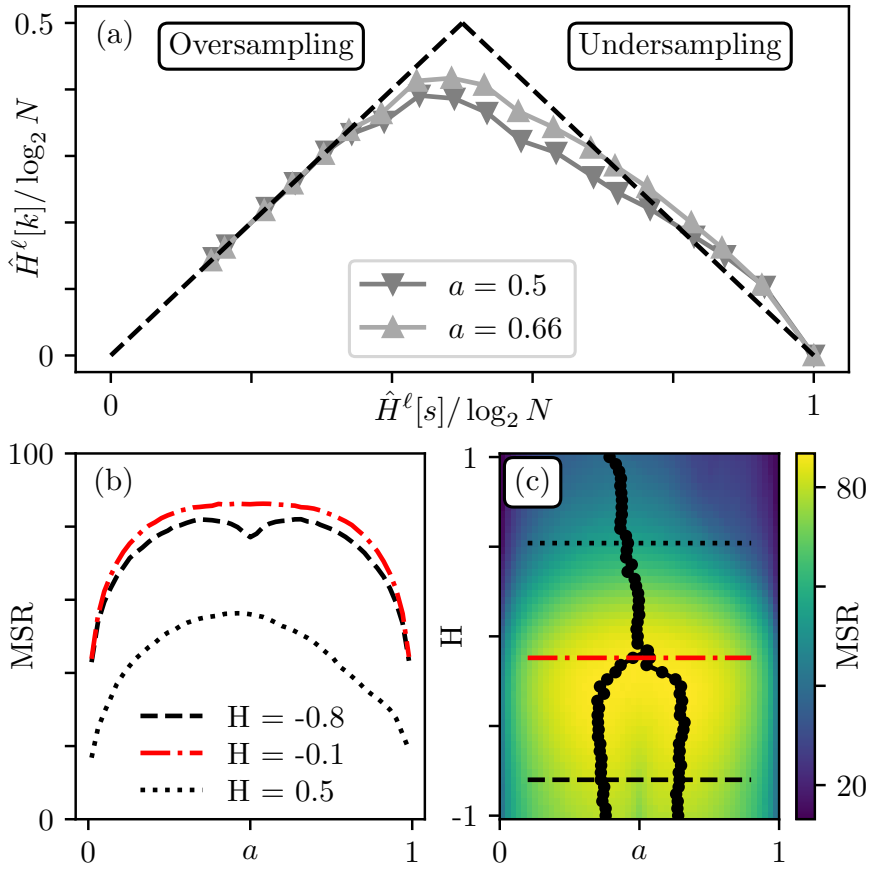

Figure 2.5: Influence of the segmentation value a. (a) Relevance curves for $H = -0.8$ for two values of a. (b) MSR as function of a for $H = -0.8$ (black dashed line), $H = -0.1$ (red dashed dotted line) and $H = 0.5$ (black dotted line). (c) Density plot $MSR(H, a)$. The maxima are signified with black markers.

$H \to 0$ from below both maxima continuously meet at $a_c = 0.5$ while flattening the $MSR(a)$ curve around such value (see Fig. 2.5(b)). At this critical point, the information content of images becomes less sensitive to the segmentation process.

When $H \approx 0$, $MSR(a)$ displays one unique maximum at $a_c = 0.5$. However, as H increases further, so does the range of correlations, leading to finite-size effects. The resulting a_c becomes very noise dependent as different samples lead to different critical thresholds. Interestingly, such behavior was also reported in the percolation of 2D Fractional Brownian Motion [198].

2.4 RELEVANCE OF NATURAL IMAGES

We now focus on *natural images*, namely pictures of natural scenes and landscapes. These have long been studied in the literature [119,

120, 123–126], as they display robust statistical features, such as scale invariance and pattern distribution criticality.

2.4.1 *On the grayscale field*

Figure 2.6(a) shows the photograph from Tkacik *et al.* [199] in the Okavango Delta in Botswana, described as a "[...] *tropical savanna habitat similar to where the human eye is thought to have evolved*". The image is subdivided into fifteen patches of size 512×512 pixels. One can observe a wide variety of patterns, ranging from uniform shades of light gray in the sky to strong discontinuities with tree branches and noisy vegetation textures.

A power spectrum analysis for all patches is shown in Fig. 2.6(b). The shape in the high frequency limit is due to camera calibration,

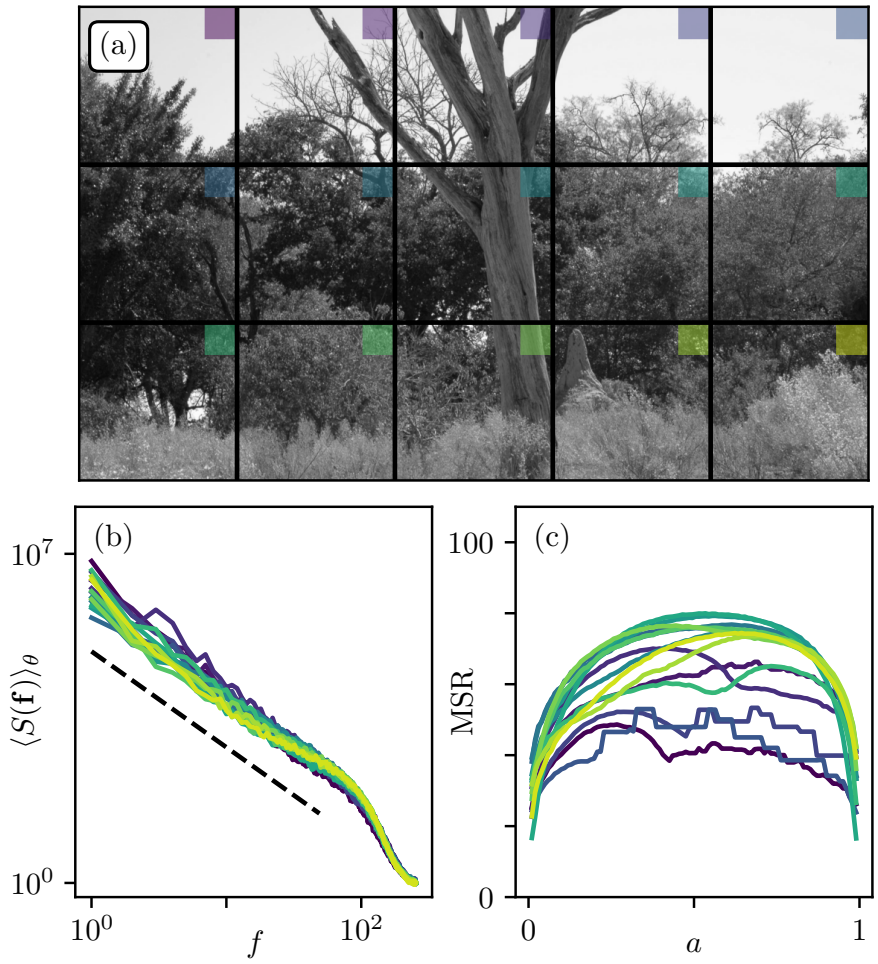

Figure 2.6: (a) Natural grayscale image from [199], segmented in patches of size 512× 512. (b) Power spectrum for each patch. Dotted line is a decaying power law with exponent −2. (c) MSR as function of a for each patch.

optical blurring, or post-processing procedures, which are independent of the patch content. At low frequency we observe a decaying power law with exponent -2.0 ± 0.1. Note that, although there are small fluctuations that may be related to patch features [119], the power spectrum analysis seems rather unable to capture the visual heterogeneity from one patch to another mentioned above.

This being said, $S(f) \sim 1/f^2$ translates to $\mathrm{H} = 0.0 \pm 0.1$ in terms of roughness exponents, which is precisely the range in which the MSR displayed critical and nontrivial behaviour for random textures in Sec. 2.3. We thus expect that the MSR approach may allow for a finer characterization of each patch. Another issue with classical spectral analysis is that the power spectrum of the image is expected to be extremely sensitive to non-linear transformations of its color histogram, even monotonous, that keep the visuals identical. With the MSR method, there is no such issue as the segmentation parameter a defines the proportion of black and white pixels, regardless of the shape of the color histogram.

Figure 2.6(c) shows the MSR curves for all patches. First observation is that the range of MSR values is similar in magnitude to that of $\mathrm{H} \approx 0$ textures in Sec. 2.3. Then, one clearly sees significant differences between the MSRs of each patch. Patches containing mainly bushy textures with no abrupt changes in patterns display a unique maximum in the MSR(a) curve. Note that the singularities that appear in some cases are due to specific colors being disproportionate in the histogram (uniform sky). Patches containing heterogeneous shades, or physical objects of different sizes combining tree truncs, branches and bush (e.g. bottom left in 2.6(a)) tend to display two maxima, similarly to $\mathrm{H} < 0$ (see Sec. 2.3).

Figure 2.7 focuses on the bottom-left patch of Fig. 2.6(a). This subimage seems to display two distinct dominant color levels. Such levels actually correspond to the maxima of the MSR curve in Fig. 2.7(b). This is visually confirmed from the segmentations 2.7(c) and 2.7(d) which capture best the fluctuations at the top and bottom of the image respectively. We emphasize that the latter representations together constitute the most informative segmentations of (a). Superimposing them (Fig. 2.7(e)) indeed leads to a good approximation of the original image with only three color levels {0,127,255}. The MSR method thus seems to account well for the diversity of content of natural images, inaccessible through classical power spectrum analysis.

2.4.2 *On the gradient magnitude*

To understand further the architecture of natural images, we now focus on the gradient magnitude field intended to capture strong spatial irregularities such as contours or borders. In addition, taking the gradient has the advantage of stationarizing the initial field. The

gradient analysis is a fundamental block of various image processing procedures, from classic edge detection [200], to supervised [201] or unsupervised [185] classification architectures in machine learning. From a more perception-based psychophysical perspective, it has been shown that essential information such as orientations, geometries and

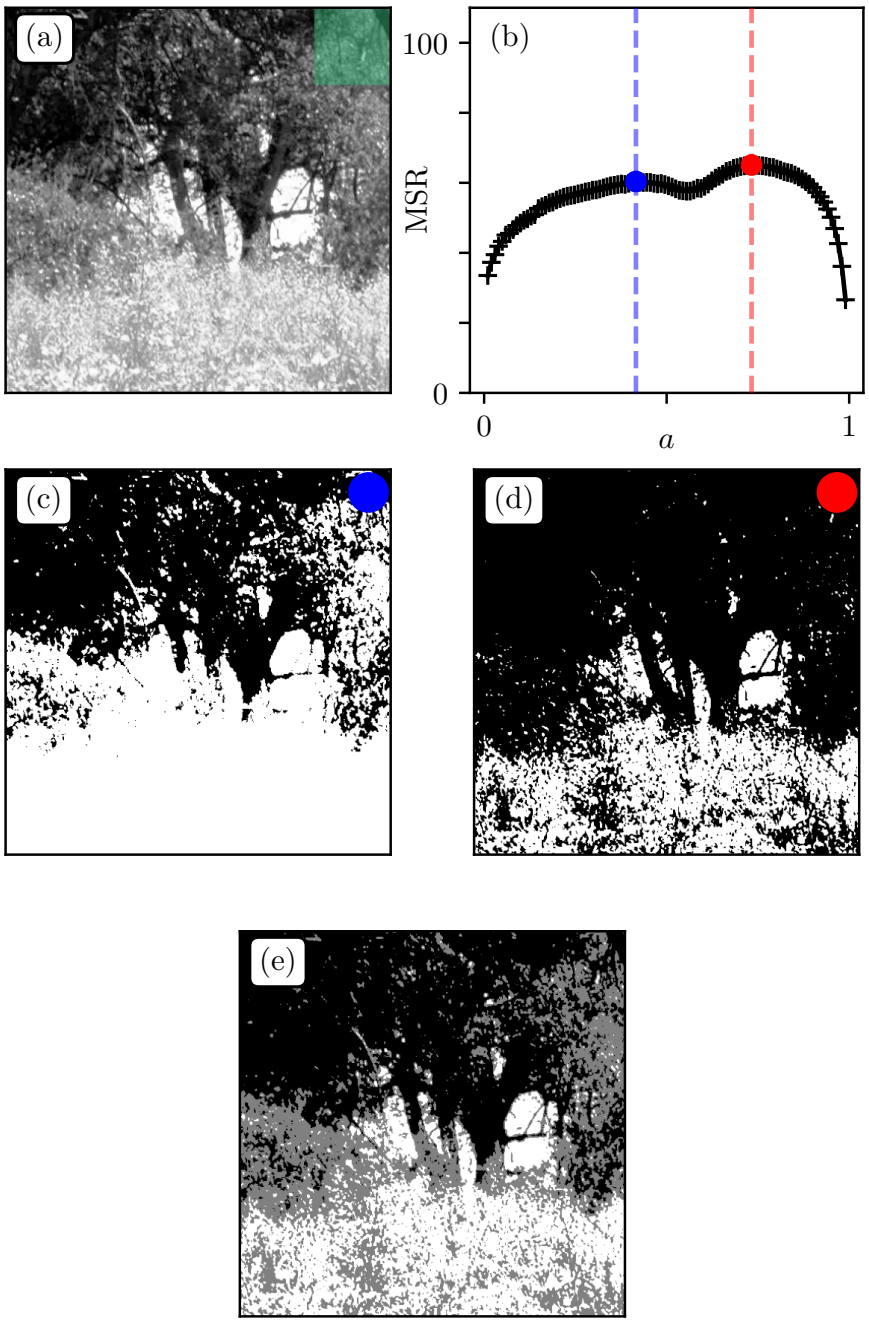

Figure 2.7: (a) Bottom-left patch of Fig. 2.6(a). (b) MSR as function of a with highlighted critical thresholds $(a_1, a_2) = (0.42, 0.73)$. (c)(d) Corresponding segmented patches. (e) Image obtained by adding (c) and (d), with three color levels {0,127,255}.

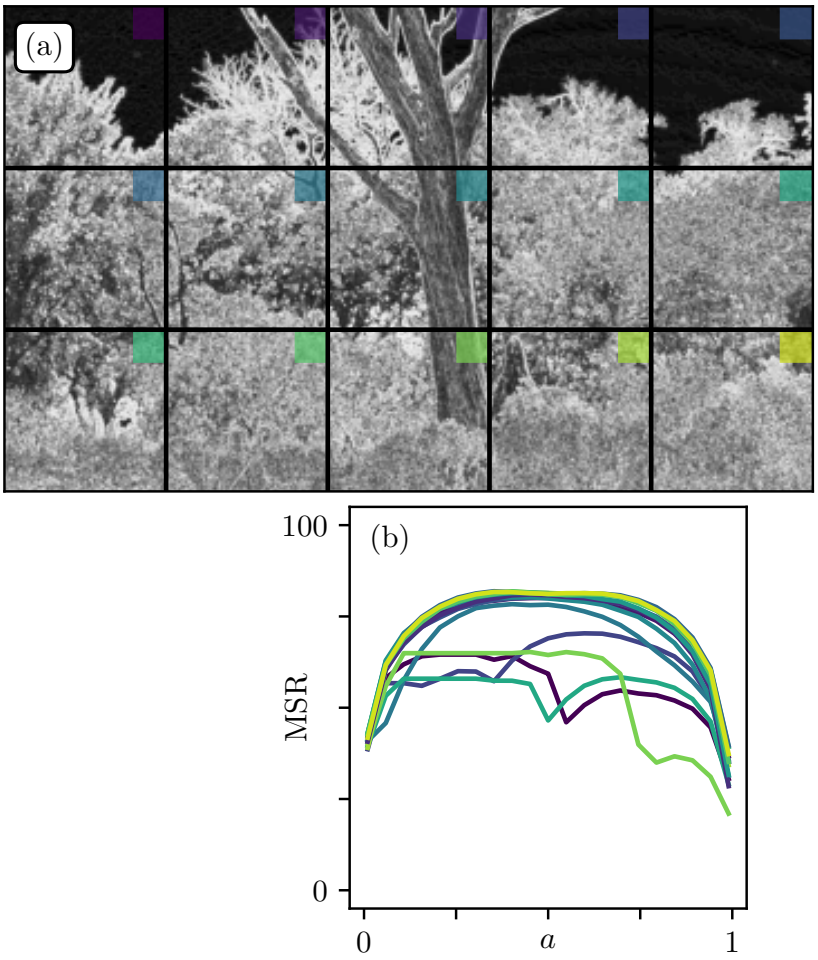

Figure 2.8: (a) Gradient Magnitude field of Fig. 2.6(a), with $j = 0$, divided in 512×512 patches. (b) MSR as function of a for the different patches.

positions could be directly inferred from the visual assessment of the gradient field [202–204]. We compute the gradients $|\nabla h|$ from wavelet convolutions. This method is now extensively used as shows excellent robustness for signal processing tasks [205–209]. On has:

$$|\nabla h| = |h * \boldsymbol{\psi}_j(\boldsymbol{r})|^2, \tag{2.4}$$

where $\boldsymbol{\psi}_j := (\psi_{j,x}, \psi_{j,y})$ is a wavelet gradient filter of characteristic dyadic size 2^j. This wavelet consists in mixing gradient and Gaussian windows, the latter being of standard deviation $\sigma_j = 2^j$ pixels. The procedure with $j = 0$ yields the image in Fig. 2.8(a). As expected, one obtains a strong signal (bright shades) for fluctuating textures of vegetation or sharp contours like branches, and low values (dark shades) for smooth and uniform regions like the sky.

We then conduct the MSR analysis on these new patches (Fig. 2.8(b)), and observe that most patches give flat MSR curves. This is tantamount to the critical H ≈ 0 case with logarithmic correlations described in

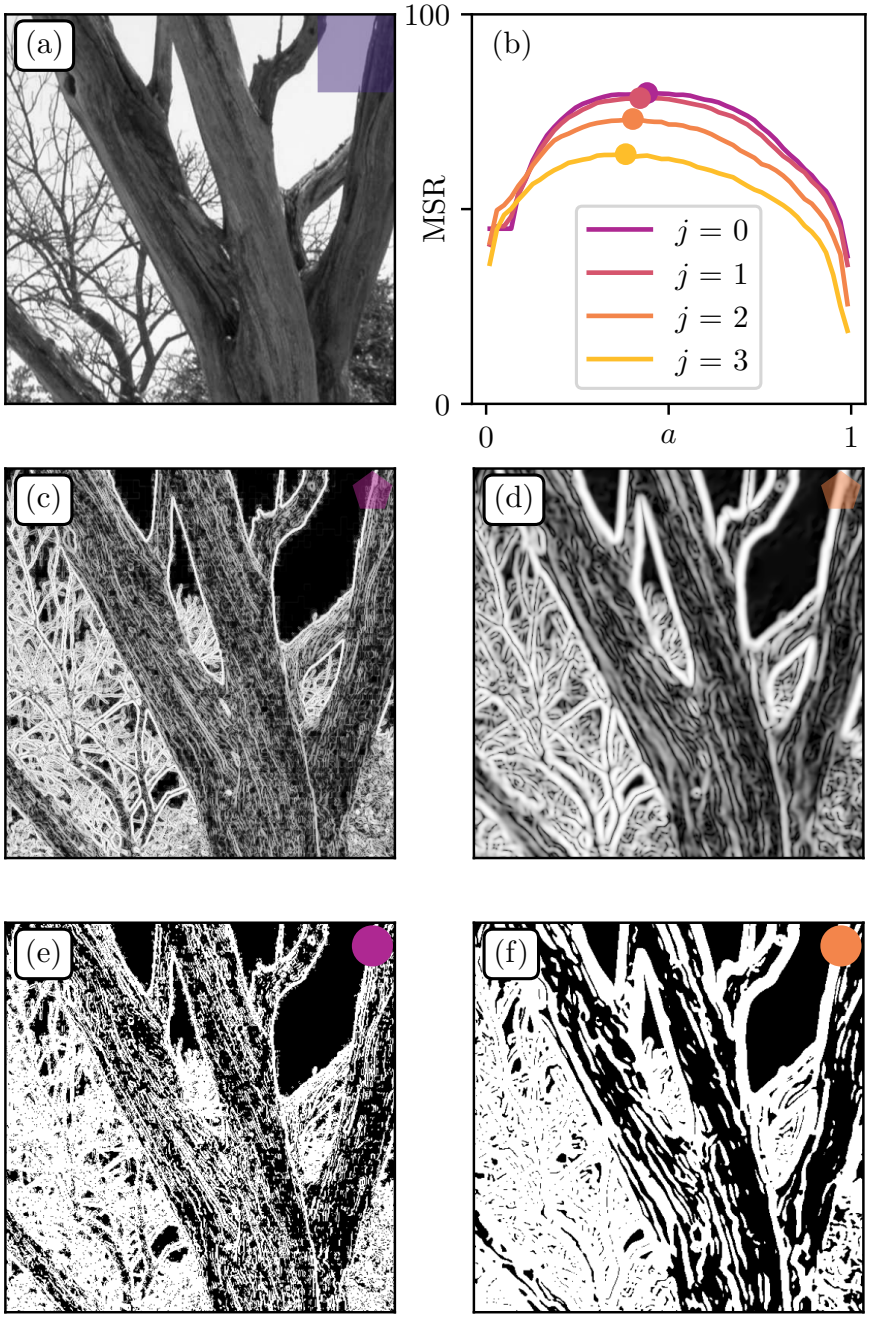

Figure 2.9: Influence of the Gradient Wavelet size. (a) Original patch from Fig. 2.6(a). (b) MSR as function of a for gradient wavelets of dyadic size $(2^j), j \in \{0, 1, 2, 3\}$. (c)(d) Gradient magnitudes for $j = 0$ and $j = 2$ respectively. (e)(f) Segmented gradient magnitudes at critical threshold values a_c for $j = 0$ and $j = 2$ respectively.

Sec. 2.3 (see Fig. 2.5). One may indeed think of natural images as a patchwork of objects of various sizes; such superposition of patterns is reminiscent of additive cascades processes [210] that also display logarithmic correlations.

We now explore the effect of changing the wavelet size (see Fig. 2.9). We chose the top middle patch in Fig. 2.8(a) as it contains large objects and small scale details. As one can see in Figs. 2.9(c) and (d), increasing j has the effect of coarse-graining small fluctuations to only leave larger ones. This translates into smaller Relevance at low compression, which in turn reduces the overall MSR (Fig. 2.9(b)). Finally, the segmented gradient fields at critical threshold values (Figs. 2.9(e) and (f)) remain visually close to initial fields (Figs. 2.9(c) and (d)). This is indeed expected as gradient magnitudes already show a large proportion of black and white pixels at the contours of physical objects.

2.5 DENOISING WITH RUDIN-OSHER-FATEMI ALGORITHM

Here we illustrate the potential of MSR in the context of a common digital image processing task: image denoising

Such procedure consists in correcting unwanted noise caused by signal processing or camera artefacts. To tackle this problem, a classic algorithm is the Rudin-Osher-Fatemi (ROF) [86] which minimizes the following functional:

$$\mathcal{L}[f] = \lambda \|\nabla f\|_2^2 + \|h - f\|_2^2 , \tag{2.5}$$

where h is the original noisy image, f the target denoised image and λ a *regularization/penalty* term preventing gradient explosion and allowing for smooth solutions. The free parameter λ is generally chosen by the operator through visual assessment.

Here we propose to calibrate such a model using classic signal processing metrics, namely the Peak Signal-to-Noise Ratio (PSNR) [194] and the Structural Similarity Index (SSI) [195]. PSNR is directly related to the Mean Squared Error (MSE) between original and mapped images through $\mathrm{PSNR} = 10 \log_{10} \left(\Delta^2 / \mathrm{MSE}\right)$ where Δ is the range of the signal, that is 255 for typical grayscale encoding. SSI is based on the comparison of patches between two images and takes into account properties such as luminance and contrast. Both are widely used in the digital image processing community. We also compute the Multiscale Relevance over the gradient magnitude field MSR_∇ as we expect the denoised image to display the same properties as natural images. This last measure does not have a priori, and can hence be used to calibrate the algorithm.

We consider the image in Fig. 2.10(a) obtained by adding a Gaussian white noise to the patch in Fig. 2.6(a). We intentionally choose a high noise value to make the denoising procedure difficult, such that some details from the original image may never be recovered. Our goal is to

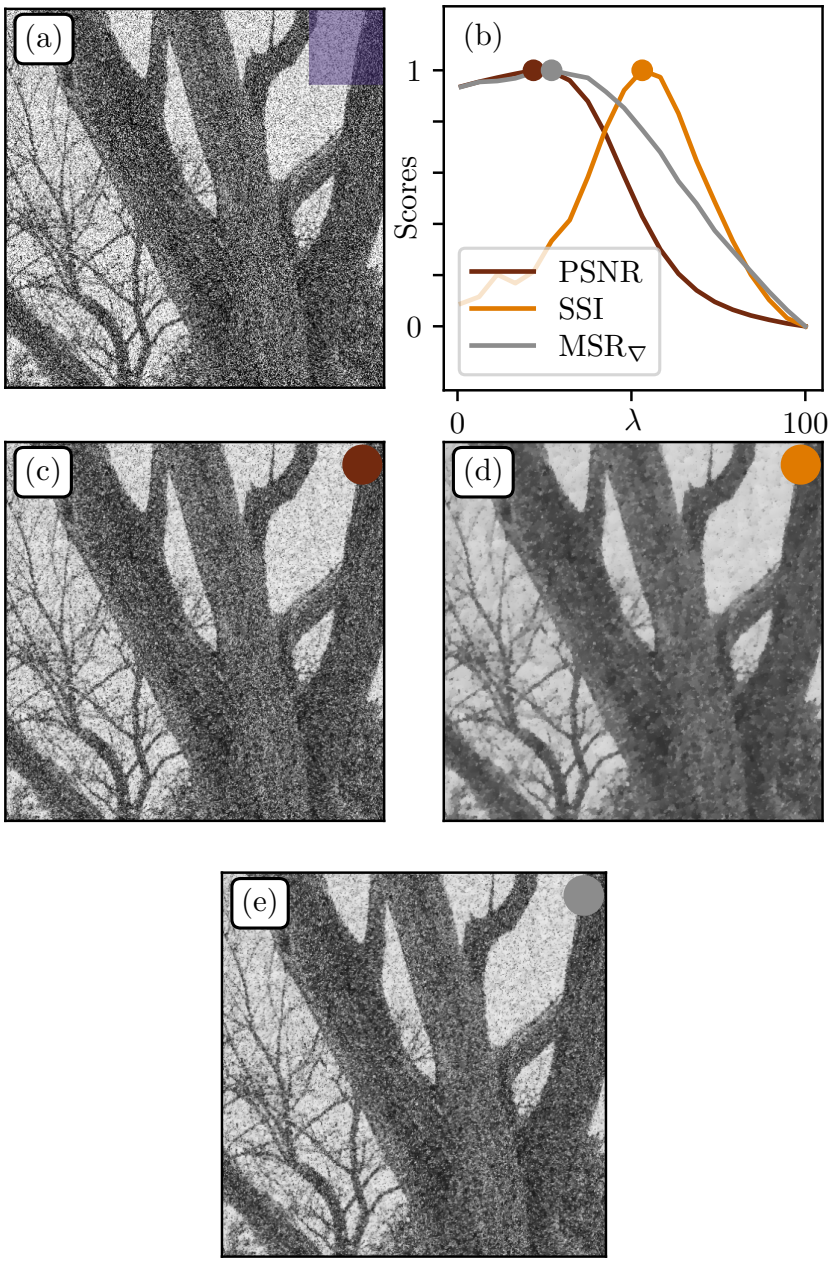

Figure 2.10: Denoising. (a) Noisy patch obtained from adding a Gaussian noise ($\sigma = 100$) to the same patch from Fig. 3.4(a). Rescaled scores as function of λ for different performance measures: Peak Signal-to-Noise Ratio (PSNR), Structural Similarity Index (SSI) and MSR over the gradient field MSR_∇. (c),(d), (e) Denoising at optimal regularization parameter λ^* for PSNR, SSI and MSR_∇ respectively.

seek the optimal λ^* leading to the best visual. The scores obtained for each method as function of λ are displayed in Fig. 2.10(b). Optimally denoised images using PSNR, SSI and MSR_∇ are shown in Fig. 2.10(c),

(d) and (e) respectively. With PSNR, one is left with a rather high level of noise, while details on the trunk surface or in the branches are conserved. In contrast, SSI removes a significant part of the noise, but at the cost of blurring small scale details. Although less obvious than for the color mapping procedure, optimal denoising with MSR_∇ seems like a good compromise between a too noisy PSNR image and an overly smoothed SSI image.

2.6 CONCLUSION

Let us summarize what we have achieved. We first introduced the Resolution/Relevance framework through a simple illustrative example. We showed how such formalism can be applied to image analysis. With the aim of investigating the framework in a controlled environment, we started by studying random textures. We then defined the Multiscale Relevance (MSR) which measures the entropy contribution at all compression scales, and obtained statistical features reminiscent of the correlated percolation problem. In particular, we highlighted the existence of a critical roughness parameter $H_c \approx 0$, corresponding to logarithmic correlations, and discussed optimal segmentation. We then extended the analysis to natural images and drew a successful comparison with random textures; we observed strong similarities with critical random Gaussian fields. Looking at gradient magnitude fields revealed an even stronger similarity to roughness criticality. Finally, we confronted the MSR procedure to a classical signal processing measure in the context of a simple image processing task: denoising. We obtained first interesting results that highlights the potential of the agnostic MSR approach in the context of image processing. This applicability is further illustrated in Ch. 3, in the case of the classic *color mapping* problem.

Future research should also focus on analytically tractable developments of Relevance and Resolution in simple cases, e.g. Gaussian white noise with well chosen cascading processes. Also note that we considered a straightforward compression procedure on the direct space but equivalent representations, for example Discrete Cosine [192] or Wavelet harmonics [193], could be used to define the reduced sample $\mathcal{S}$. Finally, we have seen that the MSR is able to capture the most relevant segmentation values, which may be used as a pre-processing method for learning frameworks.

2.7 TAKE-HOME MESSAGE

Natural images display robust statistical properties.

We adapt a recent formalism, intended to describe high-dimensional data samples, to image analysis.

- Resolution $\hat{H}[s]$ and Relevance $\hat{H}[k]$ respectively measure the entropy of the sample and of its frequencies.
- The area under the Resolution/Relevance curve is called the multiscale relevance (MSR), and measures information robustness over all compression scales.

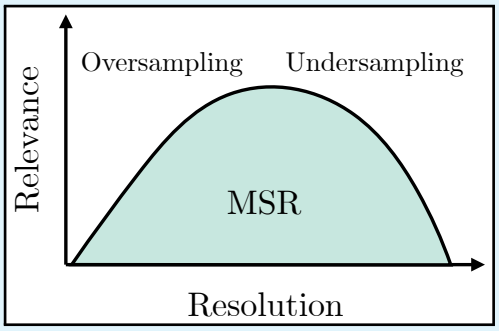

We find that:

- Gaussian $1/f^{\alpha}$ textures display percolative behaviour, with maximal MSR values around $\mathrm{H} = \alpha - 1 = 0$.
- Natural images fluctuate around $\mathrm{H} = 0$, while displaying features informing on specific image content.
- Gradient magnitudes, signifying contours of objects, further condensate around $\mathrm{H} = 0$.

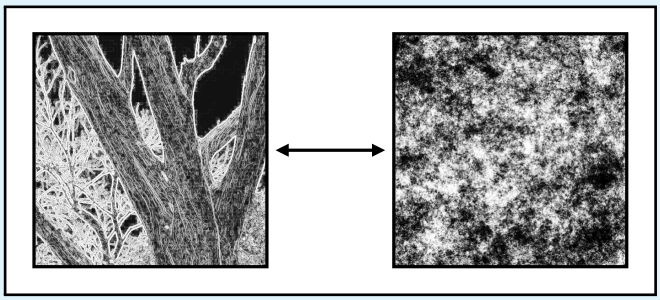

Enforcing high/robust MSR properties may be an interesting performance metric for image processing algorithms.

3

APPLICATION TO IMAGE PROCESSING: COLOR MAPPING

Think of color, pitch, loudness, heaviness, and hotness. Each is the topic of a branch of physics.

— Benoit (.B [211]) Mandelbrot

This chapter is a reorganization of [2], written in collaboration with Alexandre Darmon and Michael Benzaquen, and the results of which are based on my doctoral works. Some minor rearrangements were made, to ensure consistency with Chapter. 2.

3.1 INTRODUCTION

In physics, many problems can be formulated in terms of energy minimization. However, for complex systems with a large number of degrees of freedom, analytical minimizers are often difficult to find, and the ground state is seldom representative of the true physical state of the system at hand. To overcome such issues, a classical method in statistical thermodynamics is to slightly relax the energy minimization constraint and introduce a probabilistic model relying on entropy maximization [212, 213]. Such an approach has allowed for the exploration of suboptimal solutions with thermal noise and led to the emergence of historical results on phase transitions, e.g. for Ising models [11, 214]. This method has since been popularized in various fields, for example in biology for inference problems [76] or in computer science for classifiers (see e.g. the softmax function [74]) and annealing procedures [71].

Let us now consider the problem of field quantization and its application for images, that is color quantization. It consists in choosing a set of authorized states called the color palette and then projecting each pixel of the original image onto this palette. This method is naturally very relevant for compression and other problems involving digital image processing. The first step consists in finding the most convenient color palette from the original histogram using thresholding levels [133, 134] or clustering methods [135–138]. The second step, called *pixel mapping*, is usually achieved by performing a simple nearest color procedure. Stochastic mapping – or *dithering procedures* – are also used to reduce threshold artifacts and improve the overall visual quality of the quantized image [140–142].

Here, we shall focus on the pixel mapping step by constraining the color palette *a priori*. The aim of the present chapter is to use seasoned

statistical physics tools and novel information theory methods introduced in Ch. 2 to tackle the color quantization problem. We adopt a field theory approach, based on the exploration of simple observables at and around optimality using thermal noise. In Section 3.2 we provide a method to explore new solutions to the quantization problem with a Maximum Entropy based approach. In Section 3.3.1 we show that, in the specific case of color quantization and with the simplest error measure, this method yields surprisingly good visuals when varying the temperature of the system. To quantify this observation, and inspired by [142], we use the convoluted error to look for optimal thermal noise levels regarding the overall image quality. In Section 3.3.2 we confront the results for images with different structural characteristics, and show that the optimal temperatures are a good proxy for image complexity. In Section 3.4, guided by [142], we implement a Monte Carlo algorithm to directly minimize the convoluted error. From the tools introduced in Ch. 2, we determine in Sec. 3.5 a method to calibrate the temperature and convolution parameters. Finally, in Section 3.6 we illustrate how the method can be extended to other types of images, different target color palettes and alternative convolution kernels.

3.2 STATE QUANTIZATION

We consider a field $h(\boldsymbol{r}) \subset F$ and want to build its optimal quantized version $\hat{h}(\boldsymbol{r}) \subset \hat{F}$ where $\hat{F}$ is a subset of F. To do so, one usually minimizes a loss function between $\hat{h}$ and h. A first natural choice for the loss function is a site-wise measure of the quantization error $\mathcal{L}(h,\hat{h}) = \sum_{\boldsymbol{r}} \mathcal{L}_F(h(\boldsymbol{r}),\hat{h}(\boldsymbol{r}))$ where $\mathcal{L}_F$ is the loss for each site, usually Euclidean or logical. With such a definition, the field $\hat{h}^*$ minimizing $\mathcal{L}(h,\hat{h})$ is simply obtained by replacing each original data with the closest state in $\hat{F}$. Note that this is what commonly happens during the sampling of a continuous signal with an instrument, such as a camera projecting colors in the RGB space [215]. There are cases where this simple quantization process leads to unsatisfying $\hat{h}^*$ fields deviating too much from the original data. For example, quantizing a continuous white noise on a grid with a threshold level artificially generates correlated samples of the site percolation problem [216–218].

To engineer more relevant loss measures, our idea is to explore suboptimal configurations around $\hat{h}^*$ using the Maximum Entropy approach mentioned above [212]. This allows one to define the most agnostic – that is the most entropic – classes of distributions with given constraints, such as normalization. In the context of state quantization we look for the distributions $(\mathcal{P})$ over quantized fields that maximize the following functional:

$$J(\mathcal{P}) = S(\mathcal{P}) - \mu[\sum_{\hat{h}} \mathcal{P}(\hat{h}) - 1] - \lambda \sum_{\hat{h}} \mathcal{P}(\hat{h}) \left[\mathcal{L}(h,\hat{h}) - \mathcal{L}(h,\hat{h}^*)\right], \tag{3.1}$$

where the first term $S(\mathcal{P}) = -\sum_{\hat{h}} \mathcal{P}(\hat{h}) \log \mathcal{P}(\hat{h})$ is the distribution entropy, the second term is the normalization constraint, the last one a constraint on quantization error, and μ and λ their respective Lagrange multipliers. Differentiating Eq. (3.1) with respect to $\mathcal{P}(\hat{h})$ and μ allows to enforce normalization while leaving λ as a free parameter. This leads to:

$$\mathcal{P}_{h,\lambda}(\hat{h}) = \frac{1}{Z_{h,\lambda}} e^{-\lambda \mathcal{L}(h,\hat{h})}, \tag{3.2}$$

where $Z_{h,\lambda}$ is the partition function. By setting $T := 1/\lambda$, we recover a Boltzmann-like distribution where the loss function plays the role of the energy. In extreme cases such as $T \to 0$ and $T \to +\infty$, we respectively recover the Dirac delta distribution centred on $\hat{h}^*$ and the uniform distribution. As in the study of any Hamiltonian system, increasing the temperature softens the energy minimization constraint and is therefore the opportunity to test other basic observables.

3.3 FIRST APPROACH ON MAPPING

3.3.1 *Pixel mapping*

We now apply the above formalism in the classical image processing problem of grayscale quantization. The goal is to reduce the amount of shades taken by the pixels in an image, usually described with 256 levels. In this context, h and $\hat{h}$ respectively correspond to the original and reduced images, while F and $\hat{F}$ respectively correspond to the initial and quantized sets of grayscale levels. To define the loss function we use the naive Squared Error, obtained from squaring the Euclidean distance:

$$\mathcal{L}(h,\hat{h}) = \|h - \hat{h}\|_2^2 = \sum_{\boldsymbol{r}} \left[h(\boldsymbol{r}) - \hat{h}(\boldsymbol{r})\right]^2. \tag{3.3}$$

This loss function being pixel-wise separable, so is the corresponding distribution (Eq. (3.2)):

$$\mathcal{P}_{h,T}(\hat{h}) = \prod_{\boldsymbol{r}} p_{h(\boldsymbol{r}),T}(\hat{h}(\boldsymbol{r})) = \prod_{\boldsymbol{r}} \frac{1}{z_{h(\boldsymbol{r}),T}} e^{-[h(\boldsymbol{r})-\hat{h}(\boldsymbol{r})]^2/T}, \tag{3.4}$$

where $z_{h(\boldsymbol{r}),T}$ is the partition function of the marginal distribution $p_{h(\boldsymbol{r}),T}$.

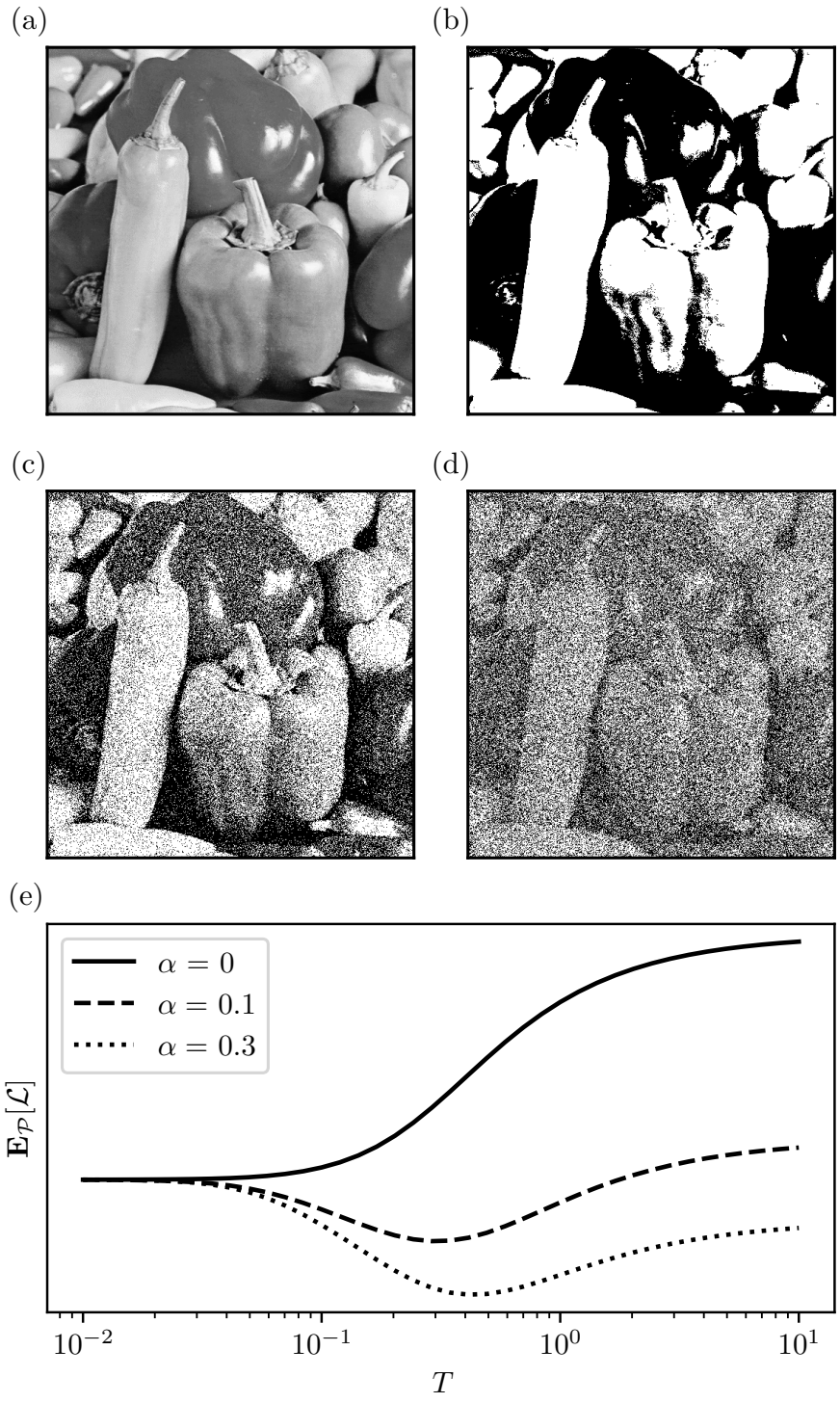

Figure 3.1: Influence of thermal noise on color quantization. (a) Original benchmark image. (b-d) Quantized versions of the original image generated at low ($T \simeq 0$), intermediate ($T = 0.3$) & high ($T = 1$) temperatures using Eq. (3.4). (e) Evolution of the rescaled Mean Convoluted Squared Error between the original and quantized images (Eq. (3.5)) with temperature for different values of the convolution parameter α (Eq. (3.6)).

To test our method, we use a classical benchmark image taken from the USC-SIPI database [219], shown in Fig. 3.1(a), and we sample quantized versions by using the marginal distributions defined in Eq. (3.4). The authorized colors are chosen as black and white, meaning that $\hat{F} = \{0, 255\}$. Figure 3.1(b) was generated at $T \to 0$, equivalent to the naive minimization $\hat{h}^*$ presented in Sec. 3.2, where any texture in the $[0, 127]$ or $[128, 255]$ intervals is simply replaced by black or white pixels respectively. The image, although still recognizable, displays thresholding artifacts such as contouring effects for shaded textures and suppresses a vast amount of details. In Fig. 3.1(c), we introduce thermal noise with intermediate temperature $T = 0.3$, leading to a more interesting visual. Parts of the lighter and darker shades are reconstructed and other details like contours now accurately correspond to the real physical features of the objects, and no longer to fluctuations around the threshold value. In Fig. 3.1(d), one can see that a higher thermal noise level no longer represents a positive contribution, as one excessively randomizes the pixel attribution rule.

Figure 3.1(c) thus interestingly appears to be a better quantized version than Fig. 3.1(b)&(d), especially when looking at it from a distance. Precisely, taking a step back has the effect of coarse-graining/convoluting the image and erasing the small-scale fluctuations created by thermal noise. To quantify such an observation, we define the Convoluted Squared Error $\mathcal{L}_\theta$ comparing the original and quantized fields after a convolution through a given kernel θ:

$$\mathcal{L}_\theta(h, \hat{h}) = \|(h - \hat{h}) \circledast \theta\|_2^2. \tag{3.5}$$

Among the many classes of kernels commonly used in image processing, we choose a power-law kernel of the form $\theta_\gamma(\boldsymbol{r}) \propto \|\boldsymbol{r}\|^{-\gamma}$, for the sake of physical interpretability and mathematical tractability. Its Fourier transform is also a power-law:

$$\tilde{\theta}_\alpha(\boldsymbol{k}) \propto \|\boldsymbol{k}\|^{-\alpha}, \tag{3.6}$$

with $\alpha = d/2 - \gamma$, where $d = 2$ is the space dimension.

When $\alpha = 0$, the kernel in the direct space is narrow and leaves the image invariant. As α increases, the convolution operation replaces each pixel value with its local average of the field. Figure 3.1(e) displays the Mean Convoluted Squared Error $\mathbb{E}_{\mathcal{P}_{h,T}}[\mathcal{L}_\theta]$ as a function of temperature (see Appendix B.1 for the details of the computation of $\mathbb{E}_{\mathcal{P}_{h,T}}[\mathcal{L}_\theta]$). As expected, the unconvoluted Squared Error ($\alpha = 0$, solid line) increases monotonously with T. For higher values of α, however, a local minimum appears at a finite temperature $T^\star_\alpha$. Note that Fig. 3.1(c) was generated with a noise level T close to the minima displayed in Fig. 3.1(e), thereby confirming that the Mean Convoluted Squared Error is a relevant observable for the color quantization problem.

3.3.2 *Visual complexity and optimal temperature.*

The optimal temperature $T_\alpha^\star$ naturally depends on the color histogram of the original image, but also on the spatial arrangement of its pixels. To quantify this last statement, we compare our benchmark image with its transformation through a histogram-invariant operation. We use a shuffling procedure that randomly selects two pixels and switches their position. The procedure is then repeated until the number of switching operations is equal to the number of pixels in the image, that is 512^2. In Figs. 3.2(a1) and (a2), we respectively display the original image and its shuffled version, and we plot the temperatures $T_\alpha^\star$ as function of α in Fig. 3.2(a3). Note that the shuffled image is still recognizable as some pixels are never selected by the procedure. For low values of α, the kernel is too narrow and the convolution has almost no effect, unsurprisingly leading to $T_\alpha^\star = 0$ for both images. Then, both temperatures monotonously increase with α until they meet at a plateau where the evolution is independent of the spatial distribution of pixels. Interestingly, we observe that $T_\alpha^\star$ is systematically higher for the original image, meaning that the shuffling procedure has strongly affected its structural properties. Indeed, natural images such as the peppers present intelligible patterns and strong spatial regularities, far from the random and uncorrelated rearrangement that the shuffling procedure creates. This behaviour is somehow reminiscent of several classical physical systems such as the Random Field Ising Model (RFIM) for which irregularities lower the critical temperature [220, 221] (see Appendix B.2 for more details on the link between the Convoluted Squared Error and the RFIM Hamiltonian).

In Fig. 3.2(b), we test another approach by comparing the evolution of $T_\alpha^\star$ with α for two different benchmark images, each presenting interesting visual features at different scales. Figure 3.2(b1) presents less small scale features than Fig. 3.2(b2), resulting in a higher optimal temperature for low values of α, see Fig. 3.2(b3) (the inset shows the difference of temperatures $\Delta T_\alpha^\star$ between the two images). This tendency reverses at higher scales. Using this procedure we compared a number of other types of natural images (forests, fields, buildings, landscapes), as well as classes of simple abstract textures like those presented in [1], with the same conclusions. This supports the intuition that the temperatures $T_\alpha^\star$ may be used as measures of multi-scale visual complexities and as such, consistent input features for aesthetic assessment algorithms [92, 106, 222–224].

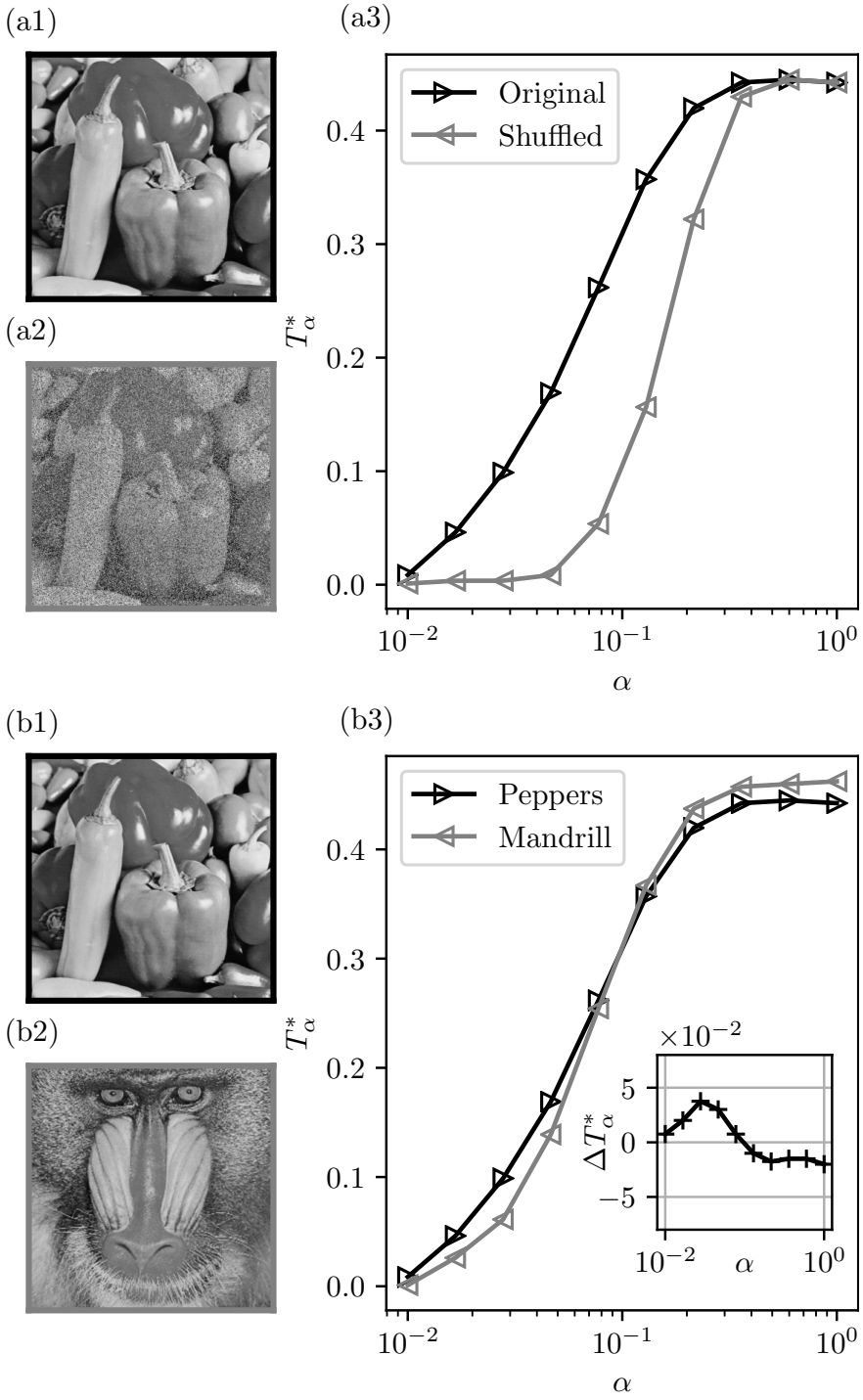

Figure 3.2: Evolution of the optimal temperature $T^\star_\alpha$ with the convolution parameter α for different images. (a) Comparison between the original image and a shuffled version generated with a randomizing procedure. (b) Comparison between two benchmark images (Peppers & Mandrill) displaying structural features at different scales.

3.4 MONTE-CARLO IMAGE GENERATION

As argued above, the Convoluted Squared Error $\mathcal{L}_\theta$ in Eq. (3.5) is a highly relevant observable for the color quantization problem. As such, it seems reasonable to use it as our effective energy function. An idea, see e.g. [142], is to directly generate images minimizing this error function using a Monte Carlo algorithm. This algorithmic approach is necessary as there is no explicit minimum of $\mathcal{L}_\theta(h, \cdot)$. Let us stress that, while Monte Carlo approaches and other dithering methods have historically contributed to the image quantization problem, the last two decades were marked by more evolved developments, using adaptive kernels [225] and clustering algorithms [226, 227]. Here, for the sake of physical interpretation, we focus our attention on the classic Monte Carlo approach as it contains the minimal ingredients to tackle this problem.

Here we implement a simplified Monte Carlo algorithm where we use the power-law kernel defined in Eq. (3.6) (rather than the Gaussian window with simulated annealing procedures used in [142]).

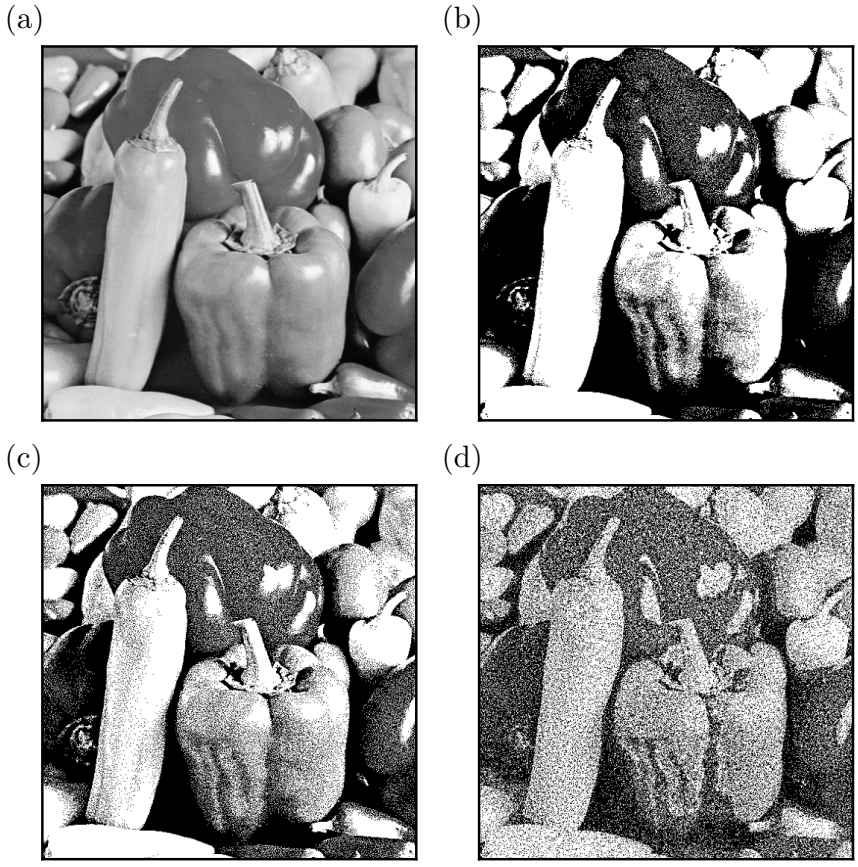

Figure 3.3: Monte Carlo image generation. (a) Original benchmark image. (b-d) Monte Carlo simulations for $\alpha = 0.02$, $\alpha = 0.05$, $\alpha = 0.5$ respectively. Images were initialized with $\hat{h}^*$ and the simulation ran until the loss function reached stability.

Images were initialized with the solution $\hat{h}^*$, and the algorithm ran until convergence of the loss functions. For algorithmic efficiency, we use the Parsival equality on Eq. (3.5) to obtain $\mathcal{L}_\theta(h, \hat{h}) = \|\mathcal{F}[h - \hat{h}](\boldsymbol{k}) \cdot k^{-2\alpha}\|_2^2$, with $\mathcal{F}$ the Fourier transform calculated using the FFT algorithm (thereby assuming periodic boundary conditions). Figure 3.3(a) displays again the original image for reference, and Figs. 3.3(b-d) the images corresponding respectively to $\alpha = 0.02$, $\alpha = 0.05$, $\alpha = 0.5$. For Fig. 3.3(b), the kernel function is narrow: small-scale details like the shadows on the peppers are faithfully reproduced, while leaving large areas of uniform color. Increasing α helps removing the latter artefact and improves the overall visual impression when looked at from a distance, see Fig. 3.3(c). However, too large convolution windows yield images lacking small-scale accuracy, see Fig. 3.3(d). A compromise shall thus be found in order to generate the most faithful quantized image, that is the optimal α providing the best trade-off throughout different scales.

3.5 OPTIMAL PIXEL MAPPING

In classical dithering algorithms, calibration is usually achieved using perception-related functionals, such as the structural similarity index measure (SSIM), that mimick human visual quality assessment [195, 228]. Although very good results can be obtained with such metrics [229], the method lacks physical interpretability. Here, we wish to provide a sounder entropy-based approach that captures the ability of images to retain information during compression, as shown in recent visual appreciation experiments [1]. To do so, we employ the formalism introduced in Ch. 2 and establish two approaches: a first one on the multiscale relevance (MSR) introduced previously, and a second one information cascading.

3.5.1 *Using the multiscale relevance*

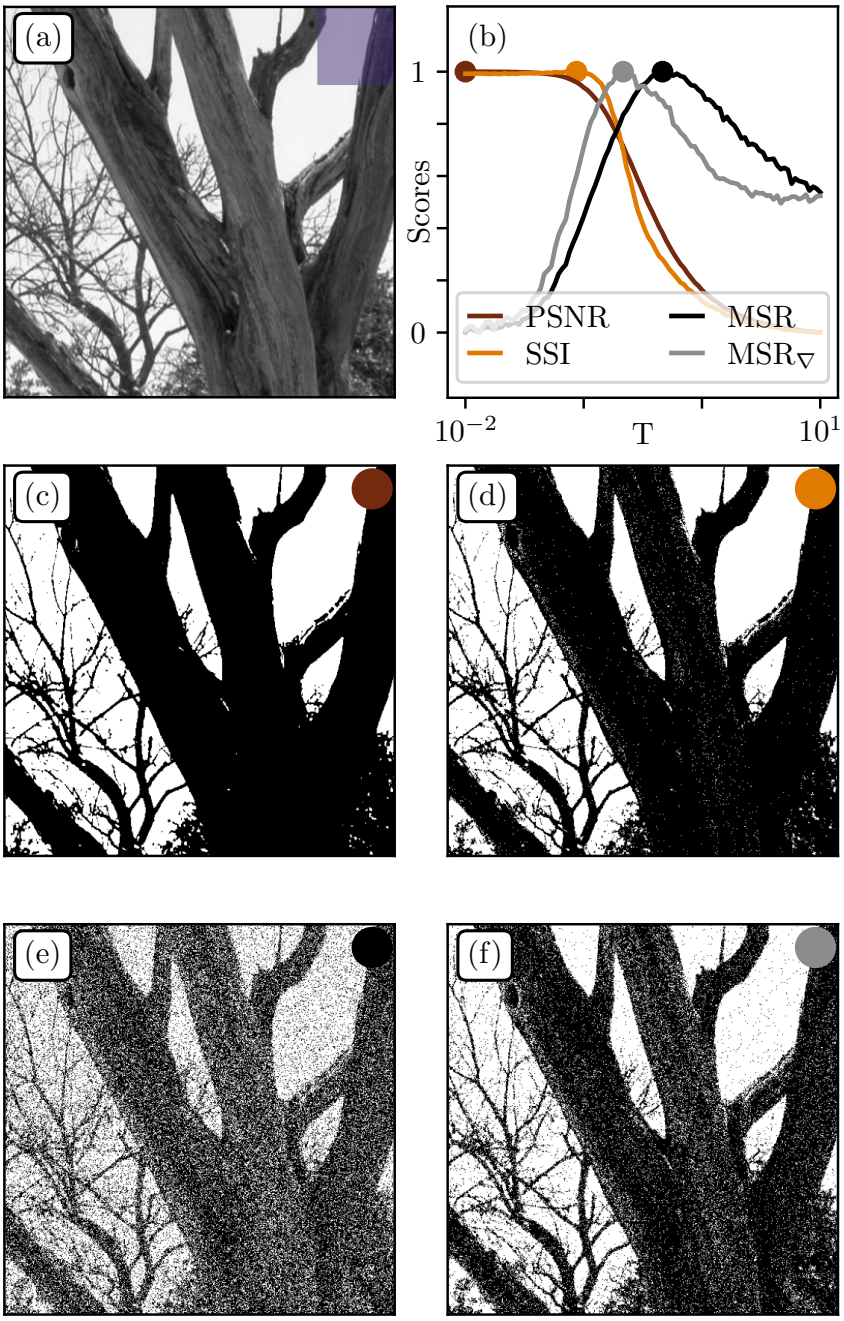

Figure 3.4: Color mapping. (a) Original patch from Fig. 2.6(a). (b) Rescaled scores as function of temperature for different performance measures: Peak Signal-to-Noise Ratio (PSNR), Structural Similarity Index (SSI), direct Multiscale Relevance (MSR), and MSR over the gradient field MSR_∇. (c),(d),(e), (f) Color mapping at optimal temperatures T^* for PSNR, SSI, MSR and MSR_∇ respectively.

We first consider the algorithm introduced in Sec.3.3.1. Classically, we found that the good visuals were obtained from temperatures T^* minimizing the mean convoluted squared error between original and reduced image. Here we propose an alternative approach consisting in maximizing the Multiscale Relevance (MSR) introduced in Ch. 2, and compare it to the same classical metrics as in Sec. 2.5, namely the Peak Signal-to-Noise Ratio (PSNR) [194] and the Structural Similarity Index (SSI) [195].

Figure 3.4(a) displays the original patch extracted from Fig. 2.6(a). Figure 3.4(b) shows the evolution of each metrics with temperature T. One sees that the PSNR between the original and mapped images is maximized at $T = 0$. This is not surprising as the PSNR is monotonously related to the MSE by definition. The corresponding mapping in Fig. 3.4(c) appears too sharp and contrasted, clearly separating vegetation from sky while introducing thresholding artifacts. Optimization of the SSI yields a non-zero yet small temperature $T = 0.1$, barely improving the resulting image (see Fig. 3.4(d)). We then compute the MSR for both direct and gradient fields. The maximization of MSR(T) leads to the image shown in Fig. 3.4(e), which contains more faithful visual features and a decent similarity to the original image at large scales, at the cost of artificial small scale features. Finally, the maximization of the gradient magnitude MSR [1], shown in Fig. 3.4(f), seems like a good compromise between (c),(d) and (e) as it also displays medium scale features (tree trunk details) without blurring finer ones (small branches).

Hence, for strong color reduction, a Multiscale Relevance approach can bring better visuals than classical metrics such as the Structural Similarity Index which, in addition, requires an *a priori* semantic knowledge of the original image. Note that the analysis could be extended to more elaborate color mapping procedure such as error diffusion [139, 230] or, Monte-Carlo based algorithms [142]. We shall see in the next section that a different approach with the same formalism provides consistent results.

3.5.2 *Using information cascading*

We get back to the Monte-Carlo algorithm introduced in Sec. 3.4. To find the most suitable kernel parameter α, we use an other interpretation of the Resolution/Relevance formalism based on the cascading of information across undersampling scales.

Here, instead of calculating the MSR, we stick to the two measures of entropy $\hat{H}^{\ell}[s]$ and $\hat{H}^{\ell}[k]$, and recall that they respectively assess heterogeneity in data and heterogeneity in data redundancy.

1 Note that to compute the gradient magnitude MSR, one has to segment the grayscale images obtained from the gradient procedure, and average over a.

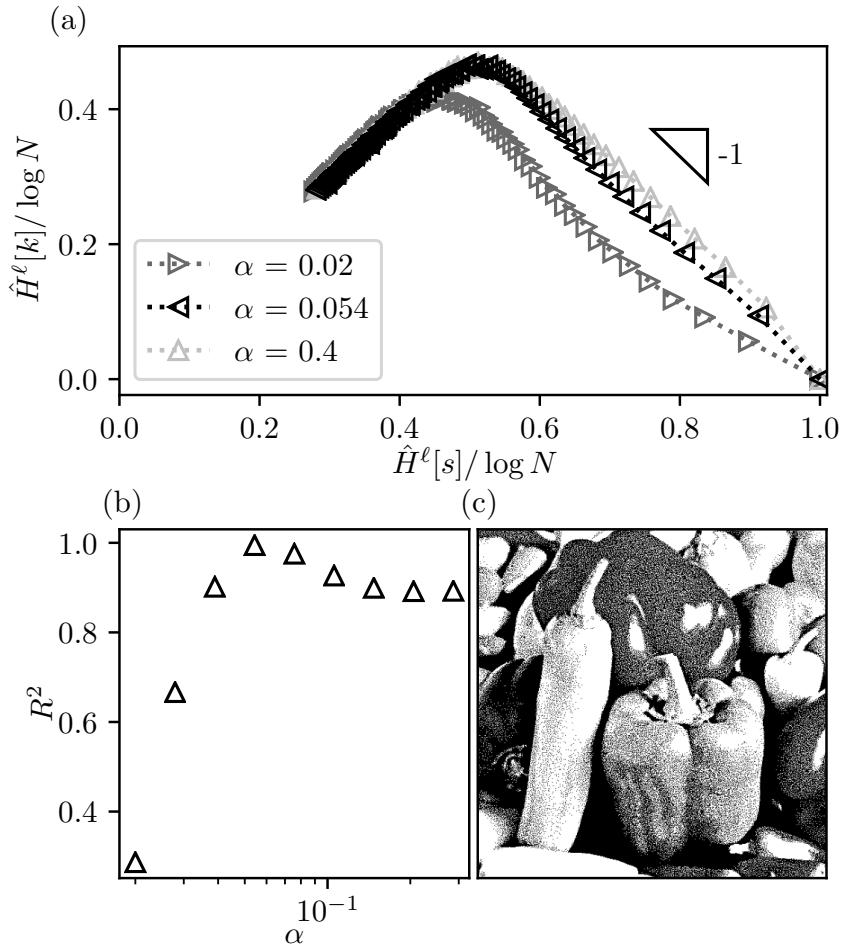

Figure 3.5: Influence of the convolution parameter α on the compressing regime of color quantized images. (a) Plot of $(H^\ell[s], H^\ell[k])_\ell$ for low, optimal and high convolution parameters α. (b) Regression coefficient R^2 of the linear fit as function of α. (c) Optimally quantized image, $\alpha = 0.054$.

In Fig. 3.5(a), we vary ℓ and plot $\hat{H}^\ell[k]$ as function of $\hat{H}^\ell[s]$ for images generated with different α. Of most interest to us here is the right part of the graphs, which corresponds to small values of ℓ, and for which the concavity of the curves is very α-dependent. This property reminds the shape of Relevance/Resolution curves for $1/f$ random textures, as was shown in Ch. 2 where the Hurst exponent H influenced the concavity of the Resolution/Relevance curves in the undersampling regime.

One can show – see Appendix B.3 – that the local slope $\mu = \mathrm{d}\hat{H}[k]/\mathrm{d}\hat{H}[s]$ actually corresponds to the trade-off rate between relevance and resolution as data is compressed. The idea is then to choose the convolution parameter such that this trade-off is as stable as possible across all scales of observations, meaning that μ should be close to -1 and as constant as possible when varying ℓ. In other terms, the

right part of the graph should be as linear as possible with slope -1. In Fig. 3.5(b) we plotted the regression coefficient R^2 obtained from the corresponding linear fit and found that it was maximized for an intermediate value $\alpha = 0.054$. The corresponding image is shown in Fig. 3.5(c) and is indeed a very good visual compromise.

3.6 BEYOND BLACK & WHITE

In this section, we illustrate how our method can be extended to other image types, color spaces and convolution kernels. We use four images from the USC-SIPI image database [219] (see Fig. 3.6, first column). For each image, we choose a different target color palette, namely B&W for Man pictures (first row), four grayscale levels for Bridge pictures (second row), eight colors (corresponding to the vertices of the RGB cube) for Peppers pictures (third row), and fifteen colors (corresponding to each point of the face-centered cubic arrangement in the RGB cube) for Mandrill pictures (fourth row).

First, we consider the $T \simeq 0$ case (second column). For each image, as in Sec. 3.3.1, the quantization process suppresses a large amount of details and produces thresholding artifacts such as contouring effects for shaded textures. Then, we increase the temperature and find the optimal $T^\star$ for each quantized image, see in third column. As it was the case for the B&W Peppers in Sec. 3.3.1, a clear improvement is obtained for each image at $T = T^\star$, with the reconstruction of features such as contours and shades. However, the latter are not yet fully consistent with the original image. The level of noise is still quite high when looking up close. Finally, we generate quantized images with the Monte-Carlo algorithm (fourth column) and test its robustness by using classical Gaussian kernels with standard deviation σ instead of power-law kernels. Using the method described in Sec. 3.5 we find, for all images, values of optimal $\sigma^* \approx 0.5$ pixels. The results are then much more satisfactory as the impression of color saturation and level of noise are significantly reduced. Note that our optimal kernels are slightly narrower than the classical error diffusion matrix kernels historically used in dithering algorithms, such as Floyd-Steinberg (FS) [139] or Jarvis-Judice-Ninke (JJN) [230]. The latter provide excellent results but their implementation does not allow for the tuning of the kernel width. For the sake of visual comparison, we have implemented the FS algorithm (fifth column) with indeed a slightly larger error dispersion (equivalent to $\sigma \simeq 0.9$ pixels). While the local FS algorithm takes a pragmatic and very efficient turn, our method is more global and above all allows for physical interpretability.

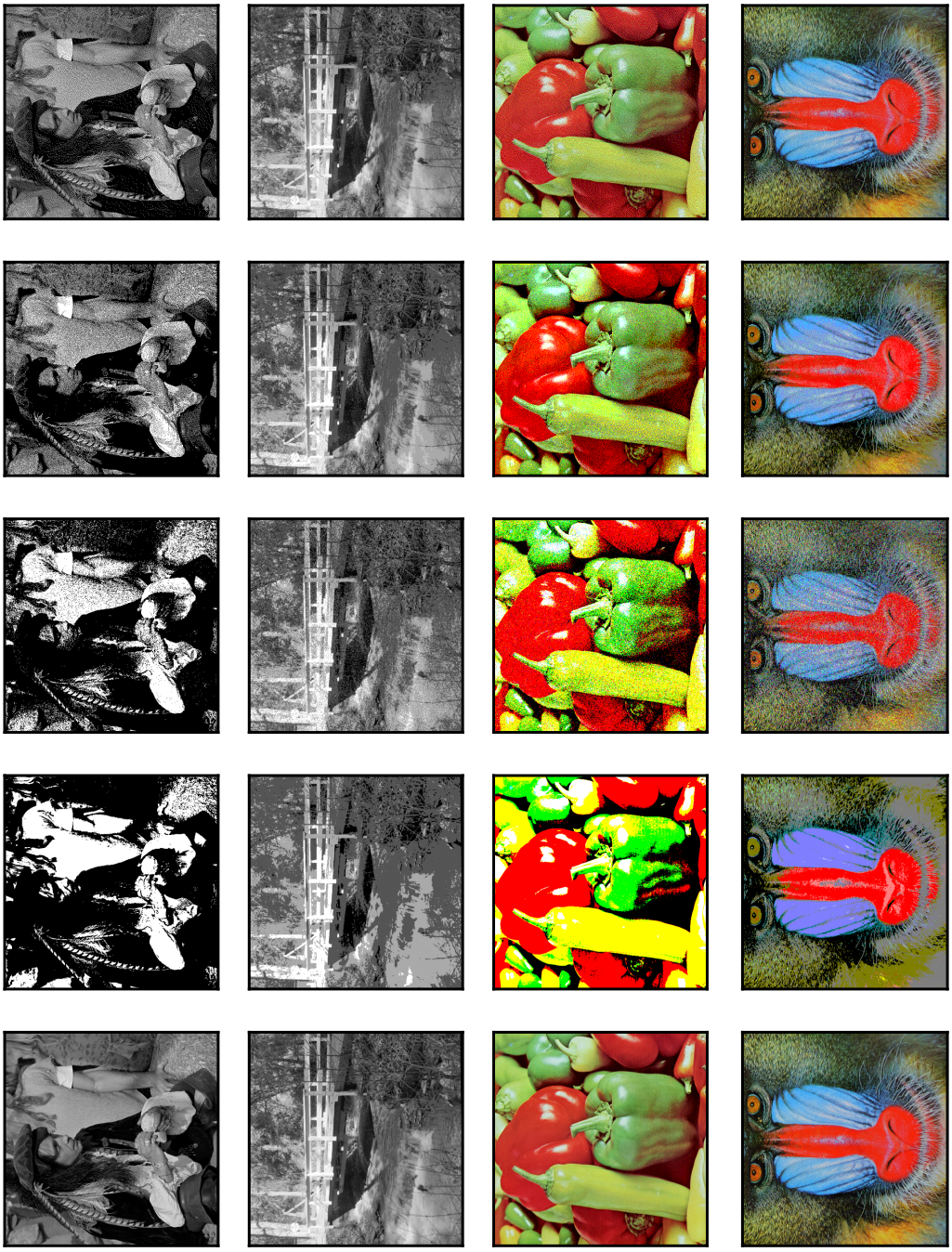

Figure 3.6: Extension to different image types and color palettes. From Left to Right: Original image, $T = 0$, $T = T^*$, $\sigma = \sigma^*$, and Floyd-Steinberg algorithm. From Top to Bottom: Man onto B&W, Bridge onto four grayscale levels, Peppers onto eight colors, and Mandrill onto fifteen colors.

3.7 CONCLUSION

Let us summarize what we have achieved. In the context of color quantization, we confirmed that the naive approach consisting in a

simple error minimization does not generally bring satisfactory visuals. To overcome this issue, we introduced thermal noise through a Maximal Entropy based approach and generated quantized images with more interesting visuals. To quantify this visual impression, and guided by [142], we introduced the Convoluted Squared Error, which compares the original and quantized fields after a coarse-graining procedure. Introducing convolution allowed us to find the optimal temperatures minimizing the new observable. Interestingly, we found that such temperatures are a good indicator for complexity at different scales. Moreover, having confirmed that the Convoluted Squared Error is a highly relevant observable with respect to color mapping, we directly minimized it to generate new images using a Monte Carlo algorithm. In order to find the optimal convolution parameter leading to the best visuals, we used the Resolution/Relevance approach that was introduced in Ch. 2. In particular, we explored two slightly different approaches, first enforcing maximal multiscale contributions, then aiming for uniform information cascading. Finally, we proved the robustness of our method against changes in image type, color palette, and convolution kernel. Note that, as mentioned in the introduction of the chapter, in the present analysis we have chosen the target color palette *ex ante*, focusing on simple cases, namely, B&W, 4 grayscale, RGB vertices and face-centered cubic. It would be interesting to consider extended color palettes where both the dimension and color values are optimized for a given image. The latter most likely depends on the features of the color histogram of the original image, but also their spatial arrangement. Future research should also be devoted to considering alternatives to the Euclidean distance such as perception based cost functions [225], structural similarity metrics [195], quality indices [227], distances including transport terms [231] or edge detection [225], which take into account *a priori* the local arrangement of the pixels.

3.8 TAKE-HOME MESSAGE

The color mapping problem consists in reducing the palette of an image (e.g passing from 256 to 2 grayscale levels).

However replacing each pixel by its closest color leads to thresholding artifacts.

We introduce noise from a maximal entropy approach. A parameter T relaxes the loss constraint, an approach at the core of statistical physics.

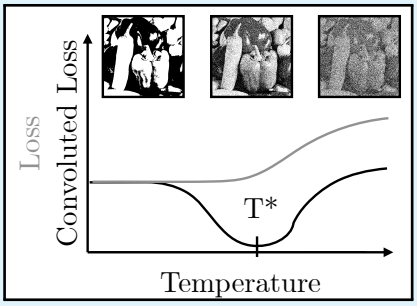

Best visuals correspond to temperatures T^* minimizing distance between blurred images (Convoluted Loss).

We minimize this convoluted loss from Monte-Carlo algorithm, and recover good visuals. The kernel shape can be calibrated from multiscale entropy arguments, introduced in the previous chapter.

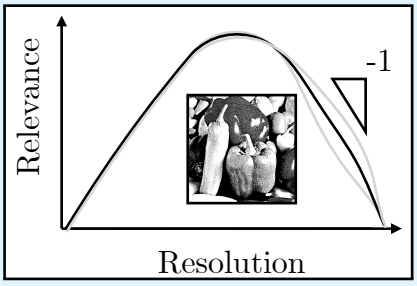

Part II

STATISTICAL ANALYSIS OF FRACTURE SURFACES.

4

MULTIFRACTAL FIELDS: WRAPPING AND UNWRAPPING

"Do you know what the B in Benoit.B Mandelbrot stands for?"
"Benoit.B Mandelbrot."

This chapter should be included in a forthcoming publication [4], written in collaboration with Laurent Ponson, Michael Benzaquen and Jean-Philippe Bouchaud, and the results of which are based on my doctoral works. The final publication may slightly differ.

4.1 INTRODUCTION

Whether in the oceans [232], in the sky [233–235], or in the mountains [30], scale invariance is everywhere around us. This feature, formalized and popularized by Mandelbrot's under the concept of fractals [236–238], has reached a general audience, who can recognize and appreciate their unfathomable beauty. For physicists, systems are said to be fractal when their observables display deterministic or statistical invariance under affine transformations of their space-time variables. In linear systems, this property is straightforward from the study of momentum equations. For non-linear systems however, the knowledge of governing equations, rarely allows the prediction of scale invariance, apart from some specific cases [56]. In such situations, scale invariance may emerge from a wide range of mechanisms such as self-organization [239], exotic fluctuations [240], or hierarchical structures. For that last situation, the most classic example may be of fluid turbulence, for which the scale invariance originates from the cascading of energy through large eddies at injection/forcing scale to small ones at dissipation scale [35, 241]. [35, 241]. These strongly coupled systems often display unique statistical signatures, including non-Gaussian fluctuations and multifractal scalings [33, 154], absent of linear fractal systems. In particular, multifractality occurs when the fluctuations of an observable $h(\boldsymbol{r})$, $\boldsymbol{r} \in \mathbb{R}^d$ can no longer be described by a unique scaling parameter. In that case, one introduces a continuous exponent spectrum ζ_q that describes the moments of these fluctuations, which under isotropic statistics translate as the following variogram property:

$$V_q(\delta r) = \langle |h(\boldsymbol{r} + \boldsymbol{\delta r}) - h(\boldsymbol{r})|^q \rangle_{\delta r = \|\boldsymbol{\delta r}\|} \sim \delta r^{\zeta_q}, \tag{4.1}$$

where $\langle . \rangle$ refers to spatial or ensemble average. A linear spectrum $\zeta_q = qH$ corresponds to monofractal scaling, described by its Hurst

exponent H alone. Instead, multifractals are characterized by a nonlinear spectrum $\zeta_q \neq qH$, a property reported in many forced nonlinear systems [143, 154, 242, 243].

What are the minimal ingredients leading to the formation of multifractals? We address this question from a geometrical, algorithmic perspective, by constructing multifractals using a few basic building blocks. Yet, we show that the construction and the deconstruction of multifractal fields – that is, their *wrapping* and *unwrapping* – may provide rich insights about the basic physical processes leading to their formation.

Algorithms generating fractals can provide essential insights in the understanding and description of scale invariant phenomena. But synthetic fractals also find multiple applications in physics and engineering. They serve as test-beds for developing accurate characterization techniques of scale invariant signals [244]. They are used in computer visions, to create a myriad of different patterns like landscapes, clouds, trees... They are also employed in direct numerical simulations of phenomena like frictions between rough surfaces [245], flows in fractured rocks [246, 247] or financial markets [205]. More recently, generation algorithms have been used to create unlimited database of perfect fractal objects to train neural networks that show promises for various applications, including the recognition and characterization of natural (imperfect) fractals [248–250]. As a result, various methods have been developed for the generation of monofractals such as noise filtering, cellular automaton or iterative methods [55, 251, 252]. For multifractals however, generation methods are scarce and generally limited (but see [205] and refs therein). Stochastic differential equations simulations [242] are restricted to some specific scaling properties. While direct sampling methods suffer from several important limitations including the lack of symmetry [253], isotropy and continuous scale invariance [254]. On top of it, extending these methods to $d > 1$ raises severe difficulties.

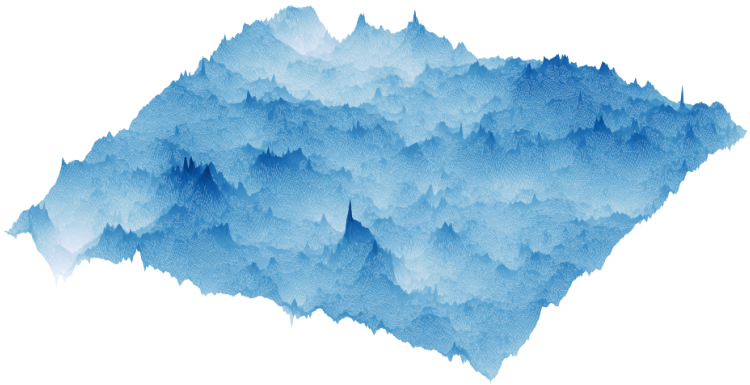

Figure 4.1: Synthetic multifractal field in dimension $d = 2$.

In this chapter, we provide a powerful, yet simple method for the generation of multifractal random fields of any dimensions, an example of which is provided in Fig. 4.1 for $d = 2$. Our model builds on the work of Bacry *et al.* [255] who defined a multifractal process with continuous dilation invariance properties, and that we generalize to higher dimensions by using fractional operators.

In practice, as described in the first two parts of this chapter, our method consists of three steps. First, a log-correlated Gaussian field $\omega(\boldsymbol{r})$ of finite correlation range ξ is defined. Taking its exponential and forcing its symmetry defines a *non-Gaussian* fluctuation field $\delta h(\boldsymbol{r})$ which is ultimately integrated into a multifractal fields $h(\boldsymbol{r})$ of fully controlled scaling properties, and show how to calculate the density probability of increments at any scale $\Delta r < \xi$, from the parameters λ and H alone.

The second part of our chapter is dedicated to the comparison of these synthetic fields with an experimental multifractal field, the surface of a fractured metallic alloy. We evidence subtle differences between both fields, providing insights on the dissipation mechanism terminating the cascading processes in fracture problems. We conclude this chapter by discussing the implications of our method for the study of strongly-coupled processes leading to multifractality, and to the in-depth characterization of fracture surfaces, a topic that will be continued in Ch. 5.

4.2 SYNTHESIS OF MONOFRACTAL FIELDS

4.2.1 *Monofractal fields*

Monofractal Gaussian fields $\omega(\boldsymbol{r})$ ($\boldsymbol{r} \in \mathbb{R}^d$) can be defined from the application of fractional operators to white Gaussian noise. In dimension $d = 1$, these operators derive from classic integration and derivation [256]. For $d > 1$, one must pass through the Fractional Laplacian $(-\Delta)^\alpha$ [257] and define the field from

$$\omega(\boldsymbol{r}) = (-\Delta)^{-\frac{H+d/2}{2}} \eta(\boldsymbol{r}), \tag{4.2}$$

where η is a white Gaussian noise of dimensions d. In Fourier space, the operation amounts to use the filter $G(\boldsymbol{k}) = 1/k^{H+d/2}$ ($k = \|\boldsymbol{k}\|$), which possesses scale and rotation invariance [1]. We may distinguish two main families of power-law correlated fields. For $H \in [-d/2, 0[$, $\omega(\boldsymbol{r})$ is a zero mean stationary Gaussian fields with power-law correlations $C(\boldsymbol{\delta r}) = \langle \omega(\boldsymbol{r} + \boldsymbol{\delta r}) \omega(\boldsymbol{r}) \rangle \propto \delta r^{2H}$. For $H \in]0, 1]$, $\omega(\boldsymbol{r})$ is a fractional Gaussian field [258, 259] of monofractal scaling $V_q(\boldsymbol{\delta r}) \propto \delta r^{qH}$. The particular case $H = 0$, lying at the transition between both cases,

1 In a lattice space of step 1, the Laplacian is expressed in terms of nearest neighbours increments, which is equivalent in the Fourier space to replacing $\|\boldsymbol{k}\|^2$ by $\sum_{i=1}^{d} (2 - 2\cos k_i)$.

corresponds to system size dependent logarithmic scaling when the self-affine regime is unbounded.

4.2.2 *Integral range*

To mimic natural fractals that expand over a finite range of length scales, we introduce an upper cutoff ξ using the modified operator $(-\Delta) \to (1/\xi^2 - \Delta)$ that damps long-range correlations. In Fourier space, this translates as $k^2 \to (2\pi/\xi)^2 + k^2$, which regularizes low frequencies. A few calculations [260] provide the correlations of ω, $C_\omega(\boldsymbol{\delta r}) \propto \delta r^H K_H(\delta r/\xi)$, where K_H is the modified Bessel function of the second kind with parameter H. We retrieve the classic Whittle-Matérn correlations [261, 262] which behave similarly to unregularized fields at short scales $\delta r \ll \xi$, and decay exponentially $C_\omega \propto e^{-\delta r/\xi}$ in the limit $\delta r \gg \xi$. Taking $H = 0$ recovers logarithmic scaling $C_\omega(\boldsymbol{\delta r}) \propto -\log(\Delta r/\xi)$ over a finite range of length scales $\delta r < \xi$.

4.3 MULTIFRACTAL FIELDS FROM THE MULTIFRACTAL RANDOM WALK

4.3.1 *Building non-Gaussian fluctuations*

We now wish to build non-Gaussian fluctuations by applying several transformations to the Gaussian field $\omega(\boldsymbol{r})$ constructed previously. In a first step that is amenable to analytical tractability, we introduce

$$\sigma(\boldsymbol{r}) = e^{\omega(\boldsymbol{r})}, \tag{4.3}$$

which explodes the largest fluctuations of ω while tempering the lowest ones, see Fig 4.2. Such signals, also referred to as crackling noise, are observed in driven disordered elastic systems where the largest fluctuations organize in bursts called avalanches [263]. The Gaussian statistics allow for the computation of the q-point correlation function of σ:

$$C_\sigma(\boldsymbol{r_1}, \dots, \boldsymbol{r_q}) := \left\langle \sigma(\boldsymbol{r_1}) \dots \sigma(\boldsymbol{r_q}) \right\rangle = e^{-\sum_{1 \le i \le j \le q} C_\omega(\boldsymbol{r_i}, \boldsymbol{r_j})}, \tag{4.4}$$

where $\boldsymbol{r_1}, \dots, \boldsymbol{r_q} \in \mathbb{R}^d$. This expression simplifies for $H = 0$ leading to $C_\omega(\delta \boldsymbol{r}) = -\lambda \log(\Delta r/\xi)$ where the *intermittency* coefficient λ and the length scale ξ control the strength and the spatial extension of the bursts of σ respectively. The resulting process is referred to as a *log-normal continuous cascade* [264].For $\|\boldsymbol{r_i} - \boldsymbol{r_j}\| \ll \xi$, Eq. (4.4) simplifies to:

$$C_\omega(\boldsymbol{r_1}, \dots, \boldsymbol{r_q}) \propto \prod_{1 \le i \le j \le q} \|\boldsymbol{r_i} - \boldsymbol{r_j}\|^{-\lambda}, \tag{4.5}$$

which displays scale invariance, as applying $\boldsymbol{r_i} \to \gamma \boldsymbol{r_i}$ multiplies C_ω by $\gamma^{-\frac{\lambda}{2} q(q-1)}$. We will see that this quadratic scaling in q directly influ-

ences the multi-affine spectrum of sampled fields.

4.3.2 *Synthetic multifractal fields*

It was shown in [253, 265] that multiplicative cascades like σ could be fractionally integrated into multifractal fields. However, such construction leads to skewed statistics which do not reproduce the symmetry observed in experimental data, e.g. turbulence velocity fields [153, 266, 267]. The solution introduced by Bacry, Delour and Muzy for the Multifractal Random Walk (MRW) [255] consists in symmetrizing the fluctuations using the following operation:

$$\delta h(\boldsymbol{r}) = s(\boldsymbol{r})\sigma(\boldsymbol{r}), \tag{4.6}$$

where s is a zero-mean white Gaussian noise that enforces $\delta h \to -\delta h$ invariance. Here, σ defines an intermittent volatility envelope in which δh fluctuates, as shown in Fig. 4.2. For $d = 1$, δh exactly defines the increments of the MRW and an integration retrieves a multifractal signal. For $d > 1$, multifractal fields are sampled using the fractional integration of fluctuations:

$$h(\boldsymbol{r}) := (-\Delta)^{-\frac{H+d/2}{2}} \delta h(\boldsymbol{r}). \tag{4.7}$$

Similarly to the construction proposed in [268], these fields display an asymptotic ($\Delta r \ll \xi$) multifractal scaling of exponent spectrum:

$$\zeta_q = qH - \frac{\lambda}{2} q(q-2), \tag{4.8}$$

as shown in Appendix. C.2. In $d = 1$, taking $H = 1/2$ provides the MRW. This corresponds to the MRW scaling for $H = 1/2$. In the general case, the constructed field recovers monofractality with $\zeta_q = qH$ for $\delta r > \xi$. Note that introducing a second cut-off ξ_h in the last integration step leads to a saturation of the variograms for $\delta r > \xi_h$, as observed in experimental data [35, 269] and simulations [154, 242].

4.3.3 *Intermittency characterization*

We verify the effectiveness of our method by generating surfaces of size 512×512 pixels, as the one shown in Fig. 4.3(a) for $H = 0.5$, $\lambda = 0.1$ and $\xi_\omega = 32$. We first check its multifractal properties: in Fig. 4.3(c), where the power-law exponents of the rescaled variograms $(V_q)^{1/q}$ are computed in the multifractal regime $\Delta r < \xi$. We observe in Fig. 4.3(d) that the generalized Hurst exponents $H_q = \zeta_q/q$ follows the linear behavior $H_q = H - \lambda/2\,(q-2)$ expected from Eq. (4.8). Note that the multi-affine to mono-affine crossover ξ is evidenced from the collapse of the rescaled variograms $(V_q)^{1/q}$ for $r > \xi$.

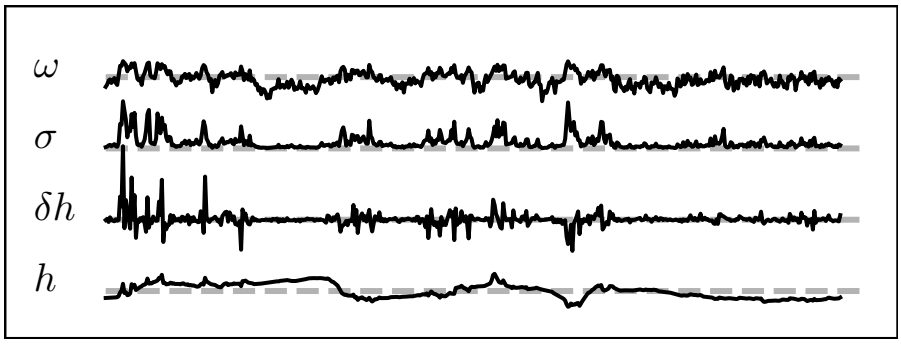

Figure 4.2: Step-by-step construction of multifractal signals, extracted here from surfaces of dimension d = 2. From top to bottom, log volatility ω from Eq. (4.2), volatility σ from Eq. (4.3), fluctuations δh from Eq. (4.6) and multifractal field h from Eq. (4.7). Horizontal dotted lines indicate the origin $y = 0$ of each signal. To go from one signal to the other, we use the following operations: exponentiation, symmetry forcing and fractional integration.

As shown in the following and as previously reported in [270, 271], the analysis of h only may be insufficient to ascertain multifractal properties. This difficulty can be circumvented by studying directly the field ω introduced previously. For MRW, λ and ξ can be measured from the local log-volatility field $\hat{\omega}_\epsilon = \log|\delta_\epsilon h|$ [272, 273], also called *magnitude* [274] or log-dissipation rate in turbulence. For multifractal fields, h can be unwrapped using the operator [253]:

$$\hat{\omega}(\boldsymbol{r}) = \log|(-\Delta)^{\frac{H+d/2}{2}} h(\boldsymbol{r})|, \tag{4.9}$$

which differs from previous studies [143, 275] by fully factoring in the effect of the roughness exponent H. The obtained log-volatility field, shown in Fig. 4.3(b), displays long-range correlations reminiscent of the multifractal properties of the original field $h(\boldsymbol{r})$ shown in Fig. 4.3(a). The fit of the correlations of $\hat{\omega}(\boldsymbol{r})$ by $C(\delta r) = -\lambda \log(\delta r/\xi)$ provides $\lambda = 0.15$ and $\xi = 32$, matching fairly well their prescribed value. In order to assess the versatility of our method, we generate a wide variety of multifractal fields of size 512×512 with prescribed properties in the range $0 \leq \lambda \leq 0.5$ and $0 \leq H \leq 1$ for a fixed cut-off length $\xi = 30$ (see Fig. C.2 and C.3 in Appendix. C.4). The parameter values λ and H are then measured either from the volatility field $\hat{\omega}(\boldsymbol{r})$ or the height field $h(\boldsymbol{r})$. We find a good agreement with the prescribed values, especially when the $\hat{\omega}$-field is used, suggesting that the study of the spatial correlations of the volatility field is a more direct, and accurate way to characterize multifractal fields.

4.3.4 *Non-Gaussian statistics of increments*

The multifractal scaling directly implies that increments $\delta_{\delta r} h = h(\boldsymbol{r} + \delta\boldsymbol{r}) - h(\boldsymbol{r})$ are linked together through a scale invariant cascading

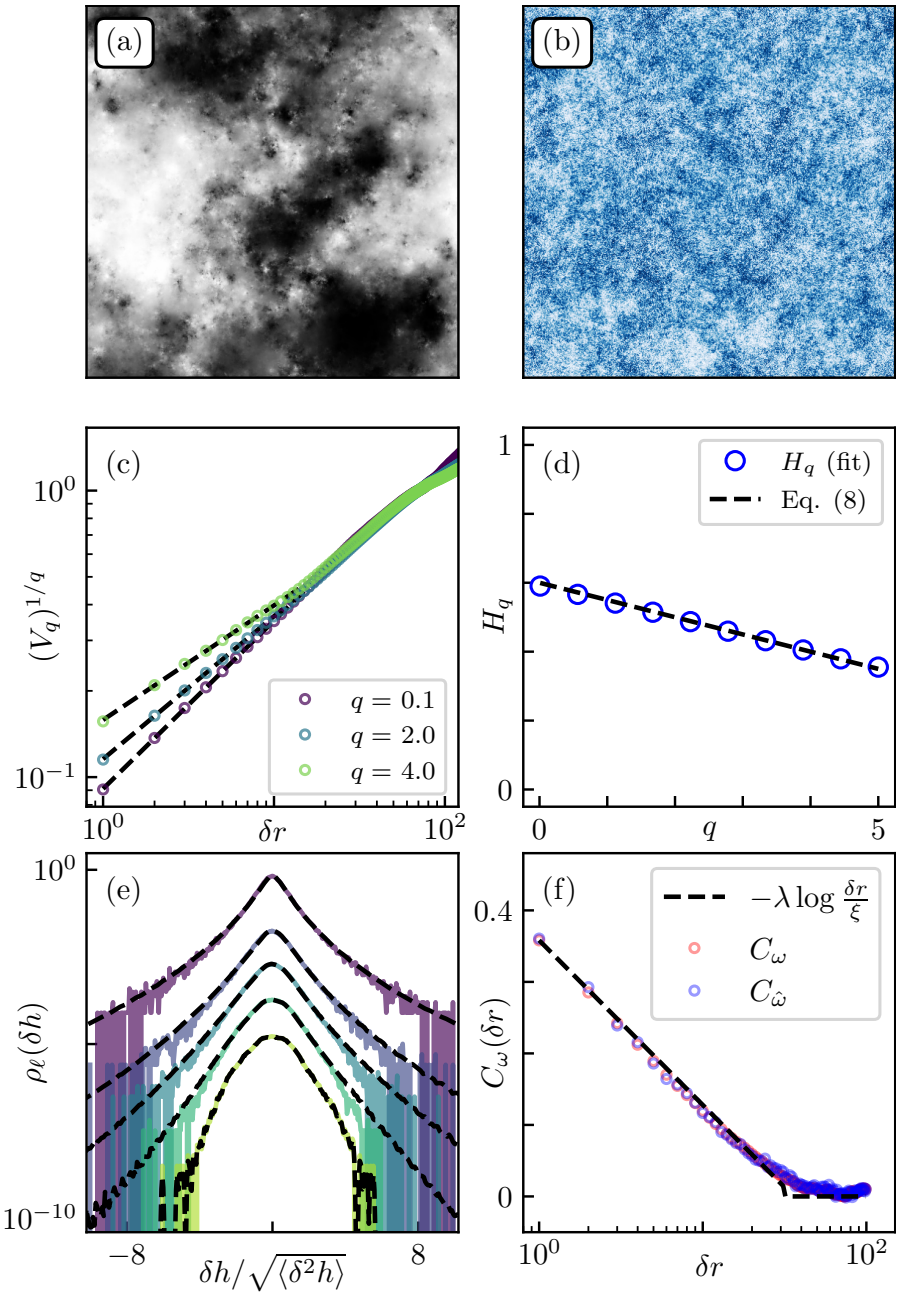

Figure 4.3: Synthetic multifractal field in dimension $d = 2$, of size 512×512, with parameters $(H, \lambda, \xi) = (0.5, 0.1, 32)$. (a) $h(\boldsymbol{r})$. (b) $\omega(\boldsymbol{r})$. (c) Rescaled variograms with their power law fits. (d) Generalized Hurst exponents, as obtained from the fit of the variograms and their comparison with the linear prediction of Eq. (4.8). (e)Distributions of fluctuations computed at scales $\epsilon/\xi = 1/32, 1/16, 1/8, 1/4, 1/2$ and 1. (Top to Bottom, shifted for illustration)and their comparison with the distribution computed from Eq. (4.10) using $L = \xi$ as a reference length scale. (f) Correlations of ω and $\hat{\omega}$ and comparison with the expected logarithmic correlations.

rule. Indeed, the fluctuation ratios $W_{\ell/L} = \delta_\ell h/\delta_L h$ are such that $\langle W^q_{\ell/L}\rangle = (\ell/L)^{\zeta_q}$ and depend on the scale ratios exclusively. As proposed by Castaing *et al.* [153], this relation can be used to link the probability density functions (p.d.f) $\rho_{\delta r}(\delta h)$ to the following dilation invariance:

$$\rho_\ell(\delta h) = \int G_{\ell/L}(u) e^{-u} \rho_L(e^{-u}\delta h) du. \tag{4.10}$$

The kernel $G_{\ell/L}(u)$ is the Gaussian p.d.f of $\log W_{\ell/L}$, that depends on ζ_q, and thus on H and λ only. We provide its expression in Appendix. C.3, as well as the p.d.f of the fluctuation ratio $W_{\ell/L}$. In practice, the statistics of fluctuations is computed at the scale $L = \xi$ from which the statistics at smaller scales is inferred using Eq. (4.10). This construction provides an alternative characterization of the multifractal behaviour of h, as it captures quantitatively the ever stronger departure from Gaussianity as we go deeper into the multifractal regime. In Fig. 4.3(e), we compute the distributions $\rho_\epsilon(\Delta h)$ on our synthetic surfaces and observe the expected transition from fat to Gaussian tail as ℓ increases. The numerical data is in perfect agreement with Eq. (4.10).

4.4 APPLICATION TO EXPERIMENTAL DATA

We now consider experimental multifractal data, here the height map of a fractured metallic alloy measured by interferometric profilometry (see Fig. 4.4(a)). Fracture surfaces are archetypes of multi-affine fields [143], even though the physical origin of their complex geometry is still debated [152, 276, 277]. The analysis carried before on synthetic fields is implemented in Fig. 4.4 to the experimental fracture surface, leading to the parameter values $(H, \lambda, \xi, \xi_h) = (0.63, 0.15, 33\mu\text{m}, 360\mu\text{m})$.

First, we recover all the salient features of our MRW-based multifractal fields, namely a linear decay $H_q = H - \lambda/2\,(q-2)$ of the exponents and a log-correlated $\hat{\omega}$-field. Notice however in Fig. 4.4(c) the slow transition towards monofractal scaling, a feature that also manifests in the statistics of height fluctuations shown in Fig. 4.4(e) that show significant deviations to Gaussian statistics even for $\epsilon \simeq 2\xi$. This soft crossover towards a Gaussian mono-affine behavior may result from the particularly marked cliff-like patterns of the fracture surface, a feature that is investigated in more details below.

This cliff-like organization is highlighted in Fig. 4.5(b) that shows the 10% largest values of $\hat{\omega}$. The most intermittent clusters organize in filamental structures, while they are more compact for the synthetic field shown in Fig. 4.5(a). The difference between both patterns is reminiscent of the dissipation mechanism in fracture problems that takes place through a cascading phenomenon culminating through the formation of mesoscale structures of size ξ. To explore these differ-

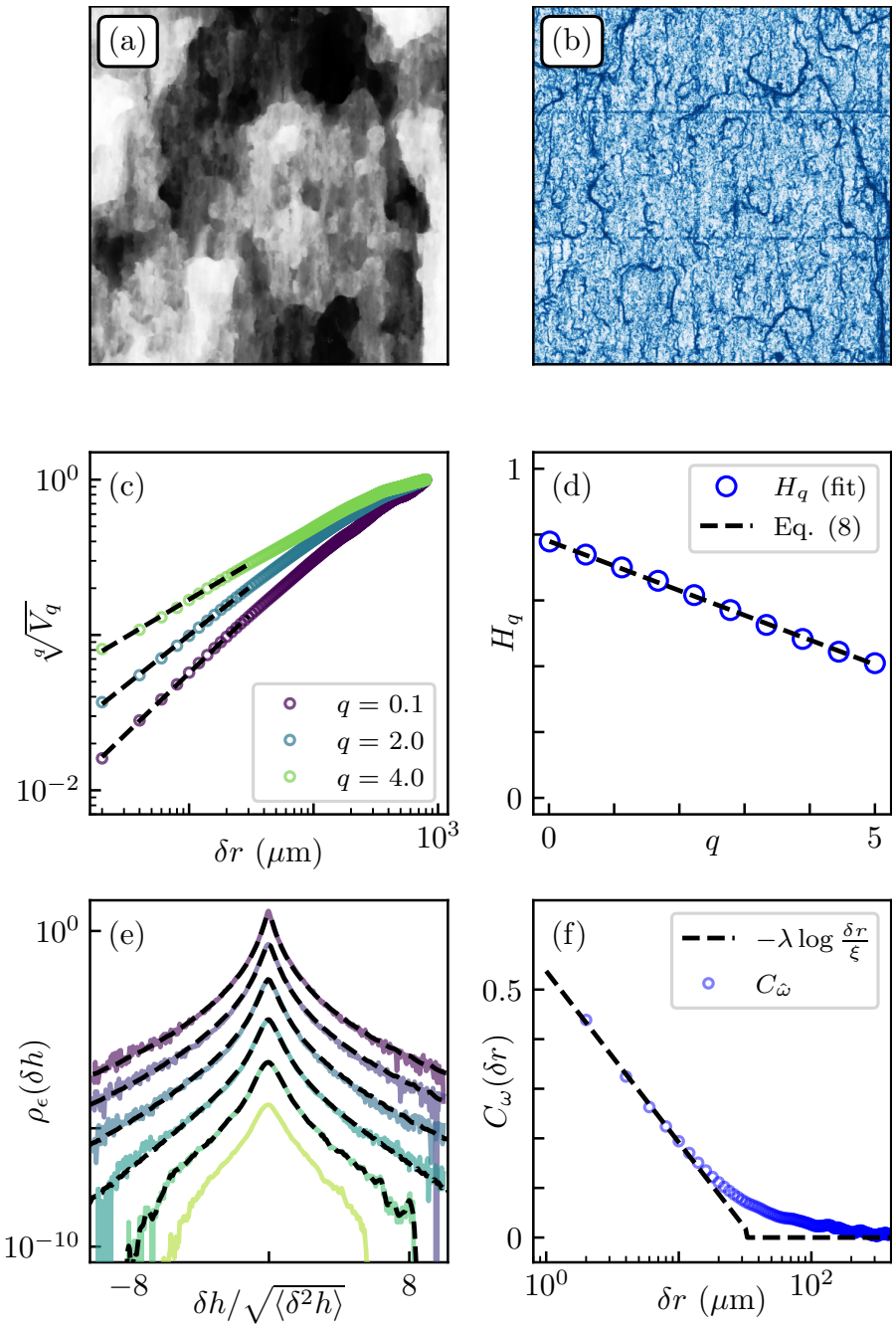

Figure 4.4: Unwrapping of an experimental multi-affine field. (a) Height map $h(\boldsymbol{r})$ of a fractured metallic alloy of size 2×2 mm^2 with 2 μm/pixel. (b) $\hat{\omega}(\boldsymbol{r})$ field, retrieved from Eq. (4.9). (c) Rescaled variograms. (d) Comparison of the exponents $H_q = \zeta_q/q$ with the prediction of Eq. (4.8) using $H = 0.63$ and $\lambda = 0.15$. (e) Distribution of fluctuations computed at scales $\epsilon/\xi = 1/16, 1/8, 1/4, 1/2, 1$ and 2 and their comparison with the distributions computed from Eq. (4.10) using $L = \xi$. (f) Correlations of $\hat{\omega}$ and comparison with the expected correlations using $\lambda = 0.15$ and $\xi = 33\mu$m.

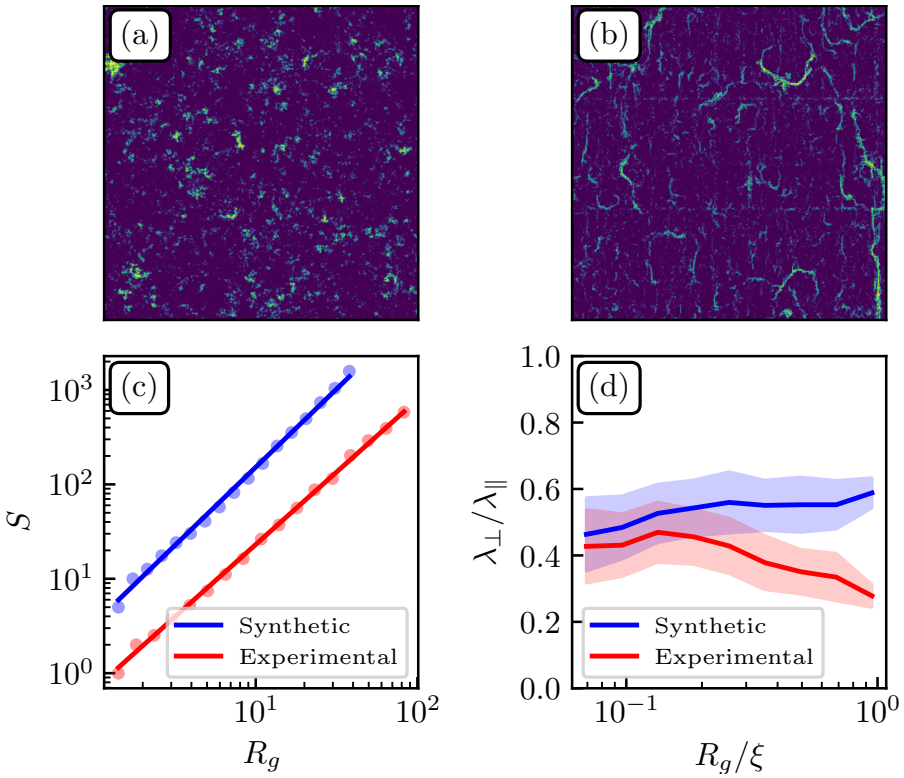

Figure 4.5: Cluster analysis of ω fields. (a) and (b) Volatility fields of artificial and experimental surface, thresholded at $p_c = 0.9$. (c) Fractal dimension analysis of clusters, defined from nearest-neighbour rule. We recover $D = (1.65 \pm .03, 1.53 \pm .02)$ for synthetic and experimental clusters respectively. (d) Ratio of the two eigenvalues of the clusters' inertia tensor as a function of their size, showing that larger clusters are more elongated than predicted by the model.

ences, we first compute the fractal dimension D of these clusters [143], as shown in Fig. 4.5(c). Their area S and their spatial extension R_g defined as the gyration radius scales as $S = R_g^D$ for both types of clusters with nearly the same exponent, even though the fractal dimension for the synthetic surface (that display more compact features) is slightly larger ($D \approx 1.65$ instead of 1.53).

We go one step further in Fig. 4.5(d) by comparing the clusters aspect ratio, defined as the ratio $\lambda_\perp/\lambda_\parallel < 1$ of the lowest and highest eigenvalues of their inertia tensor. The lower aspect ratio of the experimental dissipation clusters features their filamental structure, a topology reminiscent of kinetic energy dissipation bursts in fluid turbulence. Understanding the emergence of this filamental topology from the basic dissipation mechanisms taking place within the *fracture process zone* may shed light on the microscopic origin of the fracture energy of materials, a topic addressed in the next chapter.

4.5 CONCLUSION AND DISCUSSION

We now summarize our main findings and discuss their implications for the study of multifractal phenomena. We first generated monofractal Gaussian fields of Hurst exponent H and range ξ from which we built log-normal cascades by exponentiation in the case $H = 0$. This constitutive brick was then used to compute symmetric non-Gaussian fluctuations δh whose fractional integration led to synthetic multifractal random fields with quadratic scaling exponents ζ_q. The fields generated by our method retrieves all the salient features of classic multifractal random walks, which are quadratic scaling exponent spectrum, log-correlated volatility and a transition from Gaussian distribution to fat-tail statistics. Our method is limited here to the generation of isotropic multifractals, but anisotropy observed in many experimental systems, in particular fractures surfaces [278, 279], can be retrieved using anisotropic kernels. Our method provides multiscaling asymptotically, but exact multiscaling may be recovered by domain warping [280] of fractional Brownian fields with multifractal measures [281].[2]

One important contribution is, we believe, the idea of applying our methodology "backwards" such as to *unwrap* experimental multifractal fields and identify the singularities responsible for multifractality. In the case of the height map of a fractured material, we identify and characterize all the basic ingredients used to construct synthetic fields, but also highlight some fundamental differences, such as the softer crossover towards monofractality beyond ξ (see Fig. 4.4(f)) and the non-trivial topology of the intermittent bursts (see Fig. 4.5(d)). This last property is reminiscent of the inverse cascade in 2D turbulence, where vorticity filaments appear at large scales [283, 284]. It suggests that during material failure cooperative coalescence of damage cavities take place and culminates in the formation of large-scale cliff-like filamental structures. A next step in that investigation may rely on coagulation based descriptions [285], where such cavities are continuously absorbed and created in the vicinity of the crack tip.
We will see in Chapter. 5 that, in the case of rock surfaces, these structures indeed encode rich information about the dissipative processes controlling the fracture energy of materials, and in particular the characteristic size ℓ_c of the *Fracture Process Zone*.

2 Circulant embedding and real-time resampling [282] also constitute possible alternatives to generate multifractals with minor discretization and finite size effects.

4.6 TAKE-HOME MESSAGE

Monofractal fields can be built from the fractional laplacian operator $(-\Delta)^{\alpha}$, which simply translates as a power law kernel in the Fourier space.

Multifractal fields can be built by extending the Multifractal Random Walk model to higher dimensions.

Sampled fields verify multifractal characterizations on their (i) variogram scaling, (ii) volatility correlations and (iii) increments distribution.

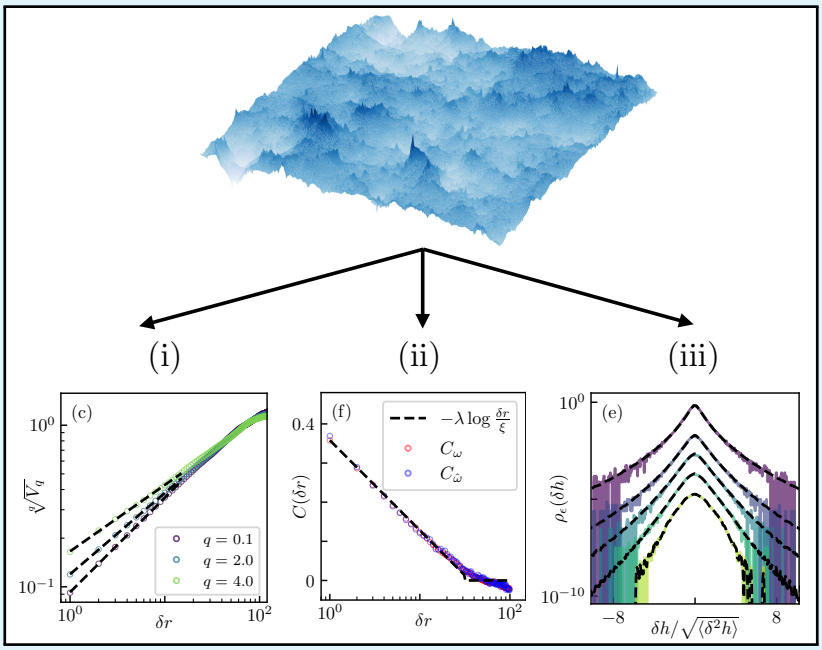

While experimental data can display proper multifractal properties, the study of intermittency bursts reveals non-trivial topology, which depends on the physics at play.

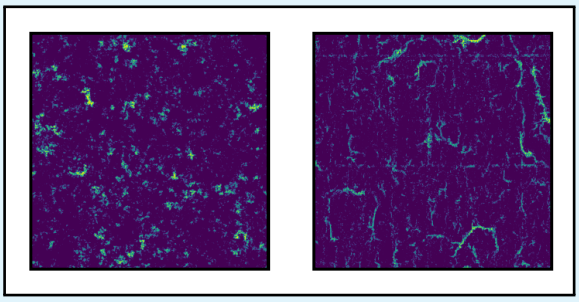

For fracture surfaces, these clusters are reminiscent of dissipative structures found in turbulence, and may encode further informations about the fracture properties of materials.

5

DECIPHERING THE INTERMITTENCY OF EXPERIMENTAL FRACTURE SURFACES

On ne sort de l'ambiguïté qu'à son détriment.

— Cardinal de Retz

5.1 INTRODUCTION

Ensuring the mechanical integrity of parts and structures is a necessary component of pretty much all engineering applications. To address this issue, powerful theoretical frameworks, among which fracture mechanics and damage mechanics, have been developed and thoroughly tested experimentally. The ability of materials to sustain mechanical loads serves as essential input of these predictive models. For describing the failure behavior under tensile loading, we then generally introduce two intrinsic properties of solids: their fracture energy (or toughness) that describes the ability of a material to resist to crack propagation and their cohesive strength that describes the ability of a material to resist to crack initiation. Despite the pivotal role played by these two properties, their microscopic origin remain partly obscure for a wide range of materials.

At small scale, cracks propagate through the accumulation and then the coalescence of damage (like e.g. microcracks) within a so-called process zone located at the crack tip vicinity (see Fig. 5.1). The way this damage spreads at the microscopic scale and ultimately sets the fracture properties measured at the macroscopic scale is still out of reach of fracture models. As a result, understanding quantitatively what makes a given material tougher than another one remains a very hard problem.

The morphological features observed on fracture surfaces of failed materials represent the sequels of these damage mechanisms. As a result, fractography, the science of examining fracture surfaces, has been one of the favourite techniques to study damage processes involved in material failure. However, standard fractography can only provide qualitative insights on microscopic failure mechanisms. As an alternative, it was proposed, as early as in the 80s [286], that the rough topography of fracture surfaces and its statistical features could be used as a field of investigation to unravel quantitatively the microscopic origin of the failure properties of materials [144, 145]. Unfortunately, this expectation has not been fully fulfilled yet. The reason may lie in the high complexity of the statistics of fracture surface, a

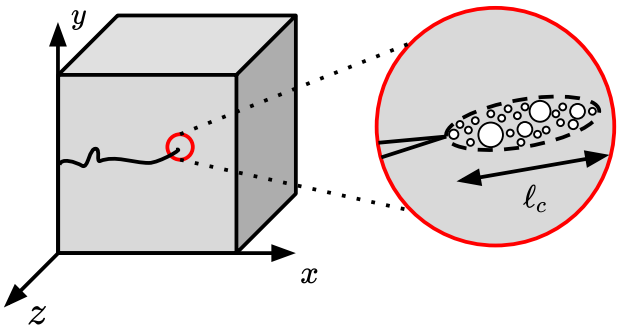

Figure 5.1: The microscopic view of failure. At large scale, failure results from the seemingly continuous propagation of a crack. Yet, zooming at the crack vicinity, one observes that cracks grow by coalescing cavities in a so-called *damage process zone* of size ℓ_c.

feature reminiscent of the high complexity of the mechanisms at the origin of the failure resistance of materials.

Yet, one systematic observation made on fracture surfaces suggests that this statistical fractography may ultimately reveal the basic mechanisms controlling the failure resistance of solids: roughness displays robust scale invariant properties observed through a wide range of seemingly different materials. Even more interesting, fracture surfaces display two separate regimes of scale invariance: at large scales, beyond some material dependent length ξ, the statistics of fracture surfaces observed at one scale can be inferred from the one observed at another scale using a unique scaling exponent, $\zeta \leq 0.5$, also referred to as the roughness exponent. Such a mono-affine regime reveals an anti-persistent response of the crack at the largest scales, a behavior governed by elasticity that tends to maintain the crack trajectory as straight as possible [147, 287, 288] At small scales, below ξ, the statistics of fracture surfaces is radically different: height variations depart from a Gaussian behavior and one single exponent is not sufficient anymore to describe the scale invariant properties. Instead, their complete description requires the introduction of a multi-affine spectrum $\zeta(q) \geq 0.5$ that describes the scaling behavior of the different moments q of the distribution of height variations. This multi-affine regime, investigated in details in Ref. [143] for several materials, reveals that at small scales, cracks follow an apparent persistent trajectory. Such a behavior was conjectured to be reminiscent of damage coalescence.

Here, our first objective is to test such a scenario on experimental data. The fracture surfaces of four rocks are investigated and the crossover length between both roughness regimes is compared with the characteristic size of the damage processes inferred from mechanical tests. To measure ξ, we propose a minimal statistical description of fracture surfaces that circumvents the complexity observed at small scales within the multi-affine regime. It relies on the characterization of the intermittency of the fracture surface, evidenced by the volatility

field associated with the topographic map of the fracture surface. Our approach successfully shows that ξ relates to the process zone size ℓ_c, and thus that the multi-affine properties of fracture surfaces are indeed the signature of damage coalescence. We may also see some exception to thsis general conclusion, for which the short scale damage roughness is dominated by the presence of microstructural features like grains.

Our second objective is to unravel the mechanisms driving the process of damage coalescence at the crack tip vicinity. We propose a methodology that evidences the spatial distribution of microcracks from the statistical treatment of the fracture surface roughness. The size distribution of this microcracks thus obtained is shown to be reminiscent of a dissipation cascade, resembling to some extent to the one observed in turbulent flows. This result sheds light on the cooperative dynamics of microcracks coalescence within the process zone. The relationship between the cascading process evidenced in our work and the crack growth resistance of brittle solids is finally discussed.

5.2 STATISTICAL FRACTOGRAPHY.

We investigate the intermittent properties of the fracture surfaces of four different rocks produced during the research work of *Aligholi et al.* [289]: coarse grain granite, fine grain granite, marble and sandstone. These surfaces are obtained by tensile failure, see [289] for more details. The corresponding height fields $h(\boldsymbol{r})$ are shown in Fig. 5.2, and display overall similarity.

5.2.1 *Multifractal analysis*

A first way to assess the statistical properties of fracture surfaces is to characterize the standard deviation of local jumps $\delta h = h(\boldsymbol{r} + \boldsymbol{\delta r}) - h(\boldsymbol{r})$ at different scales δr. This exactly defines the variogram or *roughness function*, from the following relation:

$$V_2(\boldsymbol{\delta r}) = \langle |h(\boldsymbol{r} + \boldsymbol{\delta r}) - h(\boldsymbol{r})|^2 \rangle. \tag{5.1}$$

Note that, while the variogram is computed for a vectorial increment $\boldsymbol{\delta r}$, it can be further averaged over all angles ($\|\boldsymbol{\delta r}\| = \delta r$), leading to the so-called isotropic variogram $V_2(\delta r)$.

The results shown in Fig. 5.3 indicate that fracture surfaces display fractal scaling, with $V_2 \propto \delta r^{2H}$ where $H = \zeta$ is the Hurst or roughness exponent. This fractal behaviour has been reported for many fracture surfaces, through direct, spectral or wavelet characterizations [144, 145, 279]. The fitted *Hurst* or roughness exponent values are shown in Tab. 5.1. As expected in the literature, the roughness exponent is

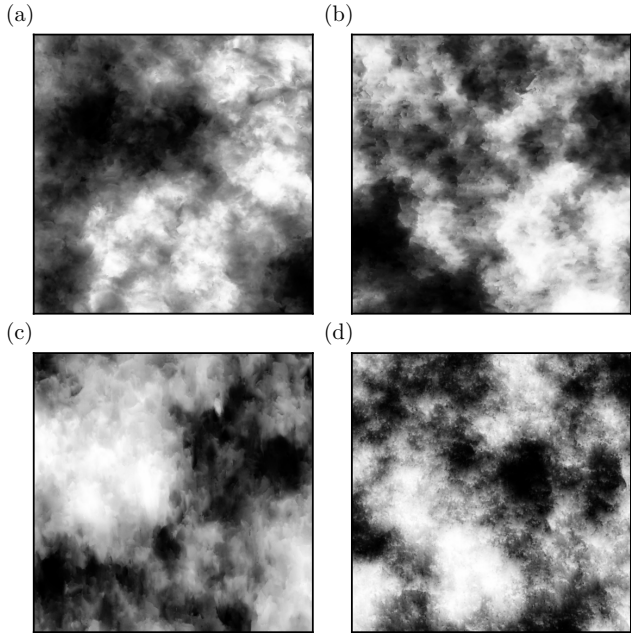

Figure 5.2: Quantile representations of fracture surfaces height field, of size 1000×1000 pixels with 16 μm/pixels. (a) Coarse-grain granite. (b) Fine-grain granite. (c) Marble. (d) Sandstone. The horizontal x-axis and vertical y-axis are respectively orthogonal and parallel to the front propagation direction.

generally higher over the crack front line direction [150, 279]. However, the isotropic exponent constitute good approximations. We recover the commonly observed short-scale persistency ($H > 1/2$) at the exception of the sandstone. For this material, the granular structure results in an inter-granular crack path that might explain such anti-persistent scaling [148, 287].

	CG Granite	FG Granite	Marble	Sandstone
$H_\perp$	0.59	0.58	0.54	0.49
$H_\parallel$	0.58	0.56	0.62	0.49
H	0.57	0.55	0.56	0.46

Table 5.1: Roughness exponents $H = \zeta_2/2$, computed along the propagation direction $(H_\perp)$, crack front direction $(H_\parallel)$, and isotropically (H) over the surface.

Jump distribution and fat-tail statistics – Fracture surfaces are also known to display multifractality at small scale, as reported in [143, 276, 290]. In particular, the probability density functions (p.d.f) $\rho_\epsilon(\delta h) = \mathbb{P}(h(\boldsymbol{r}+\boldsymbol{\epsilon}) - h(\boldsymbol{r}))$ has been reported to be fat-tailed for $\epsilon < \xi$, and Gaussian for $\epsilon > \xi$, where ξ defines a crossover length between intermittent and Gaussian statistics. In Fig 5.4, we compute these empirical p.d.fs, for various values of ϵ. For low ϵ, one observes robust fat tail

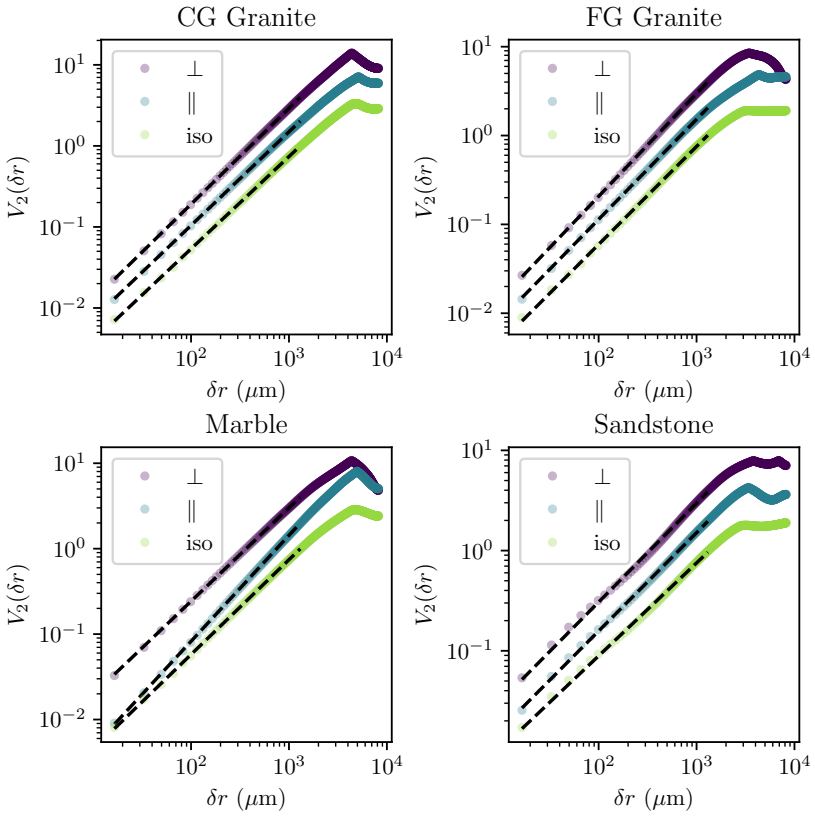

Figure 5.3: Order 2 variograms computed for the different materials. The variograms are computed along the crack propagation direction (⊥), front direction (∥), and isotropically. Black dotted lines correspond to power-law fits, values are reported in Tab. 5.1

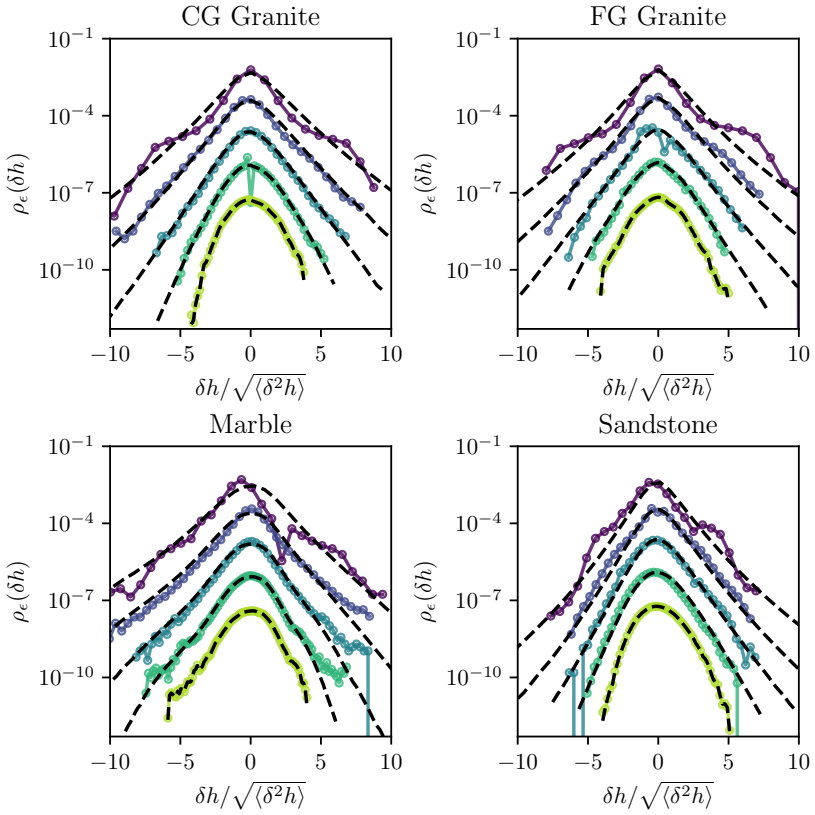

Figure 5.4: Probability density functions of jumps, computed perpendicularly to the propagation direction. Each curve corresponds to different values of $\epsilon = 33, 66, 132, 264, 528$ μm (top to bottom) that have been rescaled for visibility. The black curves correspond to the predictions inferred from the Castaing equation [153] (see Chap. 4 for more details) under log-normal cascade assumption, using the Castaing equation introduced in Ch. 4.

statistics, that can not originate from metrological limitations alone, as the spatial resolution $\delta r_{\text{resolution}} \approx 10\mu$m is lower than the pixel size $\delta r_{\text{pixel}} \approx 16.5\mu$m. The p.d.fs ultimately reach Gaussian statistics as ϵ increases. We will explain later the theoretical curves reported in black dotted lines.

Multiscaling of jumps– We go one step further into the statistical description of these surfaces, by characterizing their multifractal behaviour using the generalized variograms, defined as:

$$V_q(\boldsymbol{\delta r}) = \langle |h(\boldsymbol{r} + \boldsymbol{\delta r}) - h(\boldsymbol{r})|^q \rangle. \tag{5.2}$$

These functions generalize the variance measure used in (5.1) by measuring the different moments of the jumps, and their dependence on the scale δr. These functions are naturally predictable in the case of Gaussian statistics, as the Wick theorem ensures $V_{2m} \propto (V_2)^m$, and one would expect a collapse of the rescaled variograms $(V_q)^{1/q}$. We compute these functions in Fig. 5.5 and observe a collapse of the

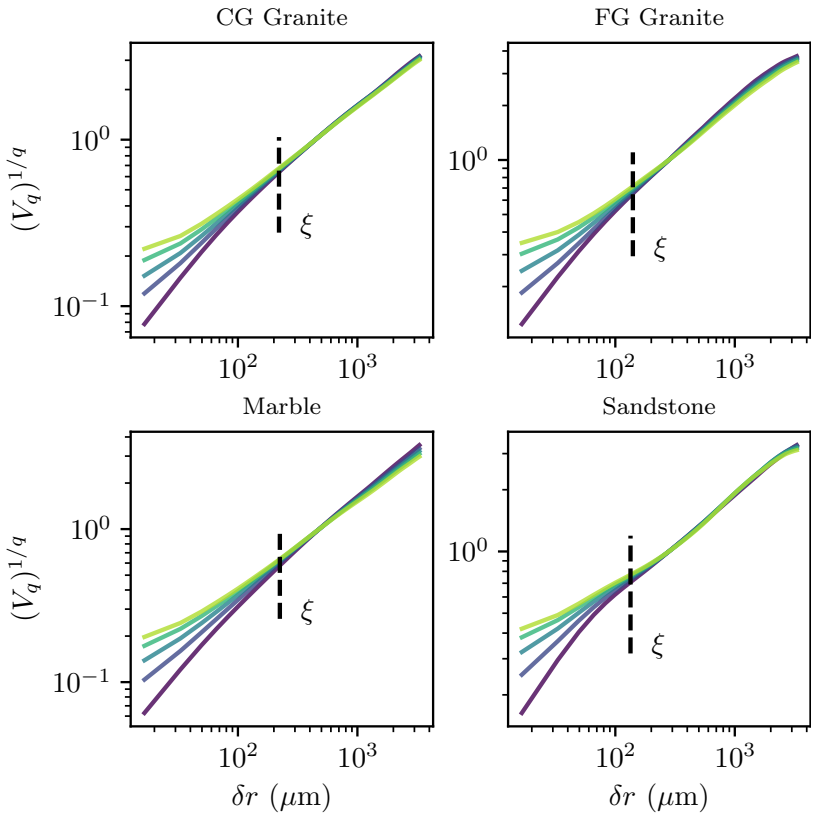

Figure 5.5: Rescaled generalized variograms $(V_q)^{1/q}$computed for the different surfaces, with $q \in \{1,2,3,4,5\}$ corresponding to bottom to top curves. The values of ξ correspond to the fitting parameter of Fig. 5.8.

rescaled variograms for $\delta r > \xi$, as reported in Chap. 4 for a metallic alloy. On the contrary, the $\delta r < \xi$ regime deviates from monofractal scaling. Here, we do not seek to characterize further the multi-affine properties as the range of length scale $\delta r < \xi$ over which intermittency is observed is rather limited. Note however that under the same assumptions of Chap. 4, a convenient prediction of the probability densities can be made in Fig. 5.4, using the Castaing equation under log-normal fluctuation ratio rule.

Volatility correlations – The previous characterizations described the self-similarity and non-Gaussianity of the surfaces. We now focus on the log-volatility field ω, that contains complementary information. Following the unwrapping technique developed in Chap. 4, we define the ω field from the fractional differentiation operation:

$$\hat{\omega}(\boldsymbol{r}) = \log|(-\Delta)^{\frac{H+d/2}{2}} h(\boldsymbol{r})|, \tag{5.3}$$

which discards the roughness cascade and highlights localized intermittent bursts. The corresponding fields are computed using the isotropic roughness exponent H reported in Tab. 5.1 , and shown in Fig. 5.6. These fields display correlated structures, which however

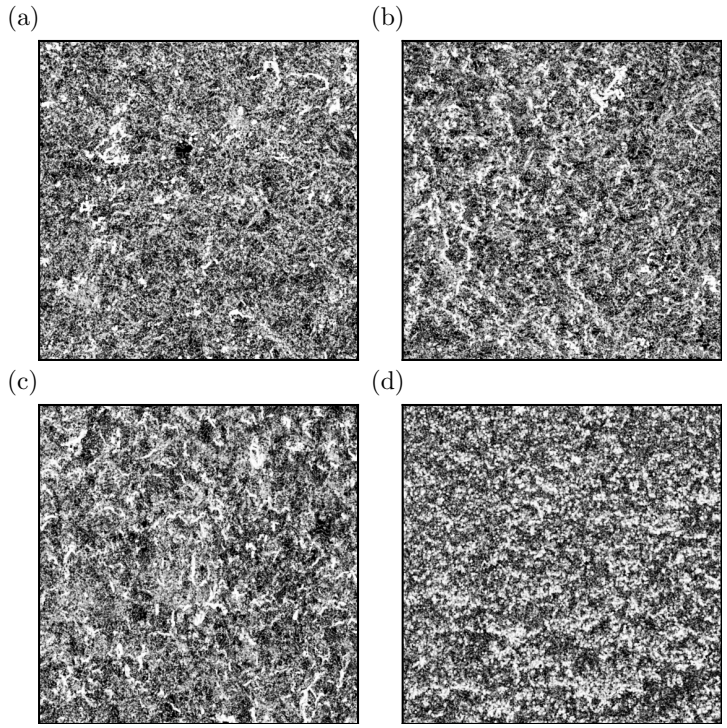

Figure 5.6: Quantile representations of the log-volatility field ω, obtained from fractional differentiation of the height using Eq. (5.3) for (a) coarse-grain granite, (b) fine-grain granite.,(c) marble and (d) sandstone. The image size 16.5×16.5 cm^2 is identical to the one of the height fields of Fig. 5.2.

seem to vary from one rock to the other. The first three surfaces display anisotropic and filamental structures (however smaller than the one observed on the fracture aluminium surface of Chap. 4), while the last one displays more compact structures.

To characterize these patterns quantitatively, we run a correlation analysis, and recover a strongly correlated short range regime, reported in Fig. 5.7. This regime, that decays faster than the logarithmically correlated regimes encountered previously, can be described by a power-law fits of the following form,

$$C_\omega(\delta r) = \lambda_{\rm pl}\delta r^{-\gamma} + C^\infty_{\rm pl}, \tag{5.4}$$

where $C^\infty_{\rm pl}$ accounts for residual correlations due to the asymmetrical statistics of ω, and $\lambda_{\rm pl}$ is an analogue of the intermittency coefficient recovered for logarithmic correlations. We recover satisfying fits, which is further confirmed by the collapse of curves in the inset of Fig. 5.7. The values of $C^\infty_{\rm pl}$ are found to be very small.

While the power-law spatial correlations of the volatility field at small scale is compatible with the multi-scaling behavior observed in Fig. 5.5 from the variograms, this power law does not provide any clue about the cutoff length ξ of this multi-affine regime. We

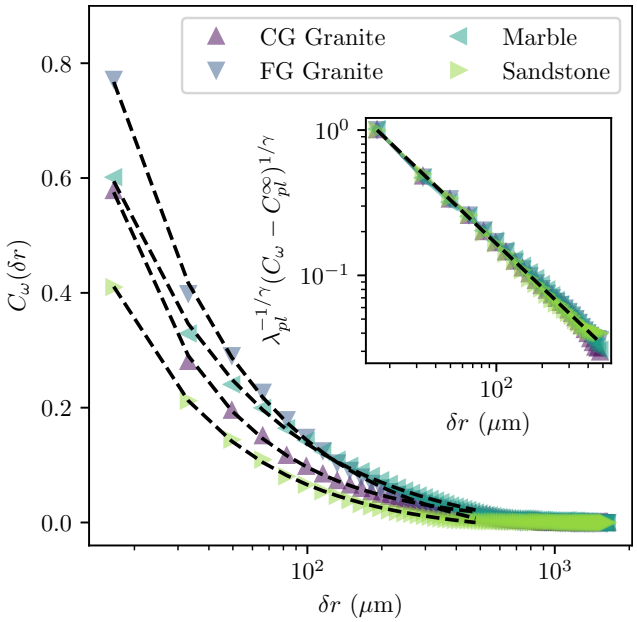

Figure 5.7: Correlation analysis of ω. (Main figure) Isotropic correlation functions of ω, fitted by power-law functions (black dotted lines). Values are reported in Tab. 5.2. (Inset) Collapse of correlation functions around the power-law model.

circumvent this difficulty by fitting the correlations for higher lags with an exponential function,

$$C_\omega(\delta r) = \lambda_{\text{exp}} \exp(-\delta r/\xi) + C^\infty_{\text{exp}}, \tag{5.5}$$

where λ_{exp} is another quantity analogous to the intermittency coefficient λ as defined in the MRW model (see Chap. 4), C^∞_{exp} accounts for the skewness of ω. As shown in Fig. 5.8, the exponential fit provides a rather accurate description of the correlations of the correlations of ω in the range $200\mu\text{m} < \delta r < 1\text{mm}$, an observation further confirmed in the semi-logarithmic representation in inset. This defines the cut-off length ξ of the multi)affine regime, the values of which are reported in Tab. 5.2. We find that the correlation length ξ is about 10–15 times the map resolution, which is two times smaller than for the aluminum alloy, explaining our first visual assessment. Again here, the values of C^∞_{exp} are found to be very small.

5.2.2 *Cluster analysis*

The previous analysis revealed the strong correlations of the volatility field, which ultimately vanish beyond ξ.

We now seek to characterize the topology of the most intermittent regions of the volatility field by running a cluster analysis. In Fig. 5.9, we reveal these clusters by thresholding the ω field by keeping only

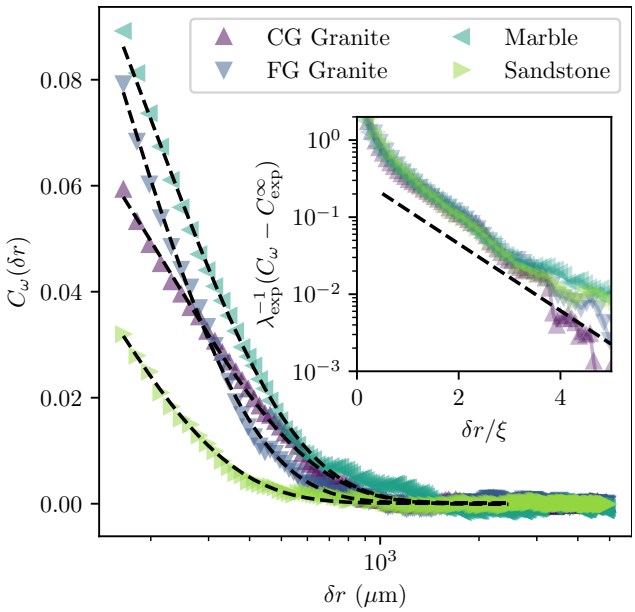

Figure 5.8: Correlation analysis of ω. (Main figure) Isotropic correlation functions of ω, fitted by an exponential decay (black dotted lines). Values of the cut-off length ξ of the multi-affine regime are reported in Tab. 5.2. (Inset) Collapse of the correlation functions around the exponential model in a semi-logarithmic representation.

	CG Granite	FG Granite	Marble	Sandstone
Power-law fits				
λ_{pl}	.58	0.81	0.63	0.43
γ	0.98 ± 0.01	0.81 ± 0.01	0.73 ± 0.02	0.89 ± 0.01
Exponential fits				
ξ (μm)	227	146	202	126
λ_{exp}	0.12	0.24	0.19	0.12

Table 5.2: Fitting parameters for the correlation functions of ω, shown in Fig. 5.7 and Fig. 5.8.

the $(1 - p_c) = 10\%$ highest values. We immediately observe the difference between the first three surfaces – which display filamental shapes– and the last one (sandstone) which displays compact small clusters. Here, we proceed to a more quantitative analysis on the fractal dimension, anisotropy and distribution of these clusters.

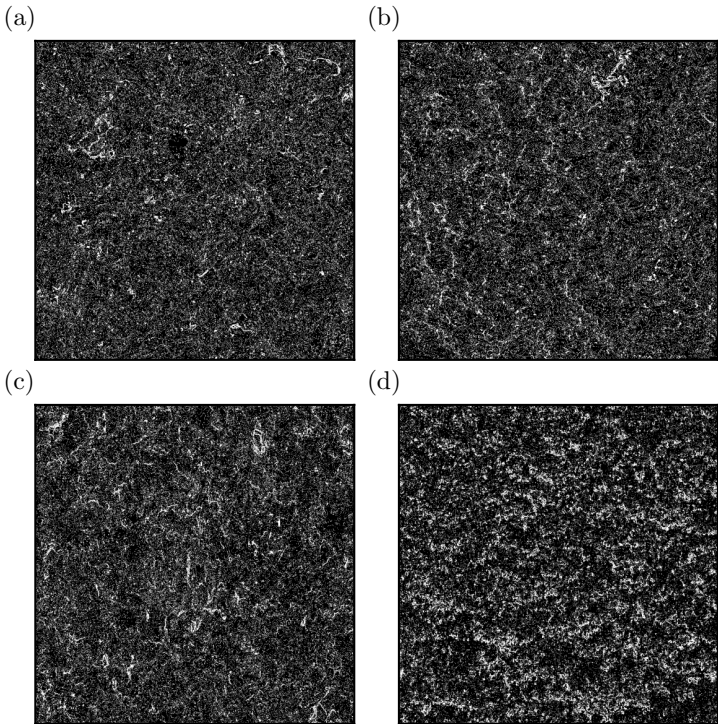

Figure 5.9: Binarized ω fields ($p_c = 90\%$), obtained from Fig. 5.6

Fractal dimensions analysis – Similarly to Chap. 4, we study the relationship between the spatial extension and the surface S of each cluster. The spatial extension is defined here as the radius R_g of the circle that fits the cluster. In practice, we use the definition $R_g^2 = \lambda_\parallel^2 + \lambda_\perp^2$ where $\lambda_\parallel$ and $\lambda_\perp$ are the largest and smallest eigenvalues of the gyration tensor T_g of the cluster, respectively. The results are reported in Fig. 5.10. We observe a fractal behaviour of clusters, with an overall fractal dimension $D = 1.63 \pm 0.05$, in agreement with previously reported results [143].

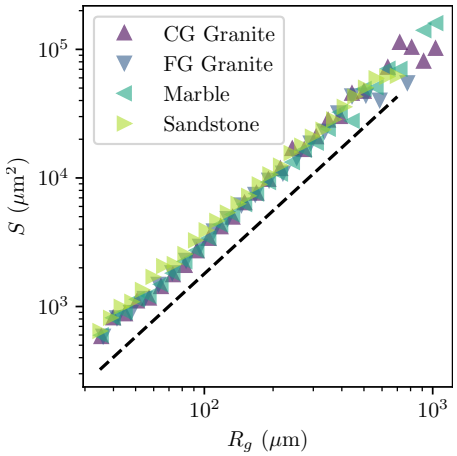

Figure 5.10: Fractal dimension analysis of clusters ($p_c = 90\%$) The fitting curve corresponds to $S = R_g^D$ with $D = 1.63$.

Anisotropy analysis – We observed in Chap. 4 that synthetic and experimental ω fields displayed different topologies in the distribution of clusters, as experimental clusters display stronger anisotropy. We repeat here the same procedure, by looking at the ratio $r = \lambda_\perp / \lambda_\parallel$, which ranges from 0 to 1. Low values correspond to filamental clusters, while high values correspond to disk shaped clusters. We observe in Fig. 5.11 a clear distinction between the first three surfaces and the sandstone surface. This last one displays more isotropic clusters, and almost no filamental structure, as observed qualitatively in Fig. 5.9.

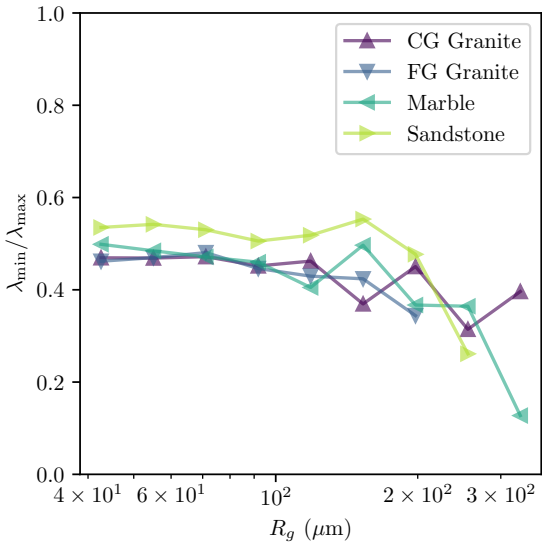

Figure 5.11: Anisotropy analysis of clusters ($p_c = 90\%$)

Distribution of cluster sizes – The clusters forming by the most intermittent events of the fracture surfaces have been shown in [143] to follow a power-law distribution $P(R_g) \propto R_g^{-\tau}$, with $\tau \approx 2.2$.

The analysis of the four rocks shows a similar behaviour, that clearly appears for low p_c values as is shown in Fig. 5.12.

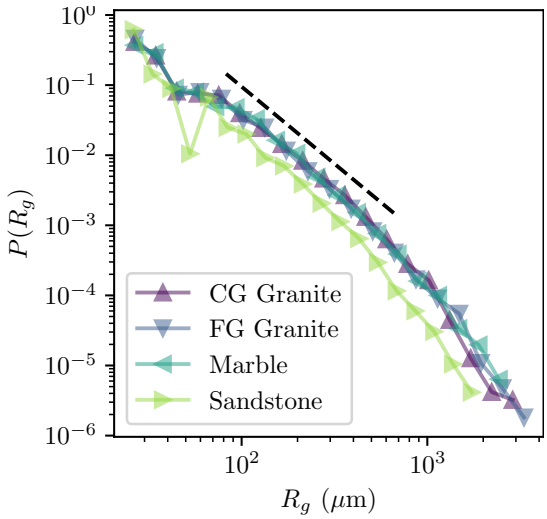

Figure 5.12: Probability distribution of cluster size ($p_c = 70\%$). The black dotted curve corresponds to a power-law with slope $\tau = 2.2$

However, as one increases p_c to conserve only the most intermittent events, the distributions deviate from one another,. This is well visible in Fig. 5.13 that shows the cumulative distribution function of clusters $F_>(R_g) = \sum_{r=0}^{R_g} P(r)$. On top of it, the cluster size distribution displays an exponential cut-off.

Normalizing the horizontal axis by the cut-off length measured in Fig. 5.8 from the correlations of the ω-fields, we observe a collapse of these different distributions in the regime $R_g > \xi$. This implies that the size of the largest clusters is set by the cut-off length of the multi-affine regime, defining a single characteristic length ξ of the intermittent regime. We note however the exceptional case of sandstone, for which the collapse length corresponds to $\xi/2$. We expect this discrepancy to originate from the grains of the material, that ultimately controls the cluster geometry, rather than the process of damage coalescence.

We now seek to provide a physical interpretation to the multiaffine length scale ξ.

5.2.3 *Physical interpretation of the cut-off length ξ*

We now compare the results of the fractographic analysis with the mechanical properties of materials, measured in [289] and reported in Tab. 5.3.

As discussed earlier, at small scale, failure proceeds through the coalescence of damage cavities. This damage is localized at the crack

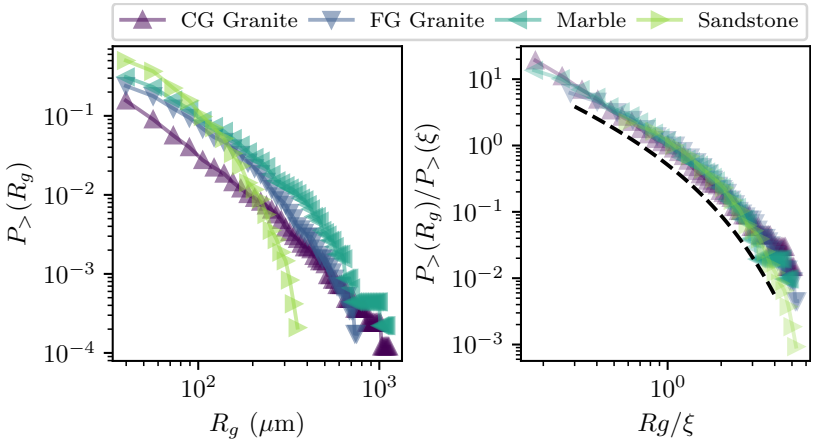

Figure 5.13: Cumulative distribution function of Cluster size ($p_c = 97\%$). On the right, the distributions are collapsed using the values of ξ(values reported in Tab. 5.2). The black curve is a truncated power law of the form $f(u) = u^{-\tau+1}e^{-u}$, with $\tau = 2.2$ and rescaled for visibility.

tip, in a region of size ℓ_c. The fracture process zone size ℓ_c can be assessed using the Dugdale–Barenblatt (D–B) formula [291]

$$\ell_c = \frac{\pi}{8}\left(\frac{K_c}{\sigma_c}\right)^2, \tag{5.6}$$

where K_c is the material fracture toughness and σ_c is its cohesive strength. When comparing ℓ_c with ξ in Tab. 5.3, one observes a linear relation $\ell_c = \alpha\xi$ where $\alpha \approx 5$, hence indicating that the multi-affine length scale ξ is set by the damage process zone size ℓ_c linking fractographic and mechanical properties.

This also supports the conjecture made by Vernède et al. [143] that multifractality is reminiscent of damage coalescence processes, both phenomena being observed on the same range of length scales $\delta r < \xi \sim \ell_c$.

The only exception is of the sandstone, whose process zone size is much higher than 5ξ. This discrepancy may be explained by two main factors: (i) sandstone possesses a grain-like structure with a characteristic size $\ell_{grain} \approx 100$ μm close to ξ value, (ii) sandstone displays a high level of porosity compared to the other rocks, see Tab. 5.3. Overall, this implies that crack growth in sandstone is mainly intergranular. And thus that the morphology of fractured sandstone surfaces is mainly governed by its inter-granular structure, especially at small scales $\delta r \leq \xi \approx 100$ μm where multifractality is observed.

This intuition is further confirmed by our fractographic analysis which emphasized the different topologies of the most intermittent bursts. For coarse-grain, fine-grain granite and marble, these bursts display filamental structures, as they were formed by the merging of several microcracks, while for the sandstone, clusters are more com-

	CG Granite	FG Granite	Marble	Sandstone
Roughness analysis				
ξ (μm)	227 ± 4	146 ± 4	202 ± 3	126 ± 3
Mechanical analysis				
σ_c (MPa)	20	24	15	8.4
K_c (MPa$\sqrt{m}$)	0.97	1.00	0.76	0.43
E (GPa)	45	55	55	18
G_c (J/m^2)	19	17	8.3	9.0
ℓ_c (μm)	1080	800	1180	1200
ℓ_{grain}	$\approx$ 1mm	$\approx$ 500 μm	$\approx$ 1 mm	$\approx$ 100 μm
ρ_p	$< 1\%$	$< 1\%$	$< 1\%$	$5 - 10\%$
ℓ_c/ξ	$4.75 \pm .05$	$5.5 \pm .2$	$5.8 \pm .1$	$9.5 \pm .2$

Table 5.3: Summary of the statistical analysis of the fracture surfaces and the mechanical properties measured by Aligholi *et al.* [289] for the four rocks investigated. The ration ℓ_c/ξ shows an almost constant value except for the sandstone, suggesting in the granites and marble, multifractality results from the coalescence process taking place within the process zone of size ℓ_c.

pact, as they were formed by the pores present in its microstructure.

Overall, we showed that multi-affinity is closely related to the damage coalescence process driving crack growth at small scale. In the following section, we embrace this phenomenology and propose models of failure base on damage coalescence mechanisms.

5.3 CRACK GROWTH MODELS

In the following section, we propose two simple models of crack growth based on the coalescence mechanisms revealed in the previous section. Our objective is to understand better how multifractality emerges from damage coalescence processes.

In a first model, we build on the discrete statistics of crack jumps, and we model the front displacement from a Continuous Time Random Walk that retrieves the superdiffusivity of crack paths at short scale.

In a second model, we adopt a continuous growth approach, with correlated velocity fluctuations, by assuming that these correlations result from damage coalescence. These correlations encode an effective behaviour of the complex dynamics taking place within the fracture process zone, and lead to a transition from superdiffusive multiaffinity to diffusive monofractality, classically observed on experimental fracture statistics.

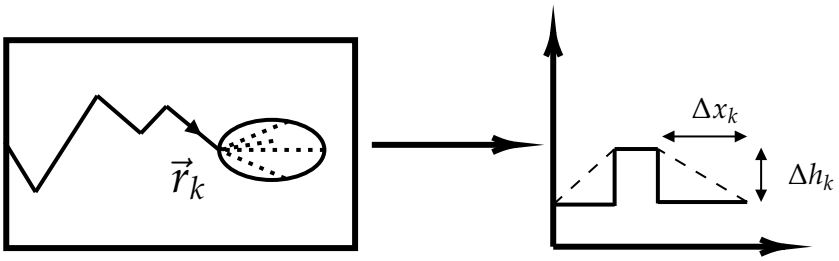

Figure 5.14: Continuous Time Random Walk Description of the crack propagation. (Left) The crack tip advances by sampling micro-cracks in the Fracture Process Zone (FPZ).(Right) The dynamics is modelled as the sampling of forward and out-of-direction jumps, whose statistics are given by Eq. (5.12).

5.3.1 *Discrete model with fat-tail statistics*

Our previous cluster revealed that cracks propagate through jumps that are power-law distributed up to a cutoff ξ. Here, the underlying assumption is that the size R_g of the clusters (i.e. the damage cavities) provide the jump length expected from a dynamical damage coalescence process. We build a $(1+1)d$ discrete jump description from the Continuous Time Random Walk model that retrieves the transition from non-Gaussian to Gaussian statistics of crack path increments. The approach adopted here belong to the realm of Quantized Fracture Mechanics, that accounts for the discrete nature of crack growth process [292, 293] .

Jumps statistics – The crack front is described by its horizontal and vertical coordinates (x_k, h_k), where k indexes singular crack events, see Fig. 5.14. We expect the jumps distributions to display a power-law shape with an upper cutoff . Here, we choose truncated levy $(\alpha-1)$-stable distributions [270, 294, 295], defined in the following:

$$\begin{cases} \psi(\Delta x) \propto & L_{\alpha-1}(\Delta x)\mathbf{1}_{\Delta x<\ell_x} \\ \Lambda(\Delta h) \propto & L_{\alpha-1}(\Delta h)\mathbf{1}_{|\Delta h|<\ell_h} \end{cases}, \tag{5.7}$$

where $L_{\alpha-1}$ is a Lévy-stable distribution [29, 296] that possesses power-law tails of exponent α, $\mathbf{1}$ designates the indicator function and (ℓ_x, ℓ_h) are the cut-off lengths. The probability density $\Lambda(\Delta h)$ is symmetric around $\langle \Delta h \rangle = 0$, while $psi(\Delta x)$ is completely skewed to prevent backpropagation.

Continuous Time Random Walk (CTRW) description – At given index k, the crack tip position results from the sum of all previous jumps starting from the initial position $(0,0)$, with $x_k = \sum_{i=1}^{k} \Delta_i x$ and $h_k = \sum_{i=1}^{k} \Delta_i h$ (see Fig. 5.14). This allows us to derive a CTRW [297] description of trajectories, where x plays the role of time. Similarly

to [298], we derive the balance equation for the density of crack path $\phi(x,h)$:

$$\phi(x,h) = \Psi_>(x)\phi(h,0) + \int\int_{[0,x]} dh'dx'\psi(h-h')\Lambda(x-x')\phi(h',x'), \tag{5.8}$$

where the first term of the RHS is defined by

$$\Psi_>(x') = \mathcal{P}(\Delta x > x') = \int_{[x;+\infty]} dx'\psi(x'), \tag{5.9}$$

and is the probability that the particle did not move and started at convenient initial positions with probability $\phi(h,0) = \delta(h-h_0)$. A Fourier-Laplace transform of Eq.(5.8) yields

$$\phi(p,k) = \frac{1-\psi(p)}{p}\phi_0(k) + \psi(p)\Lambda(k)\phi(p,k), \tag{5.10}$$

which recovers the so-called Montroll-Weiss equation [299]:

$$\phi(p,k) = \frac{1-\psi(p)}{p}\frac{1}{1-\psi(p)\Lambda(k)}, \tag{5.11}$$

where each of the transformations are related to the respective characteristic functions of jumps through $\psi(p) = \phi_{\Delta x}(ip)$ and $\Lambda(k) = \phi_{\Delta h}(k)$.

Asymptotic scaling and fractional diffusion equation – To understand the scaling of trajectories, we study the asymptotic scaling regime of Eq. (5.11) for $k, p \ll 1$ (continuous limit). The positive support of $\psi(\Delta x)$ immediately yields $\psi(p) \approx 1 - \langle \Delta x \rangle p$, without contributions of the fat-tail statistics of $\langle x \rangle$. For $\Lambda(k)$ however, the symmetry of the distribution cancels the first order term $\langle h \rangle = 0$ and yields two scaling regimes:

$$1 - \Lambda(k) \approx \begin{cases} Ck^{\alpha-1} & \text{for } \ell_h^{-1} \ll k \ll 1 \\ \langle \frac{\Delta h^2}{2} \rangle k^2 & \text{for } k \ll \ell_h^{-1} < 1 \end{cases}. \tag{5.12}$$

Injecting these scalings in Eq. (5.11) under continuous limit leads to:

$$\phi(k,p) \approx \begin{cases} \left[p + \frac{C}{\langle x \rangle}k^{\alpha-1}\right]^{-1}, & \ell_h^{-1} \ll k \ll 1, \quad p \ll 1 \\ \left[p + \frac{\langle h^2 \rangle}{2\langle x \rangle}k^2\right]^{-1}, & k \ll \ell_h^{-1} < 1, \quad p \ll 1 \end{cases}. \tag{5.13}$$

We recognize in the second case the Fourier-Laplace Transform of the Gaussian distribution $\phi(x,h) \propto \exp(-\frac{(h-h_0)^2}{4Dx})$ ($D = \langle \Delta h^2 \rangle / \langle \Delta x \rangle$) which solves the classic diffusion equation:

$$\frac{\partial p(x,h)}{\partial x} = D\frac{\partial^2 p(x,h)}{\partial h^2} + \delta(h)\delta(x) \tag{5.14}$$

In the fat-tail regime, the scaling corresponds to the solution of a fractional diffusion equation [300], where the second derivative term is replaced by a fractional Laplacian operator.

From superdiffusive Lévy flight to diffusive Gaussian statistics – Now, the question left is the existence of a crossover scale between non-Gaussian and Gaussian statistics. The specific case of constant jumps along x and truncated $(\alpha-1)$-Lévy-stable jumps along h was studied in [294]. In that situation, the authors highlighted the existence of a crossover scale $\xi = A\ell_h^{\alpha-1}\ell_x$ where

$$A = \left[\frac{\pi(\alpha-1)}{2\Gamma(1/(\alpha-1))[\Gamma(\alpha)\sin(\pi(\alpha-1)/2)/(3-\alpha)]^{1/2}}\right]^{2(\alpha-1)/(\alpha-3)}. \tag{5.15}$$

That length separates a Lévy-flight superdiffusive regime and a Gaussian one both characterized by their variogram $V_q(\delta x) = \langle h(x+\delta x) - h(x)\rangle$ such that,

$$\begin{cases} V_q(\delta x) \propto \delta x^{\zeta_q} & , \delta x \ll \xi \\ V_q(\delta x) \propto \delta x^{q/2} & , \delta x \gg \xi \end{cases}, \tag{5.16}$$

where the short scale multifractal spectrum behaves as

$$\zeta_q = \begin{cases} \frac{q}{\alpha-1}, & q < \alpha-1 \\ 1, & q > \alpha-1 \end{cases}, \tag{5.17}$$

We implement the numerical scheme experiment of [294] in Fig. 5.15 and observe multifractal scaling, that survives up to ξ. The overall shape of the generalized Hurst exponent spectrum H_q – predicted in [295] – is very reminiscent of the one observed in the discrete simulations of non-linear surface growth under power-law distributed noise [56, 301].

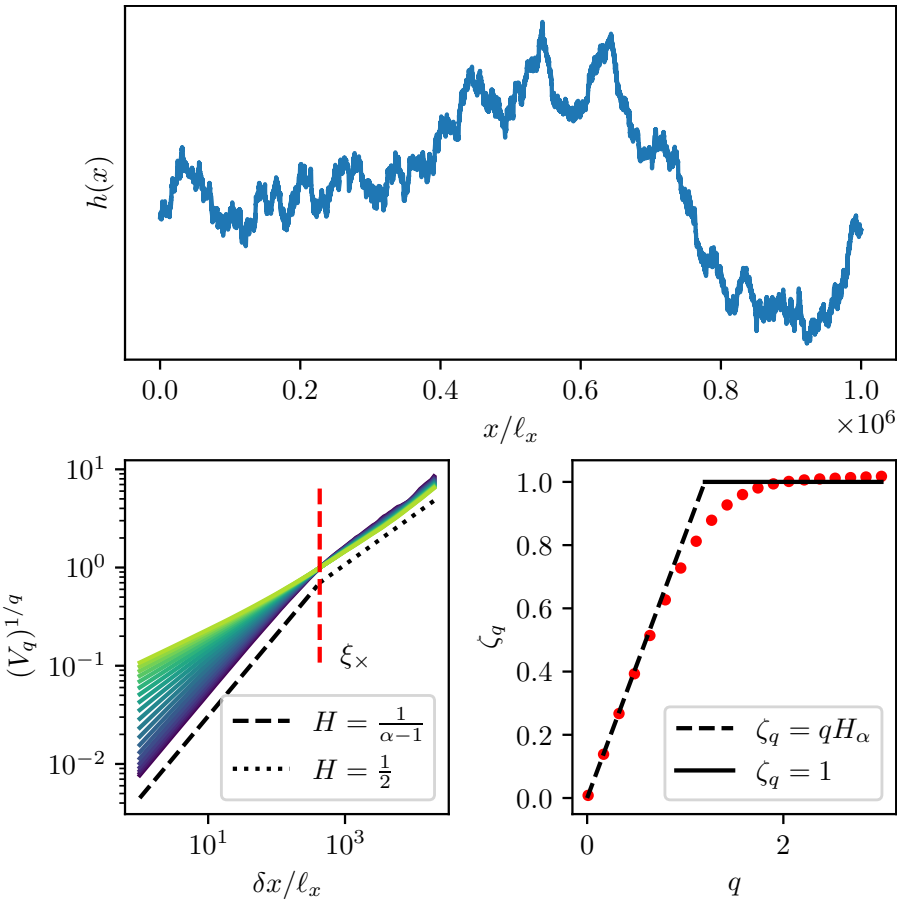

Figure 5.15: Multifractal analysis of truncated Lévy-flights, for $\ell_x = 1$, $\ell_h = 300$ and $\alpha = 2.2$. (Left) Variogram analysis, with theoretical slope of exponent $H_\alpha = 1/(\alpha - 1) = .83$, and diffusive limit $H = 1/2$. Darker colors correspond to low q values, and lighter colors to high q values. (Right) Generalized scaling exponent spectrum ζ_q, with theoretical expectations from Eq. 5.17.

Comparison with experimental results – The superdiffusive scaling described above exclusively appears for $q < \alpha - 1$. For $q = 2$, we systematically observe diffusive scaling ($H = .5$). Our predictions are compared with the scaling properties of experimental fracture surfaces [292, 302–305] in Tab. 5.4. We use the value of α to predict the roughness exponent $H_{alpha} = 1/(\alpha - 1)$. The predicted roughness exponent is then compared to its experimental value in Tab. 5.4. We find that H_α larger than $1/2$, in agreement with experiments, but systematically overestimates the experimental value. Note that our model does not predict physical values when $\alpha < 2$, as reported in paper sheets fracture, for example.

We also observe the similarity between our model and experimental surfaces, regarding the multifractal scaling observed at small scale $\delta x < \xi$, and the sharp transition towards monofractal scaling when $\delta x > \xi$. We note however that the multifractal scaling of our model

	Experimental		Predicted
	α	H	$H_\alpha = \frac{1}{\alpha-1}$
Rapid failure (metals, 3D)	$2.2 \pm .1$ [143]	$0.75 \pm .03$ [279]	$0.83 \pm .06$
Fatigue failure (metals, 3D) [302]	2.	0.55 [305]	≈ 1
Rapid failure (rocks, 3D)	$2.2 \pm .1$ [292]	$0.57 \pm .06$ (Fig. 5.3)	$0.83 \pm .06$
Subcritical crack (paper, 2D) [306]	$1.3 \pm .1$	$0.71 \pm .01$ [304]	-

Table 5.4: Comparison of the theoretical roughness exponent H_α inferred from the experimental crack jump distribution exponent α with the experimental roughness H for different materials, failure modes and sample dimensions.

is only apparent, and does not originate from volatility correlations resulting from collective effects. This *apparent multifractality* [270] is here mainly due to the presence of rare events which slow down the convergence of the Central Limit Theorem (CLT).

5.3.2 *A continuous model with correlated fluctuations*

We now adopt a continuous viewpoint to model crack growth, we describe the crack front by its position $\boldsymbol{r}(t) = (x(t), h(t))$ in the $(0x, 0y)$ plane, x and h describing in-plane and out-of-plane positions respectively (see Fig. 5.14 for the definition of the axis). We know –from experimental observations– that crack velocities strongly fluctuate, while displaying time correlations. We assume the crack velocities $(\dot{x}, \dot{h})$ to display the following correlations:

$$\begin{cases} \langle \dot{x}_t \dot{x}_{t'} \rangle - \langle \dot{x}_t \rangle^2 \propto |t - t'|^{-\gamma_x} e^{|t-t'|/\tau_x} \\ \langle \dot{h}_t \dot{h}_{t'} \rangle \propto |t - t'|^{-\gamma_h} e^{|t-t'|/\tau_h} \end{cases}, \tag{5.18}$$

where $v_0 = \langle \dot{x}_t \rangle$ is the average crack speed. Note that a characteristic length $\xi = \tau_x v_0$ naturally emerges from such description, and provides the correlation length of crack trajectories.

An important constraint is that $\dot{x}(t) \geq 0$, in order to prevent the backpropagation of the crack. We also impose the trajectory to be ballistic and one must recover $\langle x(t) - x(t') \rangle = v_0 |t - t'|$. Under these conditions of strict monotonicity, any realized trajectory $(x(t))_{0<t<T}$ can be reversed into a time trajectory indexed by x, written as $(f_t(x))_{x(0)<x<x(T)}$ such that $f_t(x(t)) = t$ for all t. Our first objective is to express the stochastic properties of the crack profile $h(f_t(x))$ by eliminating the dependency in time. Let us recall –for intuition – that the composition of a stochastic process with a strictly increasing measure is a common way to define multifractal processes [307, 308]. We now study some specific cases in which the properties of such trajectory can be analytically tractable.

First model: Superdiffusive to diffusive trajectories – For out-of-plane fluctuations $\dot{h}(t)$, a first reasonable assumption of this continuous framework is to assume Gaussian statistics, resulting from multiple contributions of the out-of-plane fluctuations. Its statistics are then summed up by its null average $\dot{h} = 0$ and its correlations, defined in Eq. (5.18). For in-plane fluctuations $\dot{x}(t)$, we assume the standard deviation to be negligible in front of v_0, leading to a deterministic speed $\dot{x}(t) \approx v_0$ corresponding to a time-trajectory of the form $\dot{f}_t(x) = x/v_0$. The resulting process has Gaussian increments and possesses two monofractal persistent and diffusive regimes, scaling as $V_q(\delta x) = \langle |h(x+\delta x) - h(x)|^q \rangle \propto \delta x^{qH}$ where the Hurst exponent verifies

$$\begin{cases} H = 1 - \frac{\gamma_h}{2}, & \delta x \ll v_0 \tau_h \\ H = \frac{1}{2}, & \delta x \gg v_0 \tau_h \end{cases}, \tag{5.19}$$

We now increase the standard deviation value of $\dot{x}(t)$, and observe the influence on resulting crack profiles.

Second model: Log-normal growth and multifractal scaling – We know that the growth of surfaces is intermittent and sample power-law distributed in-plane jumps. Yet, we expect that a sufficient coarse-graining can allow for continuous approximations. In Ref. [309], the coarse-graining of in-plane fluctuations seems to reproduce statistics similar to log-normal distributions. We also know from the literature that a simple way to build a (i) self-similar, (ii) ballistic and (iii) strictly increasing measure is to use log-normal fluctuations with power-law correlations [255, 307]. Hence, we assume in the following that in-plane fluctuations are log-normal, and correlated according to Eq. (5.18). The resulting trajectory $x(t)$ defines a proper multifractal random measure, and we study whether this is also the case for $f_t(x)$. We know, from derivative rules of inverse functions that : $\dot{x}(t)\dot{f}_t(x(t)) = 1$, which becomes $\dot{f}_t(x) = 1/\dot{x}(f_t(x))$ and implies log-normality of $\dot{f}_t$. We get the correlations of $\dot{f}_t$ from the following computation:

$$\langle \dot{f}_t(x)\dot{f}_t(x') \rangle = \langle \frac{1}{\dot{x}(t = f_t(x))} \frac{1}{\dot{x}(t' = f_t(x'))} \rangle, \tag{5.20}$$

which, from the properties of log-normal distributions, leads to:

$$\langle \dot{f}_t(x)\dot{f}_t(x') \rangle \propto \begin{cases} \left| \frac{x-x'}{v_0\tau_x} \right|^{-\lambda} & |x-x'| \ll v_0\tau_x \\ 1 & |x-x'| \gg v_0\tau_x \end{cases}, \tag{5.21}$$

In the end, the crack trajectory can be described by $y(x) = h(f_t(x))$ which exactly defines a Brownian process subjected to a log-normal cascade "time"-change, and consequently defines a Multifractal Random Walk (MRW) [255]. In the case $\tau_x = \tau_h = \tau$, one introduced

$\xi = v_0.\tau$ and recovers a non-linear scaling exponent spectrum ζ_q, verifying:

$$\zeta_q = \begin{cases} q(1-\frac{\gamma_h}{2}) - \frac{\gamma_x}{2}q(q-1), & \delta x \ll \xi \\ q/2, & \delta x \gg \xi \end{cases} . \tag{5.22}$$

Comparison with experimental data – We now confront the predictions of these two continuous models with the experimental data found in the literature.

The difficulty of tracking the velocity of crack fluctuations in real time explains the scarcity of such data in the literature. In a work from Tallakstad *et al.* [309], the local dynamics of a crack front is studied. In particular, the velocity fluctuations were found to follow truncated power-laws, with exponent $\tilde{\gamma} = 0.46$. Assuming similar correlations over $(0x)$ and $(0y)$, the first model recovers $H = 1 - \tilde{\gamma}/2 \approx 0.78$, close to the roughness exponent of metals and paper reported in Tab 5.4. We also note that relaxing the Gaussian property of jumps would leave invariant this exponent for $q = 2$.

For the second model, we showed that the presence of correlations for in-plane fluctuations were responsible for the multifractal trajectory of coefficient $\lambda = \gamma_x$, under the same assumptions, one recovers $\lambda \approx 0.43$, significantly higher than the usual range $0 < \lambda < 0.2$ [143, 152]. We expect this prediction to be bounded by the log-normal assumption of velocity fluctuations over $(0x)$, an hypothesis which would deserve further investigations.

5.4 CONCLUSION

In this chapter, we have studied four different fracture surfaces, obtained from four different types of rocks. We systematically found multifractal properties, following the different characterizations introduced in Chap 4. It appeared that the range ξ of the multifractal regime was material-dependent. Using the mechanical properties of the rocks, we show that ξ is set by the spatial extension of the Fracture Process Zone (FPZ), thus leading us to the conclusion that multifractality emerges from a damage coalescence process, occurring within the FPZ.

In a second part, we sought to identify the minimal ingredient required to generate multifractal trajectories. We proposed two simple models, one taking into account the power-law distribution of jumps emerging from the coalescence process, and a second one built on the correlations of crack front speed within the FPZ.

These two toy models – despite their simplicity– reproduce many of the features reported in our experimental analysis, and show promise

in capturing the complexity of fracture surface morphology. However, the ad-hoc features on which these models rely (power-law distributions of jumps and crack speed correlations) would deserve further investigations. We believe that this problem could be tackled by a precise description of the cooperative dynamics of damage growth and coalescence within the fracture process zone.

5.5 TAKE-HOME MESSAGE

Four fracture surfaces of different rocks are studied. They display each a specific cut-off ξ separating multifractal and monofractal scaling regimes. A cluster and mechanical analysis shows that ξ is directly related to the Fracture Process Zone (FPZ) size ℓ_c, where dissipation mechanisms occur.

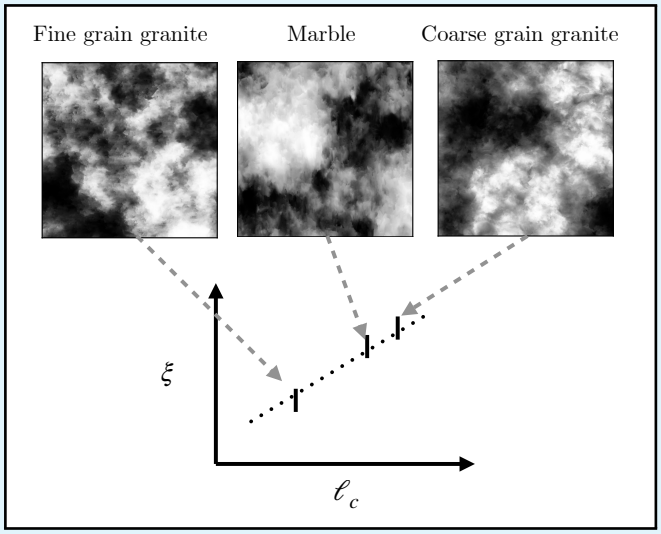

We deduce that multifractality emerges from damage coalescence occurring in the FPZ.

We test that conclusion by implementing toy models, whose ad-hoc assumptions are based on experimental observations. A first discrete model assumes truncated power-law jumps (see below), and a second one assumes time-correlated crack front speed fluctuations.

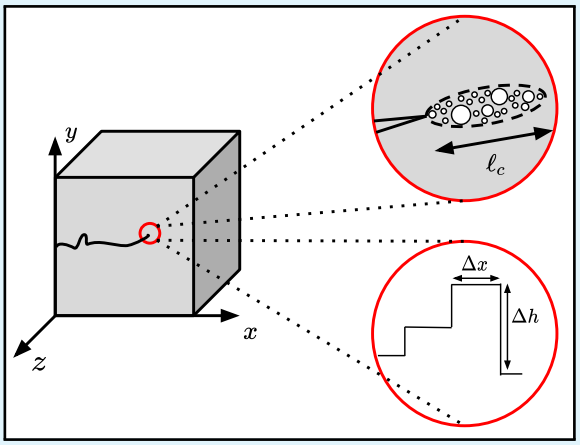

These models retrieve the transition from multifractal persistency to monofractal diffusive scaling, but could be improved further from a study of the collective dynamics of damage coalescence.

CONCLUSION

In the following conclusion, I first summarize the contributions presented in this thesis and then highlight some mutual or original continuations of these works. Note that some perspectives are also discussed at the end of each chapter.

1

SUMMARY OF WORK(S)

In the first part of the thesis, I produced a fluctuation-based approach of image analysis and processing. In particular, I employed quantitative descriptors related to information content and disorder.

In Chapter. 1, the link between visual appreciation and statistical properties of images was studied. To do so, I deployed a large-scale experiment on visual appreciation, which relied on abstract images of different complexities. Doing so allows one to avoid a cultural bias that would likely manifest for figurative images. It was found that intermediate complexity maximized appreciation scores, and could correlate with a structural complexity measure that assesses the robustness of structures to coarse-graining/blurring. Overall, this study suggests that some simple quantitative metrics can be used as quantitative criteria for aesthetic judgment. It can also be noted that most appreciated texture display statistics recovered in natural images.
In Chapter.2, I went further in the quantitative description of image content. An information theoretical formalism was applied to assess the influence of image compression over classic entropy metrics. A first study of power-law correlated images revealed the existence of two main regimes of power-law correlated ($H < 0$) and fractal ($H > 0$) fields, whose behaviour is reminiscent of the classic percolation theory. In particular, the case $H = 0$ – which corresponds to most appreciated images in the previous social experiment – displays maximal information retention. This analysis was ultimately extended to a set of natural images, and retrieved a wide variety of behaviour, close to the $H = 0$ case. Ultimately, an application to denoising showed satisfying results, and opened the door to more applications in image processing.

In Chapter. 3, the methods introduced previously were applied to a classic image processing problem: color quantization. First, I focused on the mapping procedure by using a maximal entropy approach, based on classic L^2-norm between original and quantized image. It was found that noise can yield interesting visuals, even without local error diffusion constraint. Implementing this last constraint in a Monte-Carlo algorithm, and calibrating the kernel range from information robustness constraints introduced in Chapter.3 led to excellent visuals.

The second part of the thesis was dedicated to the statistical description of the morphology of fracture surfaces, which are obtained by the complete failure of a material. It was observed that these surfaces displayed intermittent properties [143, 145, 152], similar to the ones observed in fluid turbulence [35, 38, 154].

In Chapter. 4, we introduced a class of random fields, defined from the Multifractal Random Walk model [255]. These fields display the same multiscaling that is observed on fracture surfaces, below a characteristic length ξ. We applied the construction of such random fields backwards in order to extract the intermittent contribution ω of experimental fields, here an aluminium alloy. We found that –unlike artificial fields– the organization of intermittent events in fracture surfaces is strongly anisotropic. This is particularly the case for largest and strongest structures, which organize in cliff-like patterns reminiscent of turbulent dissipative structures near the viscosity scale. One may similarly wonder whether the topology and distribution of these structures is related to the Fracture Zone Process (FPZ) size ℓ_c where dissipation takes place during material failure.

This investigation is made in Chapter. 5, where the fracture surfaces of four distinct rock materials are studied. A first roughness analysis indicates the existence of a strong short-range multifractal regime that crossovers to a mono-affine one at scale ξ. An analysis of intermittent structures revealed that, while a form of universality emerges in the distribution and shape of clusters, the hierarchy of most singular structures is dictated by the crossover scale ξ beyond which their distribution exponentially vanishes. A mechanical analysis ultimately allowed us to show a direct relation between ξ and the FPZ size ℓ_c. This result is important as it indicates that (i) the clusters observed on ω correspond to coalescing cavities in the FPZ; (ii) the multifractality observed on fracture surfaces originates from the collective dynamics of damage coalescence, whose largest events encode ℓ_c in the surface topology. Let us note however the exceptional case of porous and granular materials such as sandstone, whose intermittent patterns originates from inter-granular crack growth, and not necessarily from this collective damage dynamics.

Finally, we note that two seemingly different class of materials in terms of their failure behavior – namely metallic alloys and rocks – display similar multi-affine properties. This suggests a common microscopic mechanism, identified in Chap. 5 as a collective damage coalescence process. The toy models proposed at the end of Chap. 5 are a first step towards that coalescence based modelling, as they intend to capture this collective dynamics and assess their impact on the overall failure properties of materials. Maybe a natural next step would be the investigation of out-of-equilibrium coalescence models, that may recover the scaling properties of crack dynamics, and the intermittent properties of fracture surfaces.

2

FURTHER PERSPECTIVES

On ne fait jamais attention à ce qui a été fait ;
on ne voit que ce qui reste à faire.

— Marie Curie

Here I present a few research directions that I believe could extend the general aspect of the works presented in this thesis.

Quantitative Aesthetics experiments – In Chapter. 1, I produced a survey experiment using a finite sample of $1/f^{\alpha}$ Gaussian fields. This work could be extended by introducing a continuous cursor on α instead of a binary choice. Simultaneously, one could implement a non-linear propagation of each spectral modes to introduce smooth structural changes smooth, similarly to wave simulations. Using more complex images such as the synthetic multifractal fields introduced in Chap. 5 could also lead to interesting developments, that may relate to the peculiar properties of natural images gradient seen in Chap. 2. Note that this would require a user-friendly exploration of the parameter space.

How about color? – We have investigated the influence of the grayscale levels on visual preference. A natural extension would be of colored images, whose analysis have shown some specific correlations in pictorial art analysis [41, 310]. Similarly to Chapter. 1, one could design sets of images with given generation rules and use them in large-scale survey experiments. For example in Fig. 2.1, we sampled a random fractal image for which RGB canals were respectively lagged using a non-linear wave dispersion rule.

Resolution and Relevance of correlated noise – In Chapter. 2, we studied the influence of the roughness parameter H on the Multiscale Relevance measure (MSR), which captures the robustness of informations for all compression scales. We found out that $H = 0$ fields maximized the MSR, for a prescribed compression of the space coordinates. However, $H = 0$ fields also correspond to additive cascade processes, whose interscale causal properties have been reported in the literature [210, 259]. An interesting continuation of this work would consist in studying processes whose correlation structure built conditionally to the hierarchy of a prescribed compression measure, and evaluate their ability to maximize the MSR.

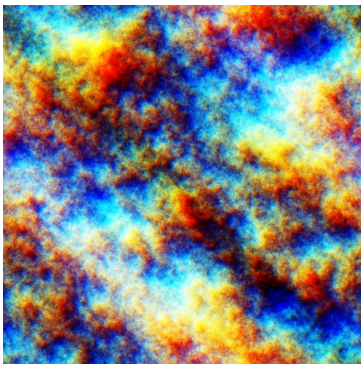

Figure 2.1: Color random surface, generated from the propagation of wave modes in each color canal, and using the dispersion relation of ocean waves [311].

Multifractal fields with more layers – The multifractal fields introduced in Chapter. 4 extend the definition of two-layered stochastic processes (with stochastic volatility). One may wonder whether this approach is generalizable to processes with deeper layers, and under which conditions such process may display scale invariance.

Causality in random surfaces – We have seen in Chapter. 4 and 5 that fracture surfaces were the result of an incremental growth of damage, that could be seen at large scale as a line propagation in a 3D material. One can wonder whether the position of a line at given time (an iso-time line) can be inferred from surfaces. This could allow one to reconstruct the full path of a crack, for example in the context of material failure investigations. A promising solution – explored during the thesis but absent from this manuscript – may employ causal observables inherited from financial time series analysis[312–315], and that have been recently translated in terms of wavelet coefficients [205]. These results could be directly compared with the surfaces obtained from crack propagation simulations [287] or other line growth models [56].

Numerical investigation of aerodynamic structures through intermittent forcing – The effect of aerodynamic structures on the local fluid velocity field can be numerically studied by using inflow boundary conditions. These limit conditions can be laminar, or reproduce advected turbulence from random Fourier modes methods [316, 317]. However, the synthetic turbulence used in those experiments does not display the non-Gaussian statistics observed in experimental flows, and that may lead to strong local deviations of the fluid behaviour. A way to bring more predictability would consist in enforcing intermittent statistics, by using the framework developed in Chapter. 4. Doing so would allow for the tuning of the non-linear contribution of turbulent

flows, and build a wider range of stress tests in computational fluid dynamics experiments.

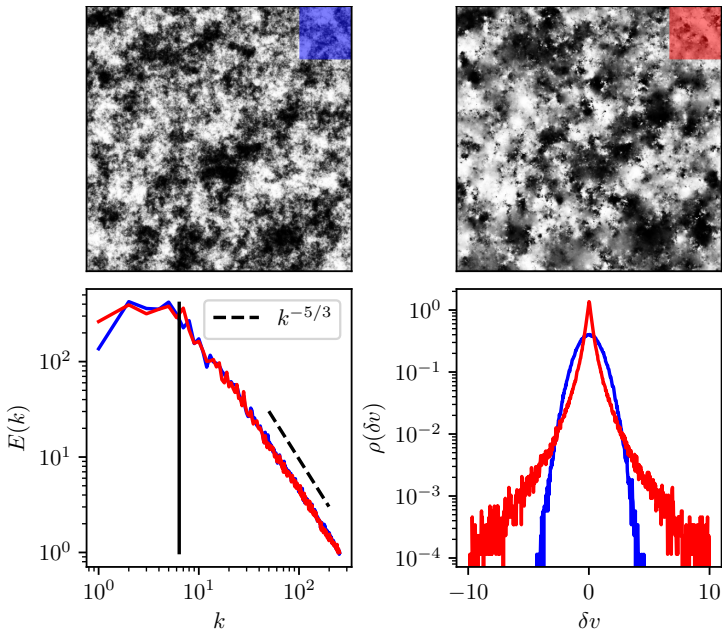

Figure 2.2: Gaussian and non-Gaussian turbulence. (Top) Quantile representation of turbulent scalar fields ($H = 1/3,\ S = 512 \times 512$) with injection scale $k_{\text{inj}}^{-1} = 20$ pixels. Top-Left is Gaussian. Top-Right is non-Gaussian of parameters $(\lambda = 0.15, \xi = 20)$. Bottom-Left displays the energy spectrum $E(k)$ of both fields, which are almost identical, as they display similar second order correlations. The vertical line indicates the injection scale from which the scale invariance begins. Bottom-Right displays the probability distribution functions of the underlying fluctuation fields $\delta h(\boldsymbol{r})$. The deviation from Gaussianity manifests in the form of fat-tailed statistics.

Part III

APPENDIX

A

APPENDIX OF CHAPTER 2

A.1 GENERATION OF $1/f^{\alpha}$ GAUSSIAN FIELDS

The $1/f^{\alpha}$ textures used in Sec. A.1 are generated through a filtering procedure. Consider a field $\phi(\boldsymbol{r})$ of given autocorrelation function $C(\boldsymbol{r})$. Using the convolution theorem one has $\tilde{C}(\boldsymbol{q}) = |\tilde{\phi}(\boldsymbol{q})|^2$ in Fourier space with $|\boldsymbol{q}| = f$. A natural way to generate a random Gaussian field ϕ with prescribed correlations is:

$$\phi = \mathcal{F}^{-1}\left(\sqrt{|\tilde{C}(\boldsymbol{q})|}\tilde{\eta}(\boldsymbol{q})\right), \tag{A.1}$$

where $\eta(\boldsymbol{r})$ is a Gaussian white noise. Note that, as a result, the textures display periodic boundary conditions. Also note that the $H = 0$ (equivalently $\alpha = 1$) case corresponds to logarithmic spatial correlations of the form (see e.g. [318]):

$$C(\boldsymbol{r}) = -\lambda\left(\log\frac{r}{\xi} + \log 2 - \gamma\right), \tag{A.2}$$

where $r = |\boldsymbol{r}|$, ξ^{-1} is a regularizing constant that can be interpreted as a low frequency cutoff, and γ is the Euler constant.

B

APPENDIX OF CHAPTER. 3

B.1 MEAN (CONVOLUTED) SQUARED ERROR

Here we derive the expression of the Mean Convoluted Squared Error (Fig. 3.1(e)). Without convolution, the expectation of the loss function reads:

$$\begin{aligned}\mathbb{E}_{\mathcal{P}}\left[\mathcal{L}(h,\hat{h})\right] &= \mathbb{E}_{\mathcal{P}}\left[\|\hat{h}-h\|_2^2\right] \\ &= \sum_{\boldsymbol{r}} \mathbb{E}_{\mathcal{P}}\left[\left(\hat{h}(\boldsymbol{r})-h(\boldsymbol{r})\right)^2\right],\end{aligned} \tag{B.1}$$

where we have used the linearity of $\mathbb{E}_{\mathcal{P}}$. Each term inside the expectation depends on the marginal variable $\hat{h}(\boldsymbol{r})$ and can be easily computed site-by-site, such that Eq. (B.1) can be rewritten as:

$$\mathbb{E}_{\mathcal{P}}\left[\mathcal{L}(h,\hat{h})\right] = \sum_{\boldsymbol{r}} \mathbb{E}_{p_{\hat{h}(\boldsymbol{r})}}\left[\left(\hat{h}(\boldsymbol{r})-h(\boldsymbol{r})\right)^2\right]. \tag{B.2}$$

Applying the same ideas to the Mean Convoluted Squared Error yields:

$$\begin{aligned}\mathbb{E}_{\mathcal{P}}\left[\mathcal{L}_\theta(\hat{h},h)\right] &= \mathbb{E}_{\mathcal{P}}\left[\|(\hat{h}-h)\circledast\theta\|_2^2\right] \\ &= \sum_{\boldsymbol{r}} \mathbb{E}_{\mathcal{P}}\left[\left((\hat{h}-h)\circledast\theta(\boldsymbol{r})\right)^2\right].\end{aligned} \tag{B.3}$$

Developing the square leads to: $\mathbb{E}_{\mathcal{P}}[\mathcal{L}_\theta(\hat{h},h)] =$

$$\sum_{\boldsymbol{r},\boldsymbol{r_1},\boldsymbol{r_2}} \theta(\boldsymbol{r}-\boldsymbol{r_1})\theta(\boldsymbol{r}-\boldsymbol{r_2})\mathbb{E}_{\mathcal{P}}\left[\left(\hat{h}(\boldsymbol{r_1})-h(\boldsymbol{r_1})\right)\left(\hat{h}(\boldsymbol{r_2})-h(\boldsymbol{r_2})\right)\right]. \tag{B.4}$$

The marginal distributions being independent, non-diagonal second order terms (with $\boldsymbol{r_1}\neq\boldsymbol{r_2}$) inside the expectation can be written as products of order 1 expectations. Rewriting the diagonal in terms of squared expectations leads to the following expression: $\mathbb{E}_{\mathcal{P}}\left[\mathcal{L}_\theta(\hat{h},h)\right] =$

$$\|\mathbb{E}_{\mathcal{P}}[\hat{h}-h]\circledast\theta\|_2^2 + \left(\mathbb{E}_{\mathcal{P}}\left[\mathcal{L}(h,\hat{h})\right] - \|\mathbb{E}_{\mathcal{P}}[\hat{h}-h]\|_2^2\right)\|\theta\|_2^2, \tag{B.5}$$

where $\mathbb{E}_{\mathcal{P}}[\mathcal{L}(h,\hat{h})]$ is the previously defined Mean Squared Error in Eq. (B.2), and $\mathbb{E}_{\mathcal{P}}[\hat{h}-h]$ is the field computed using the marginal distributions on each site.

B.2 ANALOGY WITH THE RANDOM FIELD ISING MODEL

Here we show that the Convoluted Squared Error can be rewritten as the Hamiltonian of a Random Field Ising Model (RFIM). Developping the norm in Eq. (3.5), one obtains:

$$\mathcal{L}_\theta(\hat{h}, h) = \|(\hat{h} - h) \circledast \theta\|_2^2 = \sum_{\boldsymbol{r}} [(\hat{h} - h) \circledast \theta(\boldsymbol{r})]^2. \tag{B.6}$$

Rewriting explicitly the convolution product and defining the interaction matrix J as $J(\boldsymbol{r}) = \sum_{\boldsymbol{r}'} \theta(\boldsymbol{r}')\theta(\boldsymbol{r}' - \boldsymbol{r})$, one obtains:

$$\mathcal{L}_\theta(\hat{h}, h) = \sum_{\boldsymbol{r},\boldsymbol{r}'} [\hat{h}(\boldsymbol{r}) - h(\boldsymbol{r})] J(\boldsymbol{r}' - \boldsymbol{r}) [\hat{h}(\boldsymbol{r}') - h(\boldsymbol{r}')]. \tag{B.7}$$

Since the loss is essentially defined up to a constant, one can discard $\hat{h}$-independent terms in Eq. (B.7), such that $\mathcal{L}_\theta(\hat{h}, h) \equiv \mathcal{H}_h[\hat{h}]$ where:

$$\mathcal{H}_h[\hat{h}] := \sum_{\boldsymbol{r},\boldsymbol{r}'} \hat{h}(\boldsymbol{r}) J(\boldsymbol{r}' - \boldsymbol{r}) \hat{h}(\boldsymbol{r}') - 2 \sum_{\boldsymbol{r}'} (h \circledast J)(\boldsymbol{r}') \hat{h}(\boldsymbol{r}'). \tag{B.8}$$

Interestingly, when replacing $\hat{h}$ by a spin field ϕ, one precisely recovers the Antiferromagnetic RFIM Hamiltonian $\mathcal{H}[\phi]$ which, within the braket formalism writes:

$$\mathcal{H}_h[\phi] = \langle \phi | J | \phi \rangle - 2 \langle h | J | \phi \rangle, \tag{B.9}$$

where $|h_{\text{eff}}\rangle = 2J|h\rangle$ is the effective external field. Therefore, spins and external field in the Ising model respectively play the same role as the transformed and original images in the color quantization problem. A well-known property of the Antiferromagnetic RFIM, that is interactions encouraging alternations between neighbouring spins, is for example recovered in our observations, see Fig. 3.2(a).

B.3 RESOLUTION/RELEVANCE FORMALISM

Here we introduce the formalism used to set the optimal convolution parameter in Sec. 3.5. The idea, detailed in [20, 127, 128], consists in studying a data sample for different resolution/compression levels and calculating entropy-based observables.

Let $\mathcal{S} = (s_1, ..., s_N)$ be a sample of data, and ℓ a compression parameter. One can transform the original sample into a compressed one $\mathcal{S}^\ell = (s_1^\ell, ..., s_N^\ell)$ such that $\ell = 1$ corresponds to no compression ($\mathcal{S}^1 = \mathcal{S}$) and $\ell = L$ to the totally compressed sample (quasi-degenerate data). At each compression level ℓ, one can easily calculate the number k_s^ℓ of times the state s appears in the sample $\mathcal{S}^\ell$, and the number m_k^ℓ of states appearing k times. One can then define the *resolution* as the entropy of the empirical distribution of states:

$$\hat{H}^\ell[s] = -\sum_s \frac{k_s^\ell}{N} \log \frac{k_s^\ell}{N} = -\sum_k \frac{k m_k^\ell}{N} \log \frac{k}{N}. \tag{B.10}$$

Another useful observable is the *relevance* defined as the entropy computed from the states sharing the same occurrence frequency:

$$\hat{H}^{\ell}[k] = \sum_{k} \frac{km_k^{\ell}}{N} \log \frac{km_k^{\ell}}{N}. \tag{B.11}$$

This measure of *relevance* is indeed the most direct way to encode the underlying distribution of the original data. As the latter entropy takes less bits to encode, one has $\hat{H}^{\ell}[k] < \hat{H}^{\ell}[s]$, explaining why the data in Fig. 3.5(a) is under the $y = x$ line. In order to quantify the way information spreads across compression levels, we define the compression rate $\mu_{\ell \to \ell+1}$ between two successive compression levels as the ratio between loss in relevance and loss in resolution:

$$\mu_{\ell \to \ell+1} := \frac{\hat{H}^{\ell+1}[k] - \hat{H}^{\ell}[k]}{\hat{H}^{\ell+1}[s] - \hat{H}^{\ell}[s]}. \tag{B.12}$$

In the right part of Fig. 3.5(a) and for the first compression steps (low values of ℓ), $\hat{H}[k]$ is a decreasing function of $\hat{H}[s]$, resulting in negative μ. Interestingly, this means that compressing the sample increases the amount of relevant information it contains about the underlying distribution. However, when ℓ increases further, we reach an oversampling regime (left part of Fig. 3.5(a)) for which further compression reduces both relevance and resolution.

In the case of color quantization, we wish to gain information relevance as we range from low to higher compression in the most scale-invariant way possible. This way, we avoid the scale-specific tradeoff described in Fig. 3.3. Optimality in that regard is therefore reached by taking μ close to -1 and as constant as possible in the undersampling regime, by that justifying the linear regression introduced in Sec. 3.3.2.

C

APPENDIX OF CHAPTER 4

C.1 THE CASE H=0

We generated monofractal Gaussian fields in the case $d = 2$, $H = 0$. Let us note that this case corresponds to both log-correlated Gaussian fields (LGF) and Gaussian free field (GFF) [210, 319, 320], whose Lagrangian functional is

$$\mathcal{L}[\phi] = (\nabla\phi)^2 + \frac{1}{\xi^2}\phi^2.$$

The results are shown in Fig. C.1(a) and (b). The difference of ξ directly influences the range of correlations and the visuals. The correlation functions in (c), possess asymptotic logarithmic behaviour, and can be conveniently collapsed in (d). This ability to tune the logarithmic range is useful to control the properties of synthetic multifractal fields.

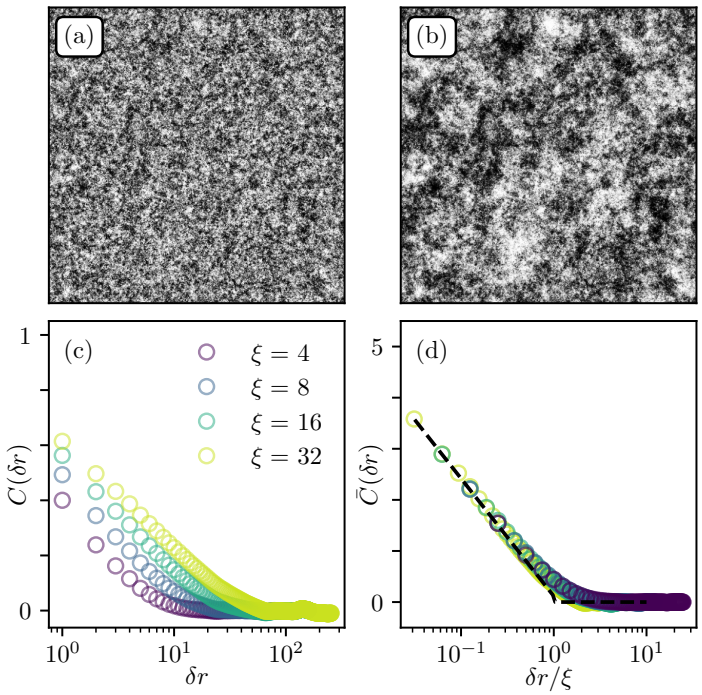

Figure C.1: Influence of ξ on sampled Gaussian fields for $d = 2$ and $H = 0$. (a),(b) Quantile representation of 512×512 samples for $\xi \in \{4, 32\}$ respectively. (c),(d) Isotropic autocorrelation functions for several cut-off values with (d) rescaled by ξ over the δr-axis, and by the pre-exponent λ over the C-axis. Black dotted line is the logarithmic regime.

C.2 SCALING OF THE MRF

In this appendix we consider a field h obtained from the construction described in the main text. We demonstrate that the jumps, $\Delta_\ell h(\boldsymbol{r}) = h(\boldsymbol{r}+\ell) - h(\boldsymbol{r})$ describe a stationary process whose moments scale with ℓ. We recall that $h(\boldsymbol{r}), \boldsymbol{r} \in \mathbb{R}^d$ is built from the fractional integration of $\delta h(\boldsymbol{r}) = s_\epsilon(\boldsymbol{r}) e^{\omega_\epsilon(\boldsymbol{r})}$, where the limit $\epsilon \to 0$ is taken here. This will allow us to make calculations in the continuous field limit. We consider Gaussian statistics for s and ω and the following correlations:

$$\begin{cases} C_s(\boldsymbol{r}) \propto \delta^d(\boldsymbol{r}) \\ C_\omega(\boldsymbol{r}) \approx -\lambda \log \frac{r}{\xi}\ ,\ r < \xi. \end{cases} \tag{C.1}$$

The relation $h(\boldsymbol{r}) = (-\Delta)^{-\frac{H+d/2}{2}} \delta h(\boldsymbol{r})$ rewrites in terms of Riesz potential [321] as:

$$h(\boldsymbol{r}) = \int_{\mathbb{R}^d} d\boldsymbol{r_1} \frac{\delta h(\boldsymbol{r}+\boldsymbol{r_1})}{\|\boldsymbol{r_1}\|^{\frac{d}{2}-H}}. \tag{C.2}$$

From now on, integrals will always be over the whole domain $\mathbb{R}^d$, unless specified otherwise.

C.2.1 *Stationarity of increments*

We calulate the q-th order moments of jumps between $\boldsymbol{r} - \frac{\ell}{2}$ and $\boldsymbol{r} + \frac{\ell}{2}$, with $\ell = \ell \boldsymbol{e}$, ($\|\boldsymbol{e}\| = 1$) and $q = 2m$. Using the symmetry of the kernel, the order q variogram writes as:

$$\langle |h(\boldsymbol{r}+\frac{\ell}{2}) - h(\boldsymbol{r}-\frac{\ell}{2})|^q \rangle = \int d\boldsymbol{r_1} \cdots \int d\boldsymbol{r_q} \prod_{i=1}^{q} \left[\|\boldsymbol{r}+\frac{\ell}{2} - \boldsymbol{r_i}\|^{H-\frac{d}{2}} - \|\boldsymbol{r}-\frac{\ell}{2} - \boldsymbol{r_i}\|^{H-\frac{d}{2}} \right] \langle \prod_i^q \delta h(\boldsymbol{r_i}) \rangle. \tag{C.3}$$

The fields s and ω being independent, one gets:

$$\langle \prod_i^q \delta h(\boldsymbol{r_i}) \rangle = \langle \prod_{i=1}^q s(\boldsymbol{r}_i) \rangle \langle e^{\sum_i^q \omega(\boldsymbol{r}_i)} \rangle, \tag{C.4}$$

which becomes, using the Wick theorem and the characteristic function of multivariate Gaussian processes leads to:

$$\langle \prod_i^q \delta h(\boldsymbol{r_i}) \rangle = \prod_{i_1,\ldots,i_{2m}} C_s(\boldsymbol{r}_{\boldsymbol{i_1}} - \boldsymbol{r}_{\boldsymbol{i_2}}) \times \cdots \times C_s(\boldsymbol{r}_{\boldsymbol{i_{2m-1}}} - \boldsymbol{r}_{\boldsymbol{i_{2m}}}) \times B e^{\frac{1}{2}\sum_{i\neq j=1}^{2m} \frac{1}{2} C_\omega(\boldsymbol{r}_i - \boldsymbol{r}_j)}, \tag{C.5}$$

where B is the variance/diagonal term of the correlation matrix, unimportant here as we observe the scaling exclusively. Injecting this last

expression in the first integral and applying the change of variable $\boldsymbol{r_i} \to \boldsymbol{r_i} + \boldsymbol{r}$ suppresses $\boldsymbol{r}$ from the expression. The functional now exclusively depends on ℓ, which implies stationarity/translation invariance. This translates as the following:

$$V_q(\ell) = \langle |h(\boldsymbol{r} + \frac{\ell}{2}) - h(\boldsymbol{r} - \frac{\ell}{2})|^q \rangle \tag{C.6}$$

$$= \langle |h(\ell) - h(\boldsymbol{0})|^q \rangle. \tag{C.7}$$

We also note the rotation invariance of $V_q(\ell)$.

C.2.2 *Asymptotic scaling*

We establish the scaling of jumps $h(\ell) - h(\boldsymbol{0})$ in the $\ell \ll \xi$ limit of Eq. C.3. The moments of order $q = 2m$ write:

$$V_q(\ell) = \int d\boldsymbol{r_1} \cdots \int d\boldsymbol{r_q} \times \prod_{i=1}^{q} \left[\|\boldsymbol{r}_i - \frac{\ell}{2}\|^{H-\frac{d}{2}} - \|\boldsymbol{r}_i + \frac{\ell}{2}\|^{H-\frac{d}{2}} \right] \langle \prod_{i}^{q} \delta h(\boldsymbol{r_i}) \rangle \tag{C.8}$$

Using that s is δ-correlated, we identify successive terms $\boldsymbol{r_{2i-1}} = \boldsymbol{r_{2i}}$ and get:

$$V_q(\ell) = \int d\boldsymbol{r_2} \cdots \int d\boldsymbol{r_{2m}} \times \prod_{i=1}^{m} \left[\|\boldsymbol{r_{2i}} - \frac{\ell}{2}\|^{H-\frac{d}{2}} - \|\boldsymbol{r_{2i}} + \frac{\ell}{2}\|^{H-\frac{d}{2}} \right]^2 \times B \prod_{i \neq j=1}^{m} e^{-\frac{1}{2} C_\omega(\boldsymbol{r_{2i}} - \boldsymbol{r_{2j}})}. \tag{C.9}$$

Note that this integral is well defined for $H < 1$. Similarly to [255], we make the change of variable $\boldsymbol{r}_i = \ell \boldsymbol{u}_i$ and recover:

$$V_q(\ell) \propto \ell^{2mH} \int d\boldsymbol{u_2} \cdots \int d\boldsymbol{u_{2m}} \prod_{i=1}^{m} \left[\|\boldsymbol{u_{2i}} - \frac{\boldsymbol{e}}{2}\|^{H-\frac{d}{2}} - \|\boldsymbol{u_{2i}} + \frac{\boldsymbol{e}}{2}\|^{H-\frac{d}{2}} \right]^2 \times \prod_{i \neq j=1}^{m} e^{-\frac{1}{2} C_\omega(\ell(\boldsymbol{u_{2i}} - \boldsymbol{u_{2j}}))}. \tag{C.10}$$

To recover the scaling of this last integral term, we split the integration domain into the reunions of subsets $\|\boldsymbol{u_i} - \boldsymbol{u_j}\| < \xi/\ell$. This allows one to extract the logarithmic correlations of C_ω, leading to a dominant term of the form $\ell^{-2\lambda^2 m(m-1)}$.

Power counting all contributions finally leads to $V_{2m}(\ell) \propto \ell^{2mH - 2\lambda^2 m(m-1)}$, which recovers:

$$V_q(\ell) \underset{\ell \ll \xi}{=} K_q \ell^{\zeta_q}, \tag{C.11}$$

where K_q depends on the standard deviation of s and ζ_q is the scaling exponent spectrum of expression:

$$\zeta_q = qH - \frac{\lambda^2}{2} q(q-2), \tag{C.12}$$

which corresponds to the MRW scaling for $H = 1/2$. Finally, note that this scaling can be generalized to all q from analytical continuation arguments.

C.3 SELF-SIMILARITY KERNEL AND FLUCTUATION RATIO $W_{\ell/L}$ DISTRIBUTION

The fluctuation ratio $\langle W^q_{\ell/L} \rangle = (\ell/L)^{\zeta_q}$ is characterized by its moments:

$$\langle W^q_{\ell/L} \rangle = (\ell/L)^{\zeta_q} = e^{\log \frac{\ell}{L} \left(qH - \frac{\lambda}{2} q(q-2) \right)}, \tag{C.13}$$

which corresponds to the moments of a log-normal distribution. The corresponding Gaussian process $\log W_{\ell/L}$ is defined by its average $\mu = (H+\lambda) \log \frac{\ell}{L}$ and deviation $\sigma = \sqrt{-\lambda \log \frac{\ell}{L}}$, leading to the distribution:

$$G_{\ell/L}(u) = \frac{1}{\sqrt{-2\pi\lambda \log(\frac{\ell}{L})}} e^{\frac{((H+\lambda)\log(\frac{\ell}{L}) - u)^2}{2\lambda \log(\frac{\ell}{L})}}. \tag{C.14}$$

C.4 SYNTHESIS AND ANALYSIS OF MULTIFRACTAL FIELDS

In the following, we estimate the multifractal parameters of several synthetic multifractal fields.

In Fig. C.2, we modify the Hurst roughness exponent H from 0.1 to 0.9. For $H \approx 0.5$, estimations from the scaling exponent spectrum ζ_q are generally good. For extreme values of H however, the estimated values of H and λ deviate from entry values. Note however that this problem can be solved through the power spectrum estimation of the roughness $H = \zeta_2/2$ [244, 322], and the extended self-similarity estimation of λ [323]. The estimations from $\hat{\omega}$ are in perfect agreement.

In Fig. C.3, we modify λ from 0.01 to 0.50. For $0 < \lambda < .2$, estimations from the scaling exponent spectrum ζ_q or from the local log-volatility $\hat{\omega}$ recover good agreement. Note that a low value of λ prevents a correct estimation of $\hat{\omega}$, leading to the discrepancy observed at $\lambda = 0.01$. As λ gets higher, the volatility based analysis should be privileged. Note however that λ rarely goes beyond 0.25 in experimental data.

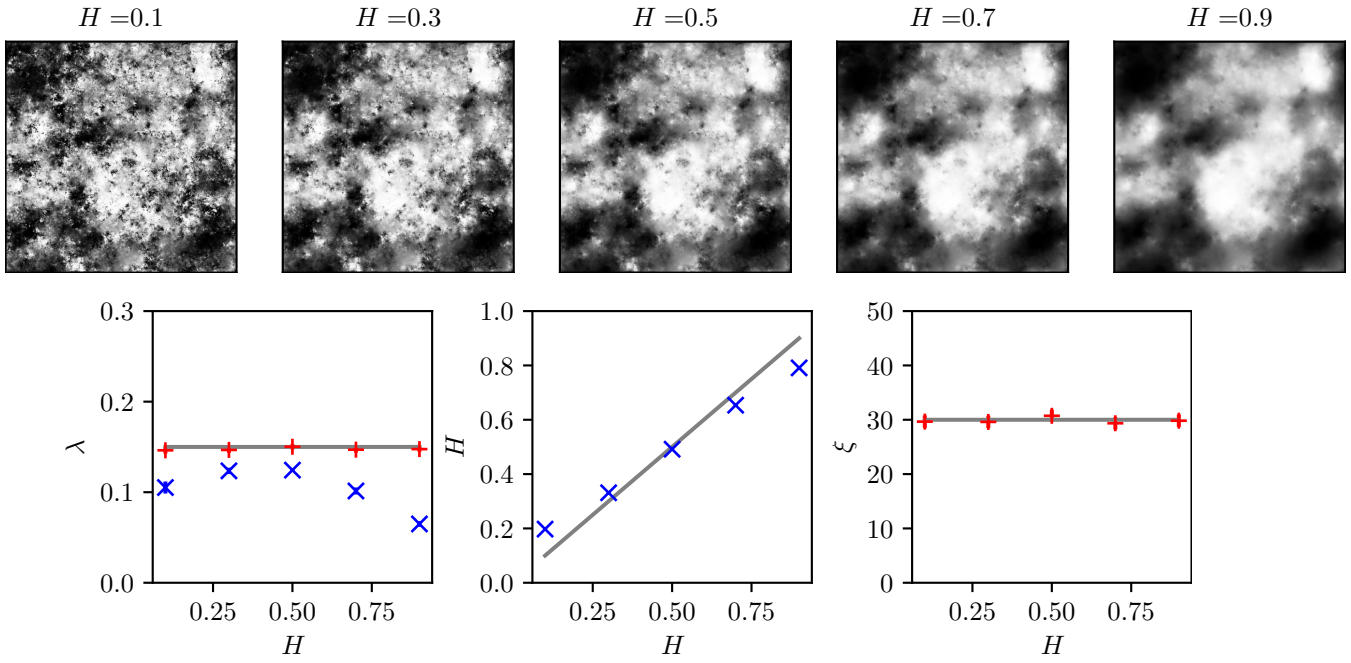

Figure C.2: Influence of the roughness exponent H. (Top) Quantile representation of simulated fields of size $L = 512$ for $H = \{0.1, 0.3, 0.5, 0.7, 0.9\}$, $\lambda = 0.15$ and $\xi = 30$ pixels. (Bottom) Estimated parameters. Red $(+)$ markers correspond to C_ω estimations. Blue $(\times)$ markers correspond to ζ_q estimations.

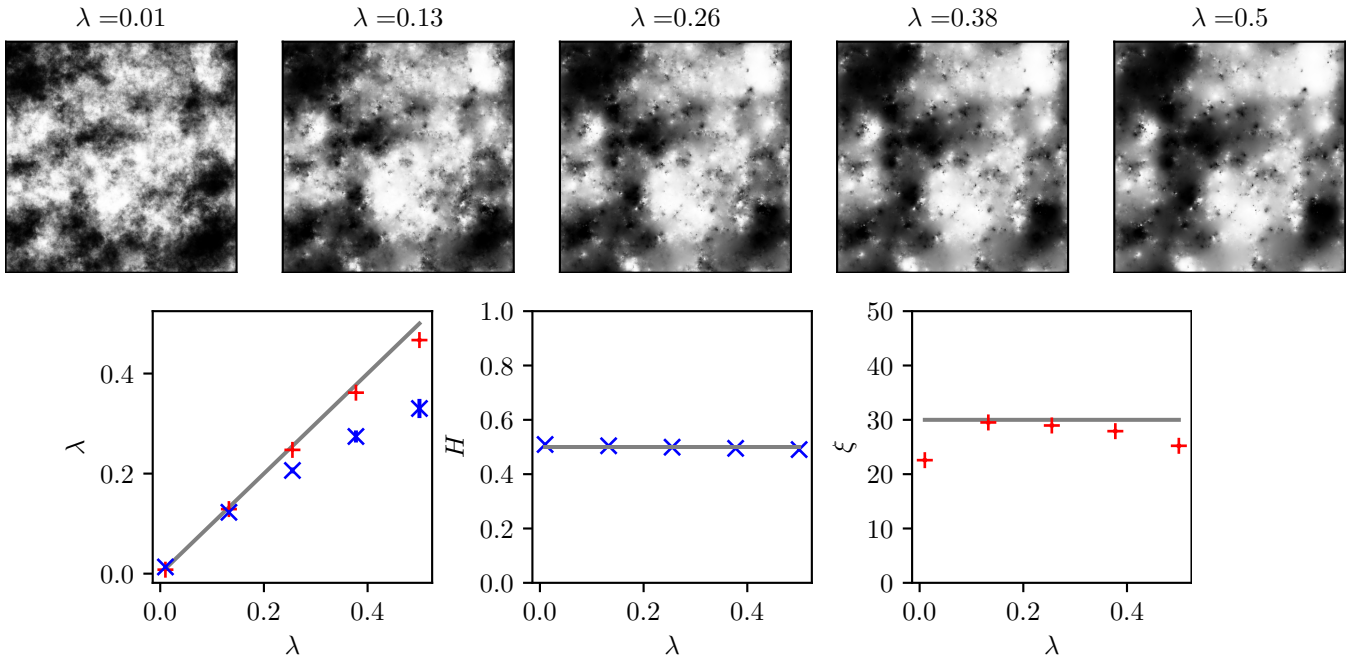

Figure C.3: Influence of the intermittency coefficient λ. (Top) Quantile representation of simulated fields of size $L = 512$ for $\lambda = \{0.01, 0.13, 0.25, 0.38, 0.5\}$, $H = 0.5$ and $\xi = 30$ pixels. (Bottom) Estimated parameters. Red $(+)$ correspond to C_ω estimations. Blue $(\times)$ correspond to ζ_q estimations.

BIBLIOGRAPHY

[1] S. Lakhal, A. Darmon, J.-P. Bouchaud, and M. Benzaquen, "Beauty and structural complexity," Physical Review Research **2**, 022058 (2020).

[2] S. Lakhal, A. Darmon, and M. Benzaquen, "A new spin on color quantization," Journal of Statistical Mechanics: Theory and Experiment **2023**, 033401 (2023).

[3] S. Lakhal, A. Darmon, I. Mastromatteo, M. Marsili, and M. Benzaquen, "Multiscale relevance of natural images," Scientific Reports **13**, 14879 (2023).

[4] S. Lakhal, L. Ponson, M. Benzaquen, and J.-P. Bouchaud, "Wrapping and unwrapping multifractal fields," In preparation (2023).

[5] S. Lakhal and M. Benzaquen, "Can beauty be quantified?" Trans. by T. Zoé, Polytechnique Insights (2021).

[6] H. Haken, *Information and self-organization: a macroscopic approach to complex systems* (Springer Science & Business Media, 2006).

[7] W. B. Arthur, "Complexity economics," Complexity and the Economy (2013).

[8] R. K. Sawyer, *Social emergence: societies as complex systems* (Cambridge University Press, 2005).

[9] H. Kitano, "Computational systems biology," Nature **420**, 206 (2002).

[10] P. Pajot, *La naissance d'une théorie au carrefour des disciplines*, fr.

[11] E. Ising, "Beitrag zur Theorie des Ferromagnetismus," de, Zeitschrift für Physik **31**, 253 (1925).

[12] G. Tkacik, E. Schneidman, M. J. Berry II, and W. Bialek, "Ising models for networks of real neurons," arXiv preprint q-bio/0611072 (2006).

[13] D. Stauffer, "Opinion dynamics and sociophysics," arXiv preprint arXiv:0705.0891 (2007).

[14] W.-X. Zhou and D. Sornette, "Self-organizing ising model of financial markets," The European Physical Journal B **55**, 175 (2007).

[15] R. T. Pierrehumbert, "Fluid mechanics: the quintessential complex system," Journal of Fluid Mechanics **938**, F1 (2022).

[16] A. N. Kolmogorov, "On tables of random numbers," Sankhyā: The Indian Journal of Statistics, Series A, 369 (1963).

[17] A. N. Kolmogorov, "On tables of random numbers," Theoretical Computer Science **207**, 387 (1998).

[18] M. S. Burgin, "Generalized kolmogorov complexity and duality in computational theory," in Doklady akademii nauk, Vol. 264, 1 (Russian Academy of Sciences, 1982), pp. 19–23.

[19] M. Li, P. Vitányi, et al., *An introduction to kolmogorov complexity and its applications*, Vol. 3 (Springer, 2008).

[20] R. J. Cubero, M. Marsili, and Y. Roudi, "Multiscale relevance and informative encoding in neuronal spike trains," Journal of computational neuroscience **48**, 85 (2020).

[21] Y.-C. Zhang, "Complexity and 1/f noise. a phase space approach," Journal de Physique I **1**, 971 (1991).

[22] S. Aaronson, S. M. Carroll, and L. Ouellette, "Quantifying the rise and fall of complexity in closed systems: the coffee automaton," arXiv preprint arXiv:1405.6903 (2014).

[23] M. Marsili and Y. Roudi, "Quantifying relevance in learning and inference," Physics Reports **963**, 1 (2022).

[24] S. Prakash, S. Havlin, M. Schwartz, and H. E. Stanley, "Structural and dynamical properties of long-range correlated percolation," Physical Review A **46**, R1724 (1992).

[25] D. H. Zanette, "Quantifying the complexity of black-and-white images," PloS one **13** (2018).

[26] L. Bachelier, "Théorie de la spéculation," in Annales scientifiques de l'école normale supérieure, Vol. 17 (1900), pp. 21–86.

[27] R. B. F. H. M. R. A. V.P.L.S., "Xxvii. a brief account of microscopical observations made in the months of june, july and august 1827, on the particles contained in the pollen of plants; and on the general existence of active molecules in organic and inorganic bodies," The Philosophical Magazine **4**, 161 (1828).

[28] A. Einstein, *Investigations on the theory of the brownian movement* (Courier Corporation, 1956).

[29] P. Lévy, *Calcul des probabilités* (Gauthier-Villars, 1925).

[30] B. B. Mandelbrot and B. B. Mandelbrot, *The fractal geometry of nature*, Vol. 1 (WH freeman New York, 1982).

[31] D Boyer and J. Romo-Cruz, "Solvable random-walk model with memory and its relations with markovian models of anomalous diffusion," Physical Review E **90**, 042136 (2014).

[32] J.-P. Bouchaud and A. Georges, "Anomalous diffusion in disordered media: statistical mechanisms, models and physical applications," Physics reports **195**, 127 (1990).

[33] A. Kolmogorov, "The Local Structure of Turbulence in Incompressible Viscous Fluid for Very Large Reynolds' Numbers," Akademiia Nauk SSSR Doklady **30**, 301 (1941).

[34] M. S. Abdelgawad, I. Cannon, and M. E. Rosti, "Scaling and intermittency in turbulent flows of elastoviscoplastic fluids," Nature Physics, 1 (2023).

[35] U. Frisch, *Turbulence: the legacy of an kolmogorov* (Cambridge university press, 1995).

[36] A. N. Kolmogorov, "Dissipation of energy in the locally isotropic turbulence," Proceedings of the Royal Society of London. Series A: Mathematical and Physical Sciences **434**, 15 (1991).

[37] S. Nazarenko, *Wave turbulence*, Vol. 825 (Springer Science & Business Media, 2011).

[38] U. Frisch and G. Parisi, "Fully developed turbulence and intermittency," New York Academy of Sciences, Annals **357**, 359 (1980).

[39] L. F. Richardson, *Weather prediction by numerical process* (University Press, 1922).

[40] J. Beattie and N. Kriel, "Is the starry night turbulent?" arXiv preprint arXiv:1902.03381 (2019).

[41] J. L. Aragón, G. G. Naumis, M. Bai, M. Torres, and P. K. Maini, "Turbulent luminance in impassioned van gogh paintings," Journal of Mathematical Imaging and Vision **30**, 275 (2008).

[42] M. Kardar, G. Parisi, and Y.-C. Zhang, "Dynamic scaling of growing interfaces," Phys. Rev. Lett. **56**, 889 (1986).

[43] M. Hairer, "Solving the kpz equation," Annals of mathematics, 559 (2013).

[44] F. Family, "Dynamic scaling and phase transitions in interface growth," Physica A: Statistical Mechanics and its Applications **168**, 561 (1990).

[45] T. Antal and Z. Rácz, "Dynamic scaling of the width distribution in edwards-wilkinson type models of interface dynamics," Phys. Rev. E **54**, 2256 (1996).

[46] D. Ertaş and M. Kardar, "Dynamic roughening of directed lines," Physical Review Letters **69**, 929 (1992).

[47] J.-P. Bouchaud, "Models of randomness and complexity, from turbulence to stock markets," Leonardo **41**, 239 (2008).

[48] A. Rosso and W. Krauth, "Roughness at the depinning threshold for a long-range elastic string," Phys. Rev. E **65**, 025101 (2002).

[49] H. Leschhorn, "Interface depinning in a disordered medium — numerical results," Physica A: Statistical Mechanics and its Applications **195**, 324 (1993).

[50] G. Düring, C. Josserand, and S. Rica, "Weak turbulence for a vibrating plate: can one hear a kolmogorov spectrum?" Phys. Rev. Lett. **97**, 025503 (2006).

[51] P. Di Francesco, H Saleur, and J. Zuber, "Critical ising correlation functions in the plane and on the torus," Nuclear Physics B **290**, 527 (1987).

[52] C. Borghesi and J.-P. Bouchaud, "Spatial correlations in vote statistics: a diffusive field model for decision-making," The European Physical Journal B **75**, 395 (2010).

[53] L. Caffarelli and L. Silvestre, "An extension problem related to the fractional laplacian," Communications in partial differential equations **32**, 1245 (2007).

[54] C. Le Priol, P. Le Doussal, and A. Rosso, "Spatial clustering of depinning avalanches in presence of long-range interactions," Physical Review Letters **126**, 025702 (2021).

[55] B. Pesquet-Popescu and J. L. Véhel, "Stochastic fractal models for image processing," IEEE Signal Processing Magazine **19**, 48 (2002).

[56] A.-L. Barabási and H. E. Stanley, *Fractal concepts in surface growth* (Cambridge university press, 1995).

[57] C. Husemann and K. J. Wiese, "Field theory of disordered elastic interfaces at 3-loop order: critical exponents and scaling functions," Nuclear Physics B **932**, 589 (2018).

[58] B. Delamotte, "An introduction to the nonperturbative renormalization group," Renormalization group and effective field theory approaches to many-body systems, 49 (2012).

[59] K. Alvelius, "Random forcing of three-dimensional homogeneous turbulence," Physics of Fluids **11**, 1880 (1999).

[60] A. Chekhlov and V. Yakhot, "Kolmogorov turbulence in a random-force-driven burgers equation," Physical Review E **51**, R2739 (1995).

[61] A. Sain, R. Pandit, et al., "Turbulence and multiscaling in the randomly forced navier-stokes equation," Physical Review Letters **81**, 4377 (1998).

[62] D. Bernard, G. Boffetta, A. Celani, and G. Falkovich, "Conformal invariance in two-dimensional turbulence," Nature Physics **2**, 124 (2006).

[63] D. Bernard, G. Boffetta, A. Celani, and G. Falkovich, "Inverse turbulent cascades and conformally invariant curves," Physical Review Letters **98**, 024501 (2007).

[64] M. S. Belen'kii, S. J. Karis, C. L. Osmon, J. M. Brown II, and R. Q. Fugate, "Experimental evidence of the effects of non-kolmogorov turbulence and anisotropy of turbulence," in 18th congress of the international commission for optics, Vol. 3749 (SPIE, 1999), pp. 50–51.

[65] A. Boudaoud, O. Cadot, B. Odille, and C. Touzé, "Observation of wave turbulence in vibrating plates," Physical Review Letters **100**, 234504 (2008).

[66] E. Falcon, C. Laroche, and S. Fauve, "Observation of gravity-capillary wave turbulence," Physical Review Letters **98**, 094503 (2007).

[67] T. C. Schelling, "Dynamic models of segregation," Journal of mathematical sociology **1**, 143 (1971).

[68] J. M. Keynes, *General theory, employment, interest and money* (Palgrave-McMillan, 1936).

[69] L. Boltzmann, "Studien über das gleichgewicht der lebendigen kraft zwischen bewegten materiellen punkten," in *Wissenschaftliche abhandlungen*, Vol. 1, edited by F. Hasenöhrl, Cambridge Library Collection - Physical Sciences (Cambridge University Press, 2012), 49–96.

[70] J. W. Gibbs, *Elementary principles in statistical mechanics: developed with especial reference to the rational foundation of thermodynamics*, Cambridge Library Collection - Mathematics (Cambridge University Press, 2010).

[71] S. Kirkpatrick, C. D. Gelatt, and M. P. Vecchi, "Optimization by Simulated Annealing," Science **220**, 671 (1983).

[72] I. Goodfellow, Y. Bengio, and A. Courville, *Deep learning* (MIT press, 2016).

[73] C. M. Bishop and N. M. Nasrabadi, *Pattern recognition and machine learning*, Vol. 4, 4 (Springer, 2006).

[74] J. Bridle, "Training Stochastic Model Recognition Algorithms as Networks can Lead to Maximum Mutual Information Estimation of Parameters," in Advances in Neural Information Processing Systems, Vol. 2 (1989).

[75] S. Cocco, C. Feinauer, M. Figliuzzi, R. Monasson, and M. Weigt, "Inverse statistical physics of protein sequences: a key issues review," Reports on Progress in Physics **81**, 032601 (2018).

[76] A. de Martino and D. de Martino, "An introduction to the maximum entropy approach and its application to inference problems in biology," Heliyon **4**, 596 (2018).

[77] K Parulski and M. Rabbani, "The continuing evolution of digital cameras and digital photography systems," in 2000 ieee international symposium on circuits and systems (iscas), Vol. 5 (IEEE, 2000), pp. 101–104.

[78] S. Hochreiter and J. Schmidhuber, "Long short-term memory," Neural computation **9**, 1735 (1997).

[79] A. Krizhevsky, I. Sutskever, and G. E. Hinton, "Imagenet classification with deep convolutional neural networks," Advances in neural information processing systems **25** (2012).

[80] A. Vaswani, N. Shazeer, N. Parmar, J. Uszkoreit, L. Jones, A. N. Gomez, Ł. Kaiser, and I. Polosukhin, "Attention is all you need," Advances in neural information processing systems **30** (2017).

[81] J. Deng, W. Dong, R. Socher, L.-J. Li, K. Li, and L. Fei-Fei, "Imagenet: a large-scale hierarchical image database," in 2009 ieee conference on computer vision and pattern recognition (IEEE, 2009), pp. 248–255.

[82] C. Kang, G. Valenzise, and F. Dufaux, "Eva: an explainable visual aesthetics dataset," in Joint workshop on aesthetic and technical quality assessment of multimedia and media analytics for societal trends (2020), pp. 5–13.

[83] N. Murray, L. Marchesotti, and F. Perronnin, "Ava: a large-scale database for aesthetic visual analysis," in 2012 ieee conference on computer vision and pattern recognition (IEEE, 2012), pp. 2408–2415.

[84] O. Braddick and J. Atkinson, "Development of human visual function," Vision research **51**, 1588 (2011).

[85] K. Grill-Spector and R. Malach, "The human visual cortex," Annu. Rev. Neurosci. **27**, 649 (2004).

[86] L. I. Rudin, S. Osher, and E. Fatemi, "Nonlinear total variation based noise removal algorithms," Physica D: nonlinear phenomena **60**, 259 (1992).

[87] A. Babenko, A. Slesarev, A. Chigorin, and V. Lempitsky, "Neural codes for image retrieval," in Computer vision–eccv 2014: 13th european conference, zurich, switzerland, september 6-12, 2014, proceedings, part i 13 (Springer, 2014), pp. 584–599.

[88] J. R. Bach, C. Fuller, A. Gupta, A. Hampapur, B. Horowitz, R. Humphrey, R. C. Jain, and C.-F. Shu, "Virage image search engine: an open framework for image management," in Storage and retrieval for still image and video databases iv, Vol. 2670 (SPIE, 1996), pp. 76–87.

[89] C. Farabet, C. Couprie, L. Najman, and Y. LeCun, "Learning hierarchical features for scene labeling," IEEE transactions on pattern analysis and machine intelligence **35**, 1915 (2012).

[90] D. Lu and Q. Weng, "A survey of image classification methods and techniques for improving classification performance," International journal of Remote sensing **28**, 823 (2007).

[91] A. Ramesh, P. Dhariwal, A. Nichol, C. Chu, and M. Chen, "Hierarchical text-conditional image generation with clip latents," arXiv preprint arXiv:2204.06125 (2022).

[92] H. Maître, *Esthétique de la photographie numérique* (ISTE Group, 2022).

[93] G. D. Birkhoff, *Aesthetic measure* (Harvard University Press, 1933).

[94] J. Schmidhuber, "Formal theory of creativity, fun, and intrinsic motivation (1990–2010)," IEEE transactions on autonomous mental development **2**, 230 (2010).

[95] M. Cardaci, V. Di Gesù, M. Petrou, and M. E. Tabacchi, "A fuzzy approach to the evaluation of image complexity," Fuzzy Sets and Systems **160**, 1474 (2009).

[96] J. Rigau, M. Feixas, and M. Sbert, "An information-theoretic framework for image complexity," in Proceedings of the first eurographics conference on computational aesthetics in graphics, visualization and imaging (2005), pp. 177–184.

[97] P. Machado and A. Cardoso, "Computing aesthetics," in Advances in artificial intelligence: 14th brazilian symposium on artificial intelligence, sbia'98, porto alegre, brazil, november 4-6, 1998. proceedings 14 (Springer, 1998), pp. 219–228.

[98] J. Rigau, M. Feixas, and M. Sbert, "Conceptualizing birkhoff's aesthetic measure using shannon entropy and kolmogorov complexity.," in Cae (2007), pp. 105–112.

[99] E. Van Geert and J. Wagemans, "Order, complexity, and aesthetic appreciation.," Psychology of aesthetics, creativity, and the arts **14**, 135 (2020).

[100] B. Spehar, S. Wong, S. van de Klundert, J. Lui, C. W. G. Clifford, and R. Taylor, "Beauty and the beholder: the role of visual sensitivity in visual preference," Frontiers in Human Neuroscience **9**, 514 (2015).

[101] B. Spehar, C. W. Clifford, B. R. Newell, and R. P. Taylor, "Universal aesthetic of fractals," Computers & Graphics **27**, 813 (2003).

[102] B. Spehar, N. Walker, and R. P. Taylor, "Taxonomy of individual variations in aesthetic responses to fractal patterns," Frontiers in Human Neuroscience **10**, 350 (2016).

[103] C. Viengkham, Z. J. Isherwood, and B. Spehar, "Fractal statistics in the aesthetic appreciation of images, textures and sound," Journal of Vision **19**, 97b (2019).

[104] D. E. Berlyne, "Aesthetics and psychobiology," Journal of Aesthetics and Art Criticism **31** (1973).

[105] D. E. Berlyne, "Psychological aesthetics, speculative and scientific," Leonardo **10**, 56 (1977).

[106] G. Valenzise, C. Kang, and F. Dufaux, in *Human Perception of Visual Information: Psychological and Computational Perspectives* (Springer International Publishing, Cham, 2022), pp. 133–181.

[107] W. Sun, F. Zhou, and Q. Liao, "Mdid: a multiply distorted image database for image quality assessment," Pattern Recognition **61**, 153 (2017).

[108] T. Virtanen, M. Nuutinen, M. Vaahteranoksa, P. Oittinen, and J. Häkkinen, "Cid2013: a database for evaluating no-reference image quality assessment algorithms," IEEE Transactions on Image Processing **24**, 390 (2014).

[109] L.-K. Wong and K.-L. Low, "Saliency-enhanced image aesthetics class prediction," in 2009 16th ieee international conference on image processing (icip) (IEEE, 2009), pp. 997–1000.

[110] S. Bhattacharya, R. Sukthankar, and M. Shah, "A framework for photo-quality assessment and enhancement based on visual aesthetics," in Proceedings of the 18th acm international conference on multimedia (2010), pp. 271–280.

[111] T. O. Aydın, A. Smolic, and M. Gross, "Automated aesthetic analysis of photographic images," IEEE transactions on visualization and computer graphics **21**, 31 (2014).

[112] Y. Deng, C. C. Loy, and X. Tang, "Aesthetic-driven image enhancement by adversarial learning," in Proceedings of the 26th acm international conference on multimedia (2018), pp. 870–878.

[113] R. Hong, L. Zhang, and D. Tao, "Unified photo enhancement by discovering aesthetic communities from flickr," IEEE transactions on Image Processing **25**, 1124 (2016).

[114] Y. Deng, C. C. Loy, and X. Tang, "Image aesthetic assessment: an experimental survey," IEEE Signal Processing Magazine **34**, 80 (2017).

[115] S. Ma, J. Liu, and C. Wen Chen, "A-lamp: adaptive layout-aware multi-patch deep convolutional neural network for photo aesthetic assessment," in Proceedings of the ieee conference on computer vision and pattern recognition (2017), pp. 4535–4544.

[116] B. Rozière, M. Riviere, O. Teytaud, J. Rapin, Y. LeCun, and C. Couprie, "Inspirational adversarial image generation," IEEE Transactions on Image Processing **30**, 4036 (2021).

[117] F. Rieke and M. E. Rudd, "The challenges natural images pose for visual adaptation," Neuron **64**, 605 (2009).

[118] D. J. Field, "Relations between the statistics of natural images and the response properties of cortical cells," Journal of the Optical Society of America A **4**, 2379 (1987).

[119] A Van der Schaaf and J. van Hateren, "Modelling the power spectra of natural images: statistics and information," Vision research **36**, 2759 (1996).

[120] R. M. Balboa and N. M. Grzywacz, "Power spectra and distribution of contrasts of natural images from different habitats," Vision research **43**, 2527 (2003).

[121] D. Tolhurst, Y Tadmor, and T. Chao, "Amplitude spectra of natural images," Ophthalmic and Physiological Optics **12**, 229 (1992).

[122] A. Hyvärinen, J. Hurri, and P. O. Hoyer, *Natural image statistics: a probabilistic approach to early computational vision.* Vol. 39 (Springer Science & Business Media, 2009).

[123] D. Zoran and Y. Weiss, "Scale invariance and noise in natural images," IEEE 12th International Conference on Computer Vision, 2209 (2009).

[124] D. L. Ruderman, "The statistics of natural images," Network: computation in neural systems **5**, 517 (1994).

[125] D. L. Ruderman and W. Bialek, "Statistics of natural images: scaling in the woods," Physical Review Letters **73**, 814 (1994).

[126] G. J. Stephens, T. Mora, G. Tkacik, and W. Bialek, "Statistical thermodynamics of natural images," Physical Review Letters **110**, 018701 (2013).

[127] A. Haimovici and M. Marsili, "Criticality of mostly informative samples: a bayesian model selection approach," Journal of Statistical Mechanics: Theory and Experiment **2015**, P10013 (2015).

[128] R. J. Cubero, M. Marsili, and Y. Roudi, "Minimum description length codes are critical," Entropy **20**, 755 (2018).

[129] O Duranthon, M. Marsili, and R. Xie, "Maximal relevance and optimal learning machines," Journal of Statistical Mechanics: Theory and Experiment **2021**, 033409 (2021).

[130] J. Song, M. Marsili, and J. Jo, "Resolution and relevance trade-offs in deep learning," Journal of Statistical Mechanics: Theory and Experiment **2018**, 123406 (2018).

[131] R. Holtzman, M. Giulini, and R. Potestio, "Making sense of complex systems through resolution, relevance, and mapping entropy," Physical Review E **106**, 044101 (2022).

[132] M. E. Celebi, "Forty years of color quantization: a modern, algorithmic survey," Artificial Intelligence Review, 1 (2023).

[133] P. Heckbert, "Color image quantization for frame buffer display," ACM Siggraph Computer Graphics **16**, 297 (1982).

[134] M. Gervautz and W. Purgathofer, "A Simple Method for Color Quantization: Octree Quantization," in New Trends in Computer Graphics (1988), pp. 219–231.

[135] R. Balasubramanian, C. A. Bouman, and J. P. Allebach, "Sequential scalar quantization of color images," Journal of Electronic Imaging **3**, 45 (1994).

[136] A. H. Dekker, "Kohonen neural networks for optimal colour quantization," Network: Computation in Neural Systems **5**, 351 (1994).

[137] A. Abernathy and M. E. Celebi, "The incremental online k-means clustering algorithm and its application to color quantization," en, Expert Systems with Applications **207**, 117927 (2022).

[138] S.-C. Huang, "An Efficient Palette Generation Method for Color Image Quantization," en, Applied Sciences **11**, Number: 3 Publisher: Multidisciplinary Digital Publishing Institute, 1043 (2021).

[139] R. W. Floyd and L. Steinberg, "An Adaptive Algorithm for Spatial Greyscale," Proceedings of the Society for Information Display **17** (1976).

[140] R. Ulichney, *Digital Halftoning* (MIT Press, Cambridge, MA, USA, June 1987).

[141] M. Orchard and C. Bouman, "Color quantization of images," IEEE Transactions on Signal Processing **39**, 2677 (1991).

[142] J. Puzicha, M. Held, J. Ketterer, J. M. Buhmann, and D. W. Fellner, "On spatial quantization of color images," IEEE Transactions on Image Processing **9**, 666 (2000).

[143] S. Vernède, L. Ponson, and J.-P. Bouchaud, "Turbulent fracture surfaces: a footprint of damage percolation?" Physical Review Letters **114**, 215501 (2015).

[144] E. Bouchaud, "Scaling properties of cracks," Journal of Physics: Condensed Matter **9**, 4319 (1997).

[145] J. Schmittbuhl, F. Schmitt, and C. Scholz, "Scaling invariance of crack surfaces," Journal of Geophysical Research: Solid Earth **100**, 5953 (1995).

[146] J. Bouchaud, E. Bouchaud, G Lapasset, and J Planes, "Models of fractal cracks," Physical Review Letters **71**, 2240 (1993).

[147] J. R. Rice, "First-Order Variation in Elastic Fields Due to Variation in Location of a Planar Crack Front," Journal of Applied Mechanics **52**, 571 (1985).

[148] J. Schmittbuhl, S. Roux, J.-P. Vilotte, and K. J. Måløy, "Interfacial crack pinning: effect of nonlocal interactions," Physical Review Letters **74**, 1787 (1995).

[149] M. Lebihain, "Large-scale crack propagation in heterogeneous materials: an insight into the homogenization of brittle fracture properties," PhD thesis (Sorbonne université, 2019).

[150] D. Bonamy and E. Bouchaud, "Failure of heterogeneous materials: a dynamic phase transition?" Physics Reports **498**, 1 (2011).

[151] A. Hansen and J. Schmittbuhl, "Origin of the universal roughness exponent of brittle fracture surfaces: stress-weighted percolation in the damage zone," Physical Review Letters **90**, 045504 (2003).

[152] E. Bouchbinder, I. Procaccia, S. Santucci, and L. Vanel, "Fracture surfaces as multiscaling graphs," Physical Review Letters **96**, 055509 (2006).

[153] B Castaing, Y Gagne, and E. Hopfinger, "Velocity probability density functions of high reynolds number turbulence," Physica D: Nonlinear Phenomena **46**, 177 (1990).

[154] Z.-S. She and E. Leveque, "Universal scaling laws in fully developed turbulence," Physical Review Letters **72**, 336 (1994).

[155] "Big whorls, little whorls," Nature Physics **12**, 197 (2016).

[156] P. Graham, *How to Do Great Work — paulgraham.com*, `http://paulgraham.com/greatwork.html`, [Accessed 20-09-2023].

[157] G. T. Fechner, *Vorschule der aesthetik*, Vol. 1 (Breitkopf & Härtel, 1876).

[158] U. Eco and G. De Michele, *Storia della bellezza* (Bompiani Milano, 2004).

[159] E. H. Gombrich, *Art and illusion* (Princeton, 1969).

[160] E. A. Vessel and N. Rubin, "Beauty and the beholder: highly individual taste for abstract, but not real-world images," Journal of vision **10**, 18 (2010).

[161] H. J. Eysenck, "A critical and experimental study of colour preferences," The American Journal of Psychology **54**, 385 (1941).

[162] M. Bar and M. Neta, "Humans prefer curved visual objects," Psychological science **17**, 645 (2006).

[163] J Alvarez-Ramirez, C Ibarra-Valdez, and E Rodriguez, "Fractal analysis of jackson pollock's painting evolution," Chaos, Solitons & Fractals **83**, 97 (2016).

[164] C. M. Hagerhall, T. Purcell, and R. Taylor, "Fractal dimension of landscape silhouette outlines as a predictor of landscape preference," Journal of Environmental Psychology **24**, 247 (2004).

[165] I. C. McManus, "Symmetry and asymmetry in aesthetics and the arts," European Review **13**, 157 (2005).

[166] D. J. Graham and D. J. Field, "Statistical regularities of art images and natural scenes: spectra, sparseness and nonlinearities," Spatial vision **21**, 149 (2008).

[167] A. Forsythe, M. Nadal, N. Sheehy, C. J. Cela-Conde, and M. Sawey, "Predicting beauty: fractal dimension and visual complexity in art," British Journal of Psychology **102**, 49 (2011).

[168] M. S. Kanwal, J. A. Grochow, and N. Ay, "Comparing information-theoretic measures of complexity in boltzmann machines," Entropy **19**, 310 (2017).

[169] I. Kant, *Critique of the power of judgment* (Cambridge University Press, 2000).

[170] E. Aujaleu, "La sensibilité esthétique et le jugement de goût," Tréma, 33 (1997).

[171] M. Koch, J. Denzler, and C. Redies, "1/f2 characteristics and isotropy in the fourier power spectra of visual art, cartoons, comics, mangas, and different categories of photographs," PLoS one **5**, 12268 (2010).

[172] A. Desolneux, L. Moisan, and J.-M. Morel, *From gestalt theory to image analysis: a probabilistic approach*, Vol. 34 (Springer Science & Business Media, 2007).

[173] B. Gidas, "A renormalization group approach to image processing problems," IEEE Transactions on Pattern Analysis and Machine Intelligence **11**, 164 (1989).

[174] S. Foreman, J. Giedt, Y. Meurice, and J. Unmuth-Yockey, "Examples of renormalization group transformations for image sets," Phys. Rev. E **98**, 052129 (2018).

[175] R. Taylor, B. Spehar, C. Hagerhall, and P. Van Donkelaar, "Perceptual and physiological responses to jackson pollock's fractals," Frontiers in Human Neuroscience **5**, 60 (2011).

[176] B Dubuc, C Roques-Carmes, C Tricot, and S. Zucker, "The variation method: a technique to estimate the fractal dimension of surfaces," in Visual communications and image processing ii, Vol. 845 (1987), pp. 241–248.

[177] B. Spehar and R. P. Taylor, "Fractals in art and nature: why do we like them?" In Human vision and electronic imaging xviii, Vol. 8651 (2013), p. 865118.

[178] S. Losh-Hesselbart and F. J. Fowler, "Survey research methods.," Journal of the American Statistical Association **80**, 1077 (1985).

[179] S. Aral, "The problem with online ratings," MIT Sloan Management Review **55**, 47 (2014).

[180] I. C. McManus, "The aesthetics of simple figures," British Journal of Psychology **71**, 505 (1980).

[181] *Zooniverse*, `https://www.zooniverse.org/`, Accessed: 2019-06-01.

[182] M. R. Chernick, W. González-Manteiga, R. M. Crujeiras, and E. B. Barrios, *Bootstrap methods*, 2011.

[183] *Mechanical turk*, `https://www.mturk.com/`, Accessed: 2019-07-01.

[184] M. Wertheimer, *Gestalt theory* (Kegan Paul, Trench, Trubner & Company, 1938).

[185] A. Krizhevsky, I. Sutskever, and G. E. Hinton, "Imagenet classification with deep convolutional neural networks," Communications of the ACM **60**, 84 (2017).

[186] Y. LeCun, L. Bottou, Y. Bengio, and P. Haffner, "Gradient-based learning applied to document recognition," Proceedings of the IEEE **86**, 2278 (1998).

[187] A. Vaswani, N. Shazeer, N. Parmar, J. Uszkoreit, L. Jones, A. N. Gomez, Ł. Kaiser, and I. Polosukhin, "Attention is all you need," Advances in neural information processing systems **30** (2017).

[188] A. Krizhevsky and G. Hinton, "Learning multiple layers of features from tiny images," Master's thesis, Department of Computer Science, University of Toronto (2009).

[189] J. Deng, W. Dong, R. Socher, L.-J. Li, K. Li, and L. Fei-Fei, "Imagenet: a large-scale hierarchical image database," IEEE conference on computer vision and pattern recognition, 248 (2009).

[190] A. M. Saxe, J. L. McClelland, and S. Ganguli, "Exact solutions to the nonlinear dynamics of learning in deep linear neural networks," arXiv preprint arXiv:1312.6120 (2013).

[191] S. Goldt, M. Advani, A. M. Saxe, F. Krzakala, and L. Zdeborová, "Dynamics of stochastic gradient descent for two-layer neural networks in the teacher-student setup," Advances in neural information processing systems **32** (2019).

[192] G. K. Wallace, "The jpeg still picture compression standard," IEEE transactions on consumer electronics **38**, xviii (1992).

[193] A. Skodras, C. Christopoulos, and T. Ebrahimi, "The jpeg 2000 still image compression standard," IEEE Signal processing magazine **18**, 36 (2001).

[194] J. Korhonen and J. You, "Peak signal-to-noise ratio revisited: is simple beautiful?" Fourth International Workshop on Quality of Multimedia Experience, 37 (2012).

[195] Z. Wang, A. C. Bovik, H. R. Sheikh, and E. P. Simoncelli, "Image quality assessment: from error visibility to structural similarity," IEEE transactions on image processing **13**, 600 (2004).

[196] A. Humeau-Heurtier, "Multiscale entropy approaches and their applications," Entropy **22**, 644 (2020).

[197] M. B. Isichenko, "Percolation, statistical topography, and transport in random media," Reviews of modern physics **64**, 961 (1992).

[198] C Du, C Satik, and Y. Yortsos, "Percolation in a fractional brownian motion lattice," AIChE journal **42** (1996).

[199] G. Tkačik, P. Garrigan, C. Ratliff, G. Milčinski, J. M. Klein, L. H. Seyfarth, P. Sterling, D. H. Brainard, and V. Balasubramanian, "Natural images from the birthplace of the human eye," PLoS one **6**, e20409 (2011).

[200] T. Peli and D. Malah, "A study of edge detection algorithms," Computer graphics and image processing **20**, 1 (1982).

[201] M. Andreux, T. Angles, et al., "Kymatio: scattering transforms in python," The Journal of Machine Learning Research **21**, 2256 (2020).

[202] M. S. Keil, G. Cristobal, and H. Neumann, "Gradient representation and perception in the early visual system—a novel account of mach band formation," Vision Research **46**, 2659 (2006).

[203] M. S. Keil, "Gradient representations and the perception of luminosity," Vision research **47**, 3360 (2007).

[204] M. Kilpeläinen and M. A. Georgeson, "Luminance gradient at object borders communicates object location to the human oculomotor system," Scientific Reports **8**, 1593 (2018).

[205] R. Morel, G. Rochette, R. Leonarduzzi, J.-P. Bouchaud, and S. Mallat, "Scale dependencies and self-similarity through wavelet scattering covariance," arXiv preprint arXiv:2204.10177 (2022).

[206] S. G. Mallat, "Multifrequency channel decompositions of images and wavelet models," IEEE Transactions on Acoustics, speech, and signal processing **37**, 2091 (1989).

[207] J.-P. Antoine, P. Carrette, R. Murenzi, and B. Piette, "Image analysis with two-dimensional continuous wavelet transform," Signal processing **31**, 241 (1993).

[208] P. Abry, S. Jaffard, S. Roux, B. Vedel, and H. Wendt, "Wavelet decomposition of measures: application to multifractal analysis of images," Unexploded Ordnance Detection and Mitigation, 1 (2009).

[209] H. Wendt, P. Abry, S. G. Roux, S. Jaffard, and B. Vedel, "Multifractal analysis for images: the wavelet leaders contribution," Traitement du Signal **26**, 47 (2009).

[210] B. Duplantier, R. Rhodes, S. Sheffield, and V. Vargas, "Log-correlated gaussian fields: an overview," Geometry, Analysis and Probability: In Honor of Jean-Michel Bismut, 191 (2017).

[211] N. Lesmoir-Gordon, *Benoît Mandelbrot obituary — theguardian.com*, `https://www.theguardian.com/science/2010/oct/17/benoit-mandelbrot-obituary`, [Accessed 20-09-2023].

[212] E. T. Jaynes, "Information Theory and Statistical Mechanics," Physical Review **106**, 620 (1957).

[213] E. T. Jaynes, "Information Theory and Statistical Mechanics. II," Physical Review **108**, 171 (1957).

[214] L. Onsager, "Crystal Statistics. I. A Two-Dimensional Model with an Order-Disorder Transition," Physical Review **65**, 117 (1944).

[215] D. A. Rowlands, "Color conversion matrices in digital cameras: a tutorial," Optical Engineering **59**, 110801 (2020).

[216] R. F. Voss, "The fractal dimension of percolation cluster hulls," Journal of Physics A: Mathematical and General **17**, L373 (1984).

[217] A. A. Saberi, "Recent advances in percolation theory and its applications," Physics Reports, Recent advances in percolation theory and its applications **578**, 1 (2015).

[218] V. K. Shante and S. Kirkpatrick, "An introduction to percolation theory," Advances in Physics **20**, 325 (1971).

[219] *USC-SIPI Database*, `https://sipi.usc.edu/database`.

[220] S. Fishman and A. Aharony, "Random field effects in disordered anisotropic antiferromagnets," Journal of Physics C: Solid State Physics **12**, L729 (1979).

[221] D. P. Belanger and A. P. Young, "The random field Ising model," Journal of Magnetism and Magnetic Materials **100**, 272 (1991).

[222] Z. Yuan, Y. Qi, M. Hu, and Q. Li, "Opinion-Unaware No-Reference Image Quality Assessment of Smartphone Camera Images Based on Aesthetics and Human Perception," in 2020 IEEE International Conference on Multimedia Expo Workshops (ICMEW) (July 2020), pp. 1–6.

[223] A. A. Bagrov, I. A. Iakovlev, A. A. Iliasov, M. I. Katsnelson, and V. V. Mazurenko, "Multiscale structural complexity of natural patterns," Proceedings of the National Academy of Sciences **117**, 30241 (2020).

[224] J. McCormack, C. Cruz Gambardella, and A. Lomas, "The Enigma of Complexity," in Artificial Intelligence in Music, Sound, Art and Design (2021), pp. 203–217.

[225] H.-Z. Huang, K. Xu, R. R. Martin, F.-Y. Huang, and S.-M. Hu, "Efficient, Edge-Aware, Combined Color Quantization and Dithering," IEEE Transactions on Image Processing **25**, Conference Name: IEEE Transactions on Image Processing, 1152 (2016).

[226] S. Thompson, M. E. Celebi, and K. H. Buck, "Fast color quantization using MacQueen's k-means algorithm," en, Journal of Real-Time Image Processing **17**, 1609 (2020).

[227] M. Frackiewicz, A. Mandrella, and H. Palus, "Fast Color Quantization by K-Means Clustering Combined with Image Sampling," en, Symmetry **11**, Number: 8 Publisher: Multidisciplinary Digital Publishing Institute, 963 (2019).

[228] G. Ramella, "Evaluation of quality measures for color quantization," en, Multimedia Tools and Applications **80**, 32975 (2021).

[229] L. E. Jaques, A. C. D. Ii, E. Murrell, D. Xie, C. P. Bailey, and P. Guturu, "Novel L1 PCA informed K-means color quantization," in Big Data IV: Learning, Analytics, and Applications, Vol. 12097 (May 2022), pp. 151–157.

[230] J. F. Jarvis, C. N. Judice, and W. Ninke, "A survey of techniques for the display of continuous tone pictures on bilevel displays," Computer graphics and image processing **5**, 13 (1976).

[231] L. Rüschendorf, "The wasserstein distance and approximation theorems," Probability Theory and Related Fields **70**, 117 (1985).

[232] H Hersbach and P. Janssen, "Improvement of the short-fetch behavior in the wave ocean model (wam)," Journal of Atmospheric and Oceanic Technology **16**, 884 (1999).

[233] F. S. Labini, M. Montuori, and L. Pietronero, "Scale-invariance of galaxy clustering," Physics Reports **293**, 61 (1998).

[234] P. H. Coleman and L. Pietronero, "The fractal structure of the universe," Physics Reports **213**, 311 (1992).

[235] H. Hentschel and I. Procaccia, "Relative diffusion in turbulent media: the fractal dimension of clouds," Physical Review A **29**, 1461 (1984).

[236] B. Mandelbrot, *Gaussian self-affinity and fractals: globality, the earth, 1/f noise, and r/s* (Springer Science & Business Media, 2002).

[237] B. B. Mandelbrot, *Multifractals and 1/f noise: wild self-affinity in physics (1963–1976)* (Springer, 2013).

[238] J. Feder, *Fractals* (Springer Science & Business Media, 2013).

[239] P. Bak, C. Tang, and K. Wiesenfeld, "Self-organized criticality: an explanation of the 1/f noise," Physical Review Letters **59**, 381 (1987).

[240] A.-L. Barabási and T. Vicsek, "Multifractality of self-affine fractals," Physical Review A **44**, 2730 (1991).

[241] B. B. Mandelbrot and B. B. Mandelbrot, "Intermittent turbulence in self-similar cascades: divergence of high moments and dimension of the carrier," Multifractals and $1/f$ Noise: Wild Self-Affinity in Physics (1963–1976), 317 (1999).

[242] S. Chibbaro and C. Josserand, "Elastic wave turbulence and intermittency," Physical Review E **94**, 011101 (2016).

[243] H. E. Stanley and P. Meakin, "Multifractal phenomena in physics and chemistry," Nature **335**, 405 (1988).

[244] J. Schmittbuhl, J.-P. Vilotte, and S. Roux, "Reliability of self-affine measurements," Physical Review E **51**, 131 (1995).

[245] V. A. Yastrebov, G. Anciaux, and J.-F. Molinari, "From infinitesimal to full contact between rough surfaces: evolution of the contact area," International Journal of Solids and Structures **52**, 83 (2015).

[246] L. Talon, H. Auradou, and A. Hansen, "Permeability of self-affine aperture fields," Physical Review E **82**, 046108 (2010).

[247] R. Liu, Y. Jiang, B. Li, and X. Wang, "A fractal model for characterizing fluid flow in fractured rock masses based on randomly distributed rock fracture networks," Computers and Geotechnics **65**, 45 (2015).

[248] K. Hirokatsu, M. Asato, Y. Eisuke, Y. Ryosuke, I. Nakamasa, A. Nakamura, and S. Yutaka, "Pre-training without natural images," International Journal of Computer Vision **130**, 990 (2022).

[249] C. Anderson and R. Farrell, "Improving fractal pre-training," in Proceedings of the ieee/cvf winter conference on applications of computer vision (2022), pp. 1300–1309.

[250] Z. Li, S. Bhojanapalli, M. Zaheer, S. Reddi, and S. Kumar, "Robust training of neural networks using scale invariant architectures," in International conference on machine learning (PMLR, 2022), pp. 12656–12684.

[251] A. Fournier, D. Fussell, and L. Carpenter, "Computer rendering of stochastic models," Communications of the ACM **25**, 371 (1982).

[252] O. Moreva and M. Schlather, "Fast and exact simulation of univariate and bivariate gaussian random fields," Stat **7**, e188 (2018).

[253] S. Lovejoy and D. Schertzer, "On the simulation of continuous in scale universal multifractals, part i: spatially continuous processes," Computers & Geosciences **36**, 1393 (2010).

[254] N Decoster, S. Roux, and A Arneodo, "A wavelet-based method for multifractal image analysis. ii. applications to synthetic multifractal rough surfaces," The European Physical Journal B-Condensed Matter and Complex Systems **15**, 739 (2000).

[255] E. Bacry, J. Delour, and J.-F. Muzy, "Multifractal random walk," Physical Review E **64**, 026103 (2001).

[256] B. B. Mandelbrot and J. W. Van Ness, "Fractional brownian motions, fractional noises and applications," SIAM review **10**, 422 (1968).

[257] A. Lischke, G. Pang, M. Gulian, F. Song, C. Glusa, X. Zheng, Z. Mao, W. Cai, M. M. Meerschaert, M. Ainsworth, et al., "What is the fractional laplacian? a comparative review with new results," Journal of Computational Physics **404**, 109009 (2020).

[258] T. Bojdecki and L. G. Gorostiza, "Fractional brownian motion via fractional laplacian," Statistics & probability letters **44**, 107 (1999).

[259] A. Lodhia, S. Sheffield, X. Sun, and S. S. Watson, "Fractional Gaussian fields: A survey," Probability Surveys **13**, 1 (2016).

[260] I. S. Gradshteyn and I. M. Ryzhik, *Table of integrals, series, and products* (Academic press, 2014).

[261] P. Whittle, "On stationary processes in the plane," Biometrika, 434 (1954).

[262] F. Lindgren, D. Bolin, and H. Rue, "The spde approach for gaussian and non-gaussian fields: 10 years and still running," Spatial Statistics **50**, 100599 (2022).

[263] J. P. Sethna, K. A. Dahmen, and C. R. Myers, "Crackling noise," Nature **410**, 242 (2001).

[264] E. Bacry, A. Kozhemyak, and J. F. Muzy, "Log-normal continuous cascade model of asset returns: aggregation properties and estimation," Quantitative Finance **13**, 795 (2013).

[265] J.-S. Gagnon, S Lovejoy, and D Schertzer, "Multifractal surfaces and terrestrial topography," Europhysics letters **62**, 801 (2003).

[266] L. Chevillard, S. G. Roux, E. Lévêque, N. Mordant, J.-F. Pinton, and A. Arnéodo, "Intermittency of velocity time increments in turbulence," Physical Review Letters **95**, 064501 (2005).

[267] L. Chevillard, B. Castaing, E. Lévêque, and A. Arnéodo, "Unified multifractal description of velocity increments statistics in turbulence: intermittency and skewness," Physica D: Nonlinear Phenomena **218**, 77 (2006).

[268] J. Duchon and R. Robert, "Champs aléatoires intermittents. partie i: champs à accroissements symétriques," Comptes rendus. Mathématique **341**, 265 (2005).

[269] X. Clotet, J. Ortín, and S. Santucci, "Disorder-induced capillary bursts control intermittency in slow imbibition," Physical Review Letters **113**, 074501 (2014).

[270] M. Zamparo, "Apparent multifractality of self-similar lévy processes," Nonlinearity **30**, 2592 (2017).

[271] J.-P. Bouchaud, M. Potters, and M. Meyer, "Apparent multifractality in financial time series," The European Physical Journal B-Condensed Matter and Complex Systems **13**, 595 (2000).

[272] E. Bacry, J. Delour, and J.-F. Muzy, "Modelling financial time series using multifractal random walks," Physica A: statistical mechanics and its applications **299**, 84 (2001).

[273] J Delour, J. Muzy, and A Arneodo, "Intermittency of 1d velocity spatial profiles in turbulence: a magnitude cumulant analysis," The European Physical Journal B **23**, 243 (2001).

[274] A Arneodo, E. Bacry, S Manneville, and J. Muzy, "Analysis of random cascades using space-scale correlation functions," Physical Review Letters **80**, 708 (1998).

[275] J. O'Neil and C. Meneveau, "Spatial correlations in turbulence: predictions from the multifractal formalism and comparison with experiments," Physics of Fluids A: Fluid Dynamics **5**, 158 (1993).

[276] S. Santucci, K. J. Måløy, A. Delaplace, J. Mathiesen, A. Hansen, J. Ø. H. Bakke, J. Schmittbuhl, L. Vanel, and P. Ray, "Statistics of fracture surfaces," Physical Review E **75**, 016104 (2007).

[277] L Ponson, Z Shabir, M Abdulmajid, E Van der Giessen, and A Simone, "Unified scenario for the morphology of crack paths in two-dimensional disordered solids," Physical Review E **104**, 055003 (2021).

[278] E. Bouchbinder, I. Procaccia, and S. Sela, "Disentangling scaling properties in anisotropic fracture," Physical Review Letters **95**, 255503 (2005).

[279] L. Ponson, D. Bonamy, and E. Bouchaud, "Two-dimensional scaling properties of experimental fracture surfaces," Physical Review Letters **96**, 035506 (2006).

[280] A. Lagae, S. Lefebvre, R. Cook, T. DeRose, G. Drettakis, D. S. Ebert, J. P. Lewis, K. Perlin, and M. Zwicker, "A survey of procedural noise functions," in Computer graphics forum, Vol. 29, 8 (Wiley Online Library, 2010), pp. 2579–2600.

[281] R. Rhodes and V. Vargas, "Multidimensional Multifractal Random Measures," Electronic Journal of Probability **15**, 241 (2010).

[282] J. van Lawick van Pabst and H. Jense, *Dynamic terrain generation based on multifractal techniques*, edited by M. Chen, P. Townsend, and J. A. Vince (Springer London, London, 1996), pp. 186–203.

[283] R. H. Kraichnan and D. Montgomery, "Two-dimensional turbulence," Reports on Progress in Physics **43**, 547 (1980).

[284] G. Boffetta and R. E. Ecke, "Two-dimensional turbulence," Annual review of fluid mechanics **44**, 427 (2012).

[285] M. A. Ferreira, J. Lukkarinen, A. Nota, and J. J. Velázquez, "Stationary non-equilibrium solutions for coagulation systems," Archive for Rational Mechanics and Analysis **240**, 809 (2021).

[286] B. B. Mandelbrot, D. E. Passoja, and A. J. Paullay, "Fractal character of fracture surfaces of metals," Nature **308**, 721 (1984).

[287] M. Lebihain, L. Ponson, D. Kondo, and J.-B. Leblond, "Effective toughness of disordered brittle solids: a homogenization framework," Journal of the Mechanics and Physics of Solids **153**, 104463 (2021).

[288] L. Ponson, "Depinning transition in the failure of inhomogeneous brittle materials," Physical Review Letters **103**, 055501 (2009).

[289] S Aligholi, L. Ponson, A. Torabi, and Q. Zhang, "A new methodology inspired from the theory of critical distances for determination of inherent tensile strength and fracture toughness of rock materials," International Journal of Rock Mechanics and Mining Sciences **152**, 105073 (2022).

[290] L. Ponson, Y. Cao, E. Bouchaud, V. Tvergaard, and A. Needleman, "Statistics of ductile fracture surfaces: the effect of material parameters," in Fracture phenomena in nature and technology: proceedings of the iutam symposium on fracture phenomena in nature and technology held in brescia, italy, 1-5 july 2012 (Springer, 2014), pp. 137–149.

[291] G. I. Barenblatt, "The mathematical theory of equilibrium cracks in brittle fracture," Advances in applied mechanics **7**, 55 (1962).

[292] G. Timár and F. Kun, "Crackling noise in three-point bending of heterogeneous materials," Physical Review E **83**, 046115 (2011).

[293] N. M. Pugno and R. S. Ruoff, "Quantized fracture mechanics," Philosophical Magazine **84**, 2829 (2004).

[294] R. N. Mantegna and H. E. Stanley, "Stochastic process with ultraslow convergence to a gaussian: the truncated lévy flight," Physical Review Letters **73**, 2946 (1994).

[295] H. Nakao, "Multi-scaling properties of truncated lévy flights," Physics Letters A **266**, 282 (2000).

[296] B. Mandelbrot, "The pareto-levy law and the distribution of income," International economic review **1**, 79 (1960).

[297] M. F. Shlesinger, J. Klafter, and Y. Wong, "Random walks with infinite spatial and temporal moments," Journal of Statistical Physics **27**, 499 (1982).

[298] M. Benzaquen and J.-P. Bouchaud, "A fractional reaction–diffusion description of supply and demand," The European Physical Journal B **91**, 1 (2018).

[299] E. W. Montroll and G. H. Weiss, "Random walks on lattices. ii," Journal of Mathematical Physics **6**, 167 (1965).

[300] V. V. Uchaikin, "Montroll–weiss problem, fractional equations, and stable distributions," International Journal of Theoretical Physics **39**, 2087 (2000).

[301] A.-L. Barabási, R. Bourbonnais, M. Jensen, J. Kertész, T. Vicsek, and Y.-C. Zhang, "Multifractality of growing surfaces," Physical Review A **45**, R6951 (1992).

[302] I. V. Lomakin, T. Mäkinen, K. Widell, J. Savolainen, S. Coffeng, J. Koivisto, and M. J. Alava, "Fatigue crack growth in an aluminum alloy: avalanches and coarse graining to growth laws," Physical Review Research **3**, L042029 (2021).

[303] L. Ponson, H. Auradou, M. Pessel, V. Lazarus, and J.-P. Hulin, "Failure mechanisms and surface roughness statistics of fractured fontainebleau sandstone," Physical Review E **76**, 036108 (2007).

[304] N. Mallick, P.-P. Cortet, S. Santucci, S. G. Roux, and L. Vanel, "Discrepancy between subcritical and fast rupture roughness: a cumulant analysis," Physical Review Letters **98**, 255502 (2007).

[305] E Bouchaud, J. Bouchaud, D. Fisher, S Ramanathan, and J. Rice, "Can crack front waves explain the roughness of cracks?" Journal of the Mechanics and Physics of Solids **50**, 1703 (2002).

[306] M. Stojanova, S Santucci, L Vanel, and O Ramos, "High frequency monitoring reveals aftershocks in subcritical crack growth," Physical Review Letters **112**, 115502 (2014).

[307] J.-F. Muzy and E. Bacry, "Multifractal stationary random measures and multifractal random walks with log infinitely divisible scaling laws," Physical Review E **66**, 056121 (2002).

[308] B. B. Mandelbrot, "Multifractal measures, especially for the geophysicist," Fractals in geophysics, 5 (1989).

[309] K. T. Tallakstad, R. Toussaint, S. Santucci, J. Schmittbuhl, and K. J. Måløy, "Local dynamics of a randomly pinned crack front during creep and forced propagation: an experimental study," Physical Review E **83**, 046108 (2011).

[310] J. Kent-Dobias, "Log-correlated color in monet's paintings," arXiv preprint arXiv:2209.01989 (2022).

[311] O. Phillips, *The dynamics of the upper ocean*, Cambridge monographs on mechanics and applied mathematics (Cambridge U.P., 1966).

[312] P. E. Lynch and G. O. Zumbach, "Market heterogeneities and the causal structure of volatility," Quantitative Finance **3**, 320 (2003).

[313] G. Zumbach, "Volatility processes and volatility forecast with long memory," Quantitative Finance **4**, 70 (2003).

[314] J.-P. Bouchaud, A. Matacz, and M. Potters, "Leverage effect in financial markets: the retarded volatility model," Physical Review Letters **87**, 228701 (2001).

[315] J. C. Cox and S. A. Ross, "The valuation of options for alternative stochastic processes," Journal of financial economics **3**, 145 (1976).

[316] P. S. Johansson and H. I. Andersson, "Generation of inflow data for inhomogeneous turbulence," Theoretical and Computational Fluid Dynamics **18**, 371 (2004).

[317] M. Klein, A. Sadiki, and J. Janicka, "A digital filter based generation of inflow data for spatially developing direct numerical or large eddy simulations," Journal of computational Physics **186**, 652 (2003).

[318] M. Peskin, *An introduction to quantum field theory* (CRC press, 2018).

[319] P. Hager and E. Neuman, "The multiplicative chaos of h= 0 fractional brownian fields," The Annals of Applied Probability **32**, 2139 (2022).

[320] E. Neuman and M. Rosenbaum, "Fractional brownian motion with zero hurst parameter: a rough volatility viewpoint," (2018).

[321] M. Riesz, "L'intégrale de Riemann-Liouville et le problème de Cauchy," Acta Mathematica **81**, 1 (1949).

[322] T. D. Jacobs, T. Junge, and L. Pastewka, "Quantitative characterization of surface topography using spectral analysis," Surface Topography: Metrology and Properties **5**, 013001 (2017).

[323] R Benzi, S Ciliberto, R. Tripiccione, C Baudet, F Massaioli, and S Succi, "Extended self-similarity in turbulent flows," Physical Review E **48**, R29 (1993).

LIST OF FIGURES

LIST OF TABLES

Titre : Approches turbulentes de l'analyse d'image et de la fractographie statistique

Mots clés : traitement d'image, esthétique quantitative, théorie de l'information, turbulence, fractographie, synthèse d'images

Résumé :
D'aucun diraient que le rôle du physicien est de décrire l'univers par des règles et des lois. En réalité, bien que le comportement des systèmes simples puisse être déduit de premiers principes, cette tâche devient difficile lorsque ces systèmes gagnent en complexité. Une seconde approche consiste alors à caractériser la réponse des systèmes soumis à des sollicitations harmoniques ou stochastiques. Cette méthode est d'autant plus intéressante en haute dimension, puisqu'elle permet (i) l'exploration efficace des différentes configurations du système, et (ii) la mise en évidence de certains régimes spécifiques. Un exemple classique serait celui de la turbulence fluide, dont l'étude révèle la présence d'un régime fractal/invariant d'échelle universel, inattendu par les équations de Navier-Stokes. Nous faisons un usage important de ces intuitions en introduisant des outils statistiques dans l'étude de sujets en apparence différents : le traitement d'images et la fractographie statistique.
Dans la première partie de cette thèse, j'aborde trois problèmes distincts du traitement de l'image. Tout d'abord, je revisite la question du lien entre l'appréciation visuelle et les propriétés statistiques des images. Ensuite, j'aborde le cas des images naturelles, dont l'analyse repose sur des observables mesurant l'information contenue dans les images à toutes les échelles : la *Multiscale relevance* (MSR). Enfin, le problème spécifique de la quantification des couleurs est traité par l'établissement d'algorithmes basés sur des principes de maximisation de l'entropie.
Dans la deuxième partie du manuscrit, j'étudie les surfaces de fracture obtenues par la rupture complète d'un matériau. Ces surfaces présentent des propriétés statistiques rappelant la turbulence des fluides par leur invariance d'échelle, et leurs fluctuations non-Gaussiennes. Tout d'abord, je définis une classe de champs aléatoires reproduisant ces propriétés. Leur comparaison avec une surface de rupture permet de souligner les similarités, ainsi que les différences principalement liées à la topologie des évènements turbulents. Enfin, l'analyse de quatre surfaces de roches permet de mettre en évidence le lien entre la longueur de corrélation du régime multifractal, et la taille de la *Fracture Process Zone* où les phénomènes de coalescence de l'endommagement se produisent. Des modèles stochastiques de propagation de fissure sont développés, et montrent l'émergence de la multifractalité à partir d'hypothèses simples, basées sur des observations expérimentales.

Title : Turbulent approaches to image analysis and statistical fractography

Keywords : image processing, quantitative aesthetics, information theory, turbulence, fractography, texture synthesis

Abstract : One may argue that the role of the physicist is to describe the universe from rules and laws. However, while the behaviour of simple physical settings can be derived from first principles, this step becomes increasingly difficult when systems gain in complexity. A second approach consists in characterizing the response of systems to harmonic or stochastic forcing. This method is all the more interesting in high dimension, as it allows one to efficiently explore the configuration space, and highlight specific regimes. Maybe the most classic example would be of fluid turbulence the analysis of which reveals universal scaling properties, unexpected from the local Navier-Stokes equations. We make strong use of these intuitions by introducing statistical and fluctuations-based tools in the study of two seemingly different subjects: image processing and statistical fractography.
In the first part of this thesis, I tackle three distinct problems in image analysis and processing, by establishing fluctuation-based metrics with straightforward interpretability. First, I revisit the long-standing question of the relation between visual appreciation and image statistics. Then, an agnostic information-theoretic observable is employed to investigate the statistical properties of natural images. Finally, I address the specific problem of image color quantization by deriving stochastic mapping algorithms from maximum entropy principles.
In the second part of the manuscript, I study fracture surfaces resulting from the complete failure of a material. These surfaces display universal statistical properties reminiscent of fluid turbulence, namely scale invariance, non-Gaussian statistics and multi-affinity. First, I define a minimal class of random fields reproducing these properties. The comparison with fracture surfaces highlights slight differences, mainly related to the presence of cliffs on the surface reminiscent of turbulent dissipation fields filaments. Then, the study of four fracture surfaces from different rocks materials allows us to link the correlation length ξ defining the multifractal regime, with the size of the Fracture Process Zone ℓ_c, in which dissipative coalescence mechanisms occur. Some stochastic models of crack propagation are ultimately introduced, and show the emergence of multifractal scaling, from ad-hoc assumptions based on experimental observations.

Institut Polytechnique de Paris
91120 Palaiseau, France